Two-Dimensional Ultrafast Pulse Shaping and its Application to Coherent Control and Spectroscopy

by

Joshua Charles Vaughan
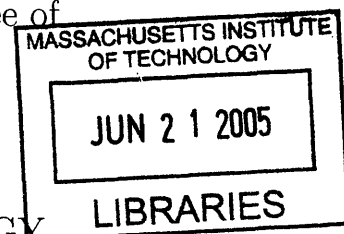
B.A. Chemistry, Reed College 2000

Submitted to the Department of Chemistry
in partial fulfillment of the requirements for the degree of

DOCTOR OF PHILOSOPHY

at the

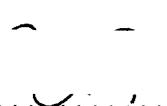MASSACHUSETTS INSTITUTE OF TECHNOLOGY

June 2005
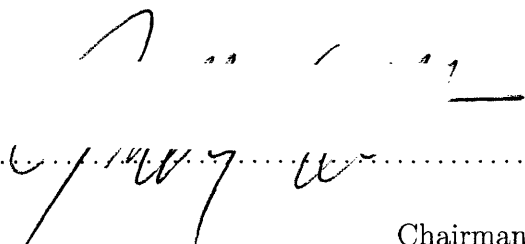
Author ....
Department of Chemistry
May 23, 2005
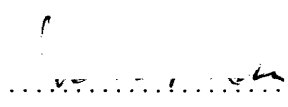
Certified by ....
Keith A. Nelson
Professor
Thesis Supervisor

Accepted by ....
Robert W. Field
Chairman, Department Committee on Graduate Students

This doctoral thesis has been examined by a committee of the Department of Chemistry as follows:

Professor Jeffrey I. Steinfeld ....

Chairman

Professor Keith A. Nelson ....

Thesis Supervisor

Professor Robert G. Griffin ....

3

Two-Dimensional Ultrafast Pulse Shaping and its Application to Coherent Control and Spectroscopy

by

Joshua Charles Vaughan

B.A. Chemistry, Reed College 2000
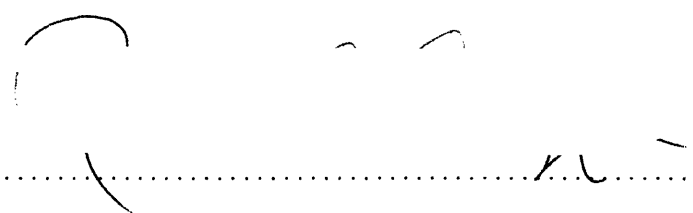
Abstract

This thesis develops powerful new methods for shaping femtosecond laser pulses in two dimensions and explores their application to coherent control of propagating lattice excitations and degenerate four-wave mixing spectroscopy. Pulse shaping in two dimensions is achieved by manipulating the spectral components of ultrashort laser pulses within many horizontal slices of the pulse. Each horizontal slice is independently shaped by means of a two-dimensional liquid crystal spatial light modulator, and taken together the shaped regions form sophisticated optical waveforms with time-dependent spatial profiles.

Automated optical control over coherent lattice responses that are both time- and position-dependent across macroscopic length scales is demonstrated. Two-dimensional (2D) femtosecond pulse shaping was used to generate excitation light fields that were directed toward distinct regions of crystalline samples, producing terahertz-frequency lattice vibrational waves that emanated outward from their multiple origins at lightlike speeds. Interferences among the waves resulted in fully specified far-field responses, including tilted, focusing, or amplified wavefronts. Generation and coherent amplification of terahertz travelling waves and terahertz phased-array generation are also demonstrated.

A novel approach to coherent nonlinear optical spectroscopy based on 2D femtosecond pulse shaping is introduced. Multiple phase-stable output beams are created and overlapped at the sample in a phase-matched boxcars geometry via 2D femtosecond pulse shaping. The pulse timing, shape, phase, and spectral content within all beams may be specified, yielding an unprecedented level of control over the interacting fields in nonlinear spectroscopic experiments. Heterodyne detection and phase cycling of the nonlinear signal is easily implemented due to the excellent phase stability between each output beam. This approach combines the waveform generation capabilities of magnetic resonance spectroscopy with the wavevector specification and phase-matching of nonlinear optical spectroscopy, yielding the signal selectivity

and control capabilities of both. Results on three prototype systems will be used to illustrate the exciting possibilities with this method.

Thesis Supervisor: Keith A. Nelson
Title: Professor

Acknowledgments

Five years ago, I arrived at MIT, ready to try my hand at graduate research, but with little idea of what lay in store for me. Before I knew it, I was immersed in problem sets, teaching assistant duties, cumulative exams, battles with uncooperative lasers, programming in Matlab and LabVIEW, machine shop marathons, plumbing repairs, and more fancy optical equipment than I ever dreamed existed. I learned the joy of designing and building scientific tools, the thrill of seeing a new result for the first time, and the satisfaction of taking a project from conception to execution to publication. Somewhere along the way there was even time for frisbee golf, hikes in Andover and elsewhere, badminton, pool at Flat Top Johnny's, and great research conferences in great locations, such as Tegernsee, Germany (in a castle, no less), Corsica, France (the dorms were on the beach), Niigata, Japan, and Vancouver, British Columbia. I have been fortunate to share in these adventures (and misadventures) with many wonderful friends and coworkers whom I would now like to thank.

Keith Nelson has been a superb research advisor. I vividly recall first meeting him when I was a prospective student. He told me all about the ultrafast spectroscopy and terahertz polaritonics work being conducted in the group at the time. I recognized right away the infectious enthusiasm he has for science, and its positive effect on me, even though I didn't understand much of what he was telling me. He has always been generous with his time, supportive of my fledgling ideas and pursuits, and ready to give me a nudge when I needed one. Although I will soon be moving to Harvard as a postdoc in the lab of Xiaowei Zhuang, I think some part of me will be always looking over my shoulder, waiting for Keith to stride into lab and ask me, in his characteristic way, "How's it going?"

Although the students and postdocs that were in the Nelson group when I first joined have since left and been replaced by a new crowd, the group has always been a great source of talent and friendship. Without their camaraderie, help, and support, life in graduate school would have been dull and probably somewhat painful. Among the many excellent group members with whom I have spent time, my most important

thank you goes to Thomas Feurer, post-doc extraordinaire. He taught me, among other things, how to torture femtosecond laser pulses, how to catch phonon-polaritons in the dark, and perhaps most significantly how to apply my creativity to science. He was a pleasure to work with, and a great sounding board for new ideas. Although I only spent about a year with him working in the laboratory, much of my work in the subsequent three years was related directly to brainstorming sessions we had over chips and salsa at lunchtime during that first year. I am greatly pleased that he is now a professor, a capacity in which I am certain his excellent scientific instincts, amazing technical skills, patience, and keen sense of humor will continue to enrich the lives of those around him.

Thomas Hornung has been a fantastic coworker and friend over the past year and a half, in good times (walks in the local parks with Irina, Kobe beef dinner in Hamamatsu) and in bad (potassium fire). He contributed many ingenious ideas to the degenerate four-wave mixing spectroscopy project, giving it a much needed push. In addition, the THz amplification methods we spent so long developing seem to be paying off with the experiments that he and Ka-Lo Yeh are now conducting. I have always been impressed with his versatility in experiments, theory, and computation. His Karaoke, on the other hand, needs a bit of work.

Peter Poulin was a great asset to the group, for his selfless computer assistance, his wizardry in decoding cryptic hexadecimal messages from laboratory equipment, and amazingly accurate impersonations of characters from the Simpsons. I have been glad to have him as a friend and group member, and I am happy that we are both staying in the Boston area and will be able to hang out in the coming years. Ben Paxton has been a good friend and partner in crime, from the early days with our quantum mechanics "Magical Mystery Tour" problem sets, to that time he and I drove to long island with a sick Nd:YLF laser, to our adventures in Japan last summer at Ultrafast Phenomena 14. Nikolay "ngoops I did it again" Stoyanov helped me numerous times with difficult mathematical and computational problems, usually solving them quickly from first-principles considerations. His eastern European charms always brought a smile to my face, and he also has a great high-kick if you are brave enough to hold

something on your head for a demonstration.

Jaime Choi (nee Beers) has been a good friend and coworker over the past 5 years. Her perpetually upbeat attitude was a blessing to the group, and there was no better person to talk to if something had got me down. I am glad that she, also, will be staying in the Boston area, and I look forward to more barbecues, board games, and sushi nights with her and her husband Michael. Darius Torchinsky and Tina Hecksher are my fellow 8-ball aficionados, and I look forward to more nights out with them and others of the group. Eric Statz, a man of nearly infinite patience, has been a valuable resource to the group, particularly with computer support. He also provided lots of useful input on and corrections of the description of phonon-polaritons in chapter three of this thesis. Any inaccuracies may therefore be directed to him. David Ward has provided technical assistance on numerous occasions, and has kept things lively in the group.

Kathy Stone and Ka-Lo Yeh are up-and-coming graduate students in the group with whom Thomas Hornung and I have worked with over the past year and a half. I am eager to see them develop into confident scientists in the next few years, and I can only guess what exciting things they will accomplish. They have been kind enough to put up with my unconventional schedule, my numerous lectures about how not to break the equipment, and occasional Tuvan-style throat singing in the lab. Kathy helped with the spectral interferometry measurements and LC SLM characterization that are included in chapter two of this thesis. Additionally, Sabine Volkmer visited from Germany in the summer of 2002, and worked on the two-dimensional terahertz field shaping experiments discussed in chapter three of this thesis.

I have also enjoyed spending time with my other group members, Christ Glorieux, Christoph "die Organizator" Klieber, Cindy Bolme, Emmanuel Peronne, Gagan Saini, Greg Wakeham, Kenji Katayama, Kevin Webb, Masashi Yamaguchi, Osamu Kamishima, Rebecca Slayton, and Taeho Shin. A very special thank you goes to Gloria Pless, whose behind-the-scenes efforts with administrative matters have contributed tremendously to the group.

My roommates Dena Cohen, Shelly Fujikawa, and Yamil Suarez have been a

big part of my life during graduate school. We have enjoyed many dinner parties, ER nights, two superbowl victories, the end of the 86-year Red Sox' Curse of the Bambino, and numerous late nights relaxing on the sofas with bad cable programming. My roommates have also been dedicated participants in my mushroom cultivation efforts (maitake, shiitake, portabella...yum) and patient bystanders with several of my unintended penicillin cultivation efforts in our refrigerator. Thanks for all the good times!

My family has been a great asset to me. Mom, you have trained me well in life and in Scrabble. I'm thrilled with how well you've done for yourself, starting over at age 59. Pop, thanks for fostering all my interests and hobbies over the years, and for instilling in me a love of tinkering, a commitment to high standards in the endeavors I pursue, and a healthy irreverence for conformity. Jenny, I'm proud of how far you've come in the past 6 years. It's great to see you all grown up and married–now get started on those nieces and nephews! Jason, we make good tag-team ministers. No matter how many years go by, you'll always be the big brother I looked up to when I was a kid.

Last but not least, I would like to thank Juan Zheng for being such a wonderful companion over the past five years. We met on the very first day of graduate school, and hit it off right away. I would never have imagined that I would end up with such a talented, beautiful, intelligent, kind, and nurturing person as her who is not only a brilliant cook but also trilingual. She has been supportive of me in all my (sometimes bizarre) interests, and smiles at my jokes even if she's heard them before. I am thrilled to embark upon the rest of our lives together and I look forward with excitement to what the future will hold for us.

Contents

Chapter 1

Introduction

Ultrashort laser pulses are coherent bursts of light with durations on the order of femtoseconds (10^{-15} seconds), making them the fastest tool created by mankind for monitoring and controlling matter. During the time it takes an ultrashort laser pulse to pass a given point within a sample, the nuclei of the atoms within the sample are virtually motionless. This extreme brevity allows for unique ability to both initiate and observe fleeting chemical and physical events. Measurements performed with ultrashort laser pulses are therefore analogous to the high-speed flash photographs of Harold Edgerton [1] and others that seem to stop time. One well-known photograph recorded a balloon caught in the act of exploding just after a bullet had passed through it. A chemical experiment analogous to the exploding balloon would be the measurement of a molecule as it is falling apart, such as the photodissociation of the gas-phase molecule ICN by Dantus et al. [2]. In this experiment, an ultraviolet laser pulse played the role of the bullet, and variably delayed probe pulses were used to measure the buildup of the CN fragment as a function of time. These *femtochemistry* experiments were recognized with a Nobel prize in chemistry in 1999 and continue to provide microscopic detail to the mechanisms underlying reactive photochemistry.

Beyond measurements of chemical processes, in which variably delayed probe pulses are used to quantify the *amount* of a given substance at different points in time following an excitation pulse, a wide variety of powerful multiple-pulse spectroscopic methods have emerged that can reveal detailed information about systems being stud-

ied. This wealth of available information can help to elucidate static properties such as molecular structure and bonding and it can help to study dynamic processes such as solvation and energy transfer. An exciting recent development within this field is two-dimensional ultrafast infrared (2D IR) spectroscopy [3], a technique that is the vibrational analogue of two-dimensional nuclear magnetic resonance (2D NMR) spectroscopy [4]. The motivation behind 2D IR spectroscopy is in large part fuelled by the phenomenal success of 2D NMR, which, among its many achievements, has revolutionized the determination of the structures of complex biological molecules. Unlike 2D NMR, which in most cases has a time resolution on the order of milliseconds and therefore probes a variety of nuclear configurations for a sample of interest, 2D ultrafast infrared spectroscopy can determine transient structural information with a time resolution on the order of picoseconds, yielding insights into, for instance, the nature of chemical solvation environments [3] and mechanisms underlying protein folding [5].

In parallel with ultrafast spectroscopic techniques aimed at studying systems and how they interact with their surroundings, scientists have long sought to use laser pulses to *control* rotational, vibrational, and electronic responses in matter. Unlike the simple ultraviolet pulse used to initiate the dissociation of ICN, highly structured, *shaped* laser pulses may be used to achieve various control objectives, including generating new states of matter and controlling chemical reactions. An early example of such experiments used a series of approximately 20 evenly-spaced pulses to create large vibrational amplitudes in the molecular crystal α-perylene [6], much in the way that a child is repetitively pushed on a swing. Each pulse exerted a sudden "impulse" force on low-frequency Raman-active vibrational modes of the crystal [via impulsive stimulated Raman scattering, (ISRS)], setting the crystal into oscillatory motion. The delay between successive pulses was then varied to coincide with the oscillation period of a particular vibrational mode of the crystal, such that a large vibrational amplitude was generated. Unlike excitation with a single pulse, where multiple vibrational modes are excited, use of a shaped excitation pulse allowed for selective excitation of just one vibrational mode of the crystal. Furthermore, a single intense excitation pulse could not be used to generate such large amplitudes since

14

its peak intensity would be so large that the crystal would become damaged or even permanently ablated.

More recently, many ground-breaking experiments have extended control schemes based on shaped laser pulses to a wide variety of systems, including: preparation of highly structured electron wavepackets in Rydberg states of atoms [7]; control of resonant and nonresonant multiphoton excitation [8, 9]; ultrafast manipulation of electron spin coherence [10]; selective dissociation and rearrangement of molecules [11, 12, 13]; control over energy-transfer pathways in light harvesting bacteria [14]; and chemically-selective microscopy [15]. Additionally, a large body of theoretical work over the past 20 years has focused on controlling chemical reactions with shaped laser pulses, as reviewed recently by Rice et al. [16] and Shapiro et al. [17]. A number of these theoretical schemes have shown exciting possibilities for moving beyond the control of selective dissociation of a single molecule to more complicated tasks such as control of bimolecular reactions, or for *laser distillation* in which chemical enantiomers may be purified or interconverted using shaped laser pulses.

A long-standing control objective of the Nelson group has been to generate and observe very large amplitude vibrational displacements in ferroelectric crystals in order to characterize anharmonic (i.e. non-parabolic) contributions to their potential energy surface. The "holy grail" of such experiments would be to initiate sufficiently large ionic displacements that the crystals being studied would undergo collective structural change. This structural rearrangement could then be observed using various time-resolved spectroscopic methods, yielding valuable information underlying the mechanisms involved in the rearrangement. In ferroelectrics [18], which are ionic crystals possessing a permanent electric dipole within the unit cell, the sought after anharmonic components of the potential energy surface are known to strongly influence a number of properties of these materials that are of great technological importance. For instance, ferroelectric materials are widely used as piezoelectric transducers and actuators, insulators in high dielectric constant capacitors, ferroelectric random access memory (FRAM) in computers, and they are promising candidates for large-scale (many megabytes or larger) nonvolatile random access memory devices

widely anticipated in the computer industry. Although anharmonic potential energy contributions have been modelled theoretically [19], there has only been one report in the literature which has measured properties related to the nonlinear lattice potential in the frequency range of the vibrational modes of the crystal associated with its phase transition.

Unfortunately, it is not a simple task to generate the sought after large amplitude vibrational displacements in ferroelectric crystals. Since intense coherent sources of radiation are not available at the vibrational frequencies of interest, which occur in the 0.1-10 THz (10^{12} Hz) or far-infrared region of the spectrum, these vibrational modes are instead excited via ISRS with short laser pulses, as in the case of the vibrational modes of α-perylene. Unlike the case of the α-perylene, the vibrational modes of interest in ferroelectric crystals *propagate*, much like waves on a pond, such that they rapidly depart from their origin. Therefore, in order for multiple-pulse excitation schemes to be extended to generate large-amplitude ionic displacements in ferroelectric crystals, the excitation pulses must be spatially distributed such that they can "follow" the excitation they are trying to amplify.

With the motivation of creating large-amplitude ionic displacements in ferroelectric crystals, we have extended the methodology of femtosecond pulse shaping in order to produce highly structured optical waveforms with time-dependent spatial profiles. We refer to these methods as *two-dimensional femtosecond pulse shaping*. The development of these methods comprised a large amount of the work in this thesis and will be described in chapter 2. We begin with a review of the relevant background in one-dimensional pulse shaping, including a careful examination of commonly observed distortions in shaped pulses that have not treated comprehensively in the literature and that require detailed understanding in a number of applications. Next, we introduce 2D pulse shaping methods and their relationship to well known methods for shaping the transverse spatial profile of a laser beam. The final section of chapter 2 presents a powerful new diffraction-based approach to femtosecond pulse shaping that we will return to in the final chapter on coherent nonlinear optical spectroscopy.

Chapter 3 describes experiments in which the pulse shaping and beam shaping

methods of chapter 2 are applied to controlling propagating lattice excitations. These propagating lattice excitations are admixtures of lattice-vibrational and electromagnetic modes called *phonon-polaritons*. Simply put, they are part vibration and part light. We describe experiments in which two-dimensional pulse shaping methods are applied to the generation of large amplitude phonon-polaritons. Additional experiments are reported which make use of the electromagnetic component of phonon-polaritons to create a phased array source of THz radiation. Finally, a novel approach is described for the generation of arbitrarily shaped THz waveforms based on manipulation of the transverse spatial profile of a single excitation pulse, with possible applications in far-infrared spectroscopy and THz signal processing.

Chapter 4 presents a new approach to 2D *optical* spectroscopy [20] based on the pulse shaping methods described in chapter 2. Analogous to 2D IR spectroscopy, described above, 2D optical spectroscopy probes electronic resonances and should therefore reveal information regarding the coupling of chromophores, such as relative dipole orientations and energy transfer processes, on a subpicosecond timescale. Due in part to technical difficulties, however, coherent nonlinear optical spectroscopy has found less success than its counterpart in the infrared region of the spectrum. The experimental approach we present provides both a drastic simplification of the methods used for performing coherent nonlinear optical spectroscopy, overcoming many of the technical challenges in conventional approaches, and a tremendous expansion of the capabilities afforded by these methods. First, we will review the basic theoretical background in coherent nonlinear optical spectroscopy, using the simple approach of diagrammatic perturbation theory [21]. Next we will describe the experimental apparatus and elaborate its capabilities. Finally, results on three prototype systems will be used to illustrate the exciting possibilities with this powerful new method.

Chapter 2

Two-Dimensional Femtosecond Pulse Shaping

2.1   Introduction to Pulse Shaping

Efforts to control the temporal structure of individual laser pulses are almost as old as the pulsed laser itself. Early "pulse shaping techniques" were directed primarily towards generating shorter and shorter pulses rather than the production of sophisticated waveforms. The sizable spectral bandwidth of picosecond lasers made possible frequency domain pulse shaping techniques based on phase or amplitude modulation of the spectral components of the laser pulse [22] as well as acousto-optical or electro-optical time-domain methods [23]. With the advent of femtosecond lasers having even larger bandwidths (typically 6-100 nm), pulse shaping rapidly developed into its own field [24]. Led by the work of Weiner, Heritage, and co-workers [25], researchers have used various devices to shape femtosecond pulses, such as liquid crystal spatial light modulators [24], acousto-optic modulators [26], and deformable mirrors [27]. Other approaches employ space-to-time conversion [28], volume holography [29], or acousto-optic programmable dispersive filtering [30].

Femtosecond pulse shaping methods have been applied to diverse problems in, for example, spectroscopy [31], microscopy [15], laser control of matter [16, 17], laser pulse compression [32], telecommunications [33], and optical metrology [34]. A typical

experimental setup for pulse shaping apparatus is shown in fig. 2-1. A short (50 fs) laser pulse incident from the right is spectrally dispersed by a grating-lens pair. At the spectral plane, a computer-controlled liquid-crystal (LC) spatial light modulator (SLM) modulates the phase and/or amplitude of the dispersed laser spectrum. The modulated spectral components are then recombined by another grating-lens pair, producing an output waveform. The output waveform in this case is a series of 10 unevenly spaced pulses spread out over 6 ps. Note that the waveform shown in fig. 2-1 was created with a related diffraction-based apparatus, described in detail in section 2.8.

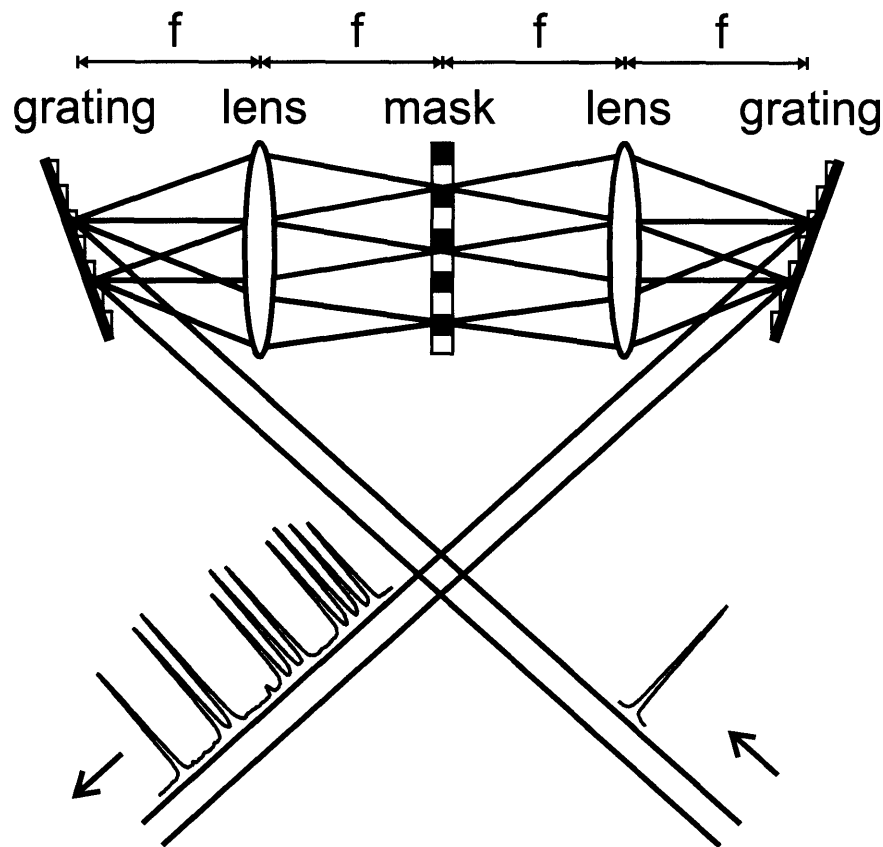Figure 2-1: Schematic illustration of experimental apparatus used for temporal-only pulse shaping. The input and output pulses shown here are actual measurements taken with a related diffraction-based pulse shaping apparatus described in section 2.8.

Most programmable femtosecond pulse shaping techniques reported to date only allow for control of the temporal profile of the output waveform. This can be thought

of as control over one dimension, the direction of propagation. We will refer to this type of temporal-only pulse shaping as *one-dimensional*. Two and three-dimensional pulse shaping techniques generate spatially and temporally shaped waveforms with different temporal profiles along one or two spatial coordinates perpendicular to the direction of propagation. Although some published experiments have demonstrated multidimensional spatiotemporal pulse shaping [35], none until recently have been able to generate high-fidelity multi-dimensionally shaped pulses in an automated fashion. In particular Nuss et al. [36] and Hill et al. [29] generated high-fidelity two and three-dimensional pulse shapes, respectively, using holographic techniques, but the potential applications of these techniques are restricted by their dependence on permanently recorded holograms. Koehl et al. [37] demonstrated programmable two-dimensional pulse shaping with an electrically addressed two-dimensional LC SLM. While the LC SLM was reconfigurable, the generation of arbitrary waveforms was problematic due to large interpixel gaps and an incomplete range of phase modulation values.

Much of the work in this thesis was dedicated to the development of methods for two-dimensional shaping of femtosecond laser pulses [38, 39, 40, 41], made possible by a newly developed optically addressed LC SLM. This chapter will review these two-dimensional femtosecond pulse shaping methods, including the necessary background on one-dimensional pulse shaping. Section 2.2 will describe the principles of operation, the performance, and procedures for the calibration of the LC SLM—the active element at the heart of the experiments described in this thesis. Section 2.3 will provide a brief description of methods used in this thesis to characterize two-dimensionally shaped laser pulses. In section 2.4, one-dimensional pulse shaping is analyzed, including a detailed study of the effects of nonlinear spectral dispersion and imperfections of LC SLMs on shaped pulses. Many researchers have noted the presence of replica pulses and other pulse distortions resulting from pixelation (or smooth pixel boundaries) of the LC SLM, but these effects have not yet been treated comprehensively. Coherent nonlinear optical spectroscopic experiments to be described in chapter 4 depend crucially on a detailed understanding of these waveform distortions

and methods for suppressing them.

Two-dimensional pulse shaping is introduced in section 2.5 with a technique we term *real-space shaping*. Real-space shaping essentially uses a two-dimensional LC SLM to independently shape many horizontal slices of the laser beam, which when taken together, form a coherent two-dimensional waveform. Waveforms shaped in this way were used to steer, focus, and amplify lattice excitations travelling at light-like speeds in ionic crystals, the topic of chapter 3. Section 2.6 briefly describes well-known methods for shaping the transverse spatial profile of a beam, often called *Fourier beam shaping*. In section 2.7, we return to two-dimensional pulse shaping with a technique we have termed *wavevector shaping* that is the combination of temporal-only pulse shaping and Fourier beam shaping methods. Wavevector shaping greatly expands the possibilities of two-dimensional pulse shaping, as it allows for the coherent redistribution of the laser pulse along the temporal and a single transverse spatial dimension. Section 2.8 introduces a new diffraction-based phase and amplitude pulse shaping method based on wavevector shaping. This diffraction-based pulse shaping approach has many beneficial characteristics, including the suppression of certain types of replica pulses, and the capability of generating multiple phase- and amplitude-shaped pulses outputs that may be used in applications such as coherent four-wave mixing spectroscopy, the topic of chapter 4.

Mathematical conventions and commonly encountered relations for Fourier transformation between frequency and time domains, and the less intuitive position and wavevector domains, are described in the appendix 1 (section 2.9). A list of commonly-used pulse shapes and how to make them is also included there.

2.2 Liquid Crystal Spatial Light Modulator

2.2.1 Jones-Matrix Analysis

Liquid-crystal (LC) spatial light modulators (SLMs) are the active elements used in most pulse shaping apparatuses to control the phase, or when used in combination

with a polarizer, the phase and amplitude of a light field. LC SLMs do this by imparting a variable birefringence $\Delta\phi(V)$, which can be controlled for each pixel. When a voltage V is applied to the LC SLM, the LC molecules align themselves with the applied field to a degree that depends on the strength of the applied field. The degree of alignment influences the index of refraction along the so-called c-axis but does not influence the index of refraction along the orthogonal axis. Therefore, an input light field polarized along the direction of the c-axis [see fig. 2-2(a)] is shifted by $\Delta\phi$.
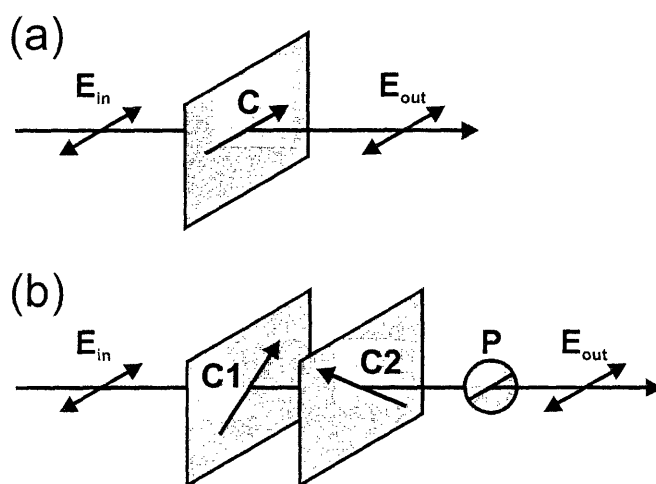
Figure 2-2: (a) Horizontally-polarized input light field incident upon a LC SLM with c-axis in the horizontal plane. (b) Horizontally-polarized input light field incident upon two LC SLMs in series followed by a polarizer.

All of the experiments reported here made use of the single-mask arrangement shown in fig. 2-2 (a).The commonly used dual-mask LC SLM arrangement consists of two (1D) LC SLMs in series followed by a polarizer, as illustrated in fig. 2-2(b). The two LC layers have orthogonal c-axes and the input light field is polarized at 45-degrees relative to either c-axis. Since we will later refer to the ability of the dual-mask LC SLM to independently control the phase and amplitude of the output light field [42, 31], we will take a moment now to mathematically analyze this capability using a simple Jones matrix formalism. The horizontally-polarized input light field is given by the vector E_{in}, and the modulator, polarizer, and rotation matrices are given by $M(\Delta\phi)$, P_x, and $R(\theta)$, respectively.

$$E_{in} = \begin{pmatrix} 1 \\ 0 \end{pmatrix} \qquad M(\Delta\phi) = \begin{pmatrix} \exp(i\Delta\phi) & 0 \\ 0 & 1 \end{pmatrix}$$

$$P_x = \begin{pmatrix} 1 & 0 \\ 0 & 0 \end{pmatrix} \qquad R(\theta) = \begin{pmatrix} \cos\theta & \sin\theta \\ -\sin\theta & \cos\theta \end{pmatrix} \qquad (2.1)$$

The induced birefringence $M(\Delta\phi)$ in eq. 2.1 applied by the LC SLM is expressed in its own coordinate system, using the c-axis and the perpendicular axis within the plane of the LC SLM. In the x-y basis (laboratory horizontal and vertical), the modulation applied by the LC SLM is $R(-\theta)M(\phi_1)R(\theta)$, where θ is the angle between the laboratory x-axis (horizontal) and the LC c-axis. The output light field E_{out} corresponding to the dual-mask arrangement shown in fig. 2-2(b) is therefore given by

$$E_{out} = P_x R(\pi/4) M(\Delta\phi_2) R(-\pi/4) R(-\pi/4) M(\Delta\phi_1) R(\pi/4) E_{in}. \qquad (2.2)$$

This can be simplified to give the output field

$$E_{out,x} \propto P_x \exp[i(\phi_1 + \phi_2)/2] \begin{pmatrix} \cos[(\phi_1 - \phi_2)/2] \\ i\sin[(\phi_1 - \phi_2)/2] \end{pmatrix}. \qquad (2.3)$$

In the case when the polarizer is used as shown in fig. 2-2(b), the horizontally-polarized output field has an amplitude determined by the difference of the birefringences of the two masks $\Delta\phi_1 - \Delta\phi_2$ while the phase is determined by the sum of the birefringences $\Delta\phi_1 + \Delta\phi_2$. Thus, the dual-mask arrangement allows for independent phase and amplitude control over the light field that is transmitted through the polarizer [42, 31]. In the case when the polarizer is removed from the apparatus, the result is an arbitrary elliptical state of polarization. This arrangement was originally proposed for polarization pulse shaping by Wefers in [42] in order to generate pulse shapes whose polarization state is varied as a function of time. The method has

been further developed, especially by Brixner and coworkers [43, 44, 45, 46, 47], and applied to a number of coherent-control experiments in which vectorial properties of light were exploited, for example [48, 49, 50, 51].

2.2.2   Hamamatsu 2D LC SLM

The 2D LC SLM used in these experiments, Hamamatsu model SLMM X7550-800, is optically addressed from the back by light emitted from a 660 nm, 30 mW laser diode (see fig. 2-3). A conventional transmission mode 2D LC mask is used to attenuate the light from the laser diode in a specified, spatially varying manner. The light transmitted by the LC mask is then incident upon a photoconductive semiconductor layer that converts the incident light to a voltage such that a variable voltage may be applied to different regions of the LC SLM. The LC SLM itself contains no pixels but consists instead of a uniform nematic LC layer that is driven by a voltage corresponding to the incident laser diode light intensity. Due to the pixelation of the active LC matrix, there are effectively 480×480 regions (which we will still refer to as pixels for the sake of convenience) on the nematic layer, each 40×40 microns in size. A 1000 Hz, 2.5 or 3 VAC square wave (5 or 6 V peak-peak) voltage was applied to the LC SLM in all the measurements described here. The response of the LC SLM is strongly dependent on the biasing voltage and frequency.
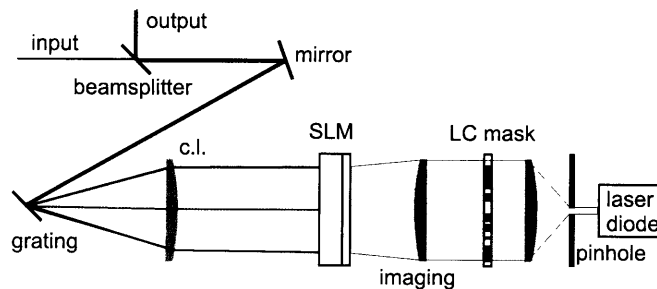

Figure 2-3: The pulse shaping arrangement is similar to conventional $4f$ spectral filtering arrangements, except that a two-dimensional LC SLM in a reflection geometry is employed. The LC SLM is optically addressed by imaging a conventional transmissive liquid crystal array onto a photoconductive layer.

The extent of pixelation and interpixel region size of an LC SLM are important

characteristics influencing the quality and variety of pulse shapes obtainable with it. Wefers [31] showed that a pixelated LC SLM creates unwanted spatial and temporal replica pulses due to interpixel gaps. For one-dimensional LC SLMs, these effects are usually tolerably small since the fill factor is typically over 95%. In the case of electrically addressed two-dimensional SLMs, the fill factor is only on the order of 60% due to conducting structures on the mask necessary to address the different pixels. For example, Koehl et al. [37] found that the large interpixel gaps (as well as a limited phase modulation range) in their electrically addressed transmission-mode 2D LC SLM not only reduced the overall transmission but also severely restricted the quality of the waveforms produced. Recently, electrically-addressed pixelated reflection-mode 2D LC SLMs have become available with a fill factor of 85% or better, (for instance, HOLOEYE Photonics AG, model LC 2002). Although there have been no reports using this new generation of pixelated reflection-mode 2D LC SLMs, they are promising devices for pulse shaping applications.

One way to reduce the effects of pixel gaps is to use an optically addressed LC SLM with an imaging arrangement designed to smooth out the interpixel regions. This technique was demonstrated by Dorrer et al. in the case of a one-dimensional pulse shaper used to correct for higher order phase distortions [52]. The cutoff frequency of the modulation transfer function of their LC SLM was relatively low, allowing for very smooth transitions between neighboring "regions" of the LC SLM (much smoother than for the Hamamatsu LC SLM).

The present LC SLM is optically addressed in such a way as to reduce pixelation effects while preserving the ability to produce highly sophisticated waveforms. To measure the extent of pixelation of the current LC SLM the birefringence response of the SLM was imaged to a CCD. The incident light was polarized at 45 degrees with respect to the LC SLM edges and the CCD was equipped with a −45 deg polarizer. By this means, the setup converted any change of the polarization into a modulation of the intensity. The transmission liquid crystal array (see fig. 2-3) is controlled by the VGA output of a computer, which operates in a grey mode with 8-bit resolution. Each of the 256 greyscale values may then be addressed by creating the appropriate

image with the computer to be sent to the LC SLM.
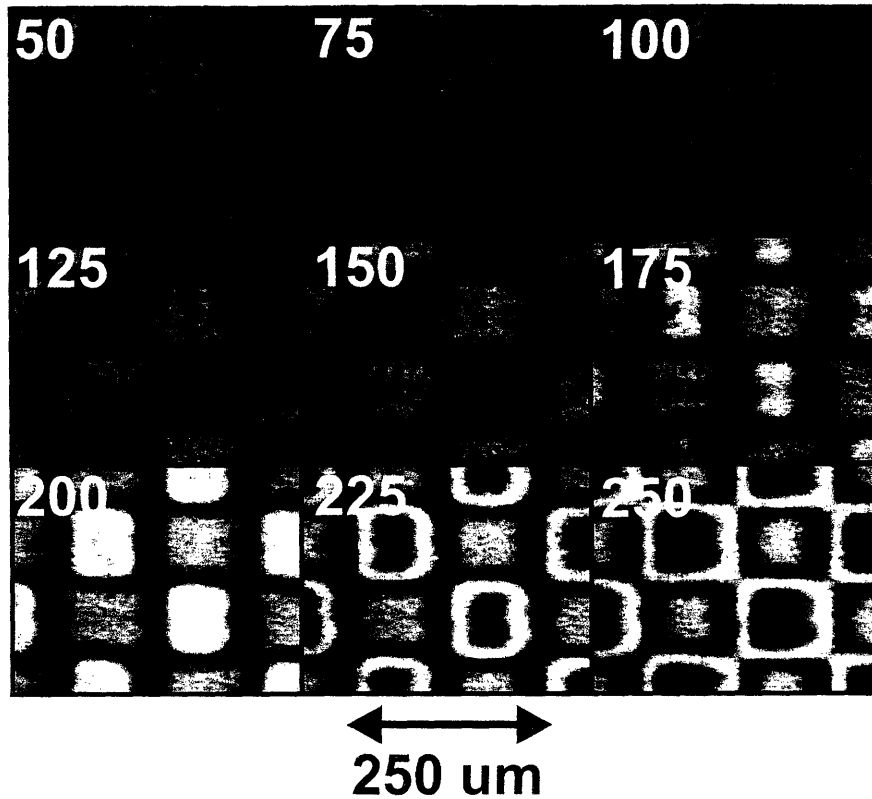
Figure 2-4: Intensity-modulation images of the Hamamatsu LC SLM, indicating pixelation and pixel smoothing when a checkerboard phase pattern consisting of 3×3 pixel blocks was applied to the Hamamatsu LC SLM. Images are shown for greyscale values of 50, 75, 100, 125, 150, 175, 200, 225, and 250, which covers a phase range slightly in excess of 2π radians.

Figure 2-4 shows a series of 9 images illustrating the extent of pixelation and pixel smoothing in the Hamamatsu LC SLM. The phase pattern applied was in the shape of a checkerboard, where each square of the checkerboard consisted of a 3×3 block of LC SLM pixels. Half of the blocks were scanned through a range of greyscale values (0-255) while the other half of the blocks were set to a greyscale value of 0. All pixel blocks begin at the same intensity, after which the pixel blocks that are scanned first grow darker (100) then brighter (200) and then darker once more (250). This behavior is expected as the polarization of the light reflected from the scanned pixel blocks rotates to be first crossed relative to the polarizer (100), then aligned with the polarizer (200) and then crossed again (250). [See fig. 2-7(a) for a plot illustrating

27

the response of a single region of the LC SLM.] The 3×3 pixel blocks are clearly visible in fig. 2-4, although the pixel blocks are not sharply defined. Instead, there are continuous transitions between adjacent pixel blocks, which smooth out the gaps that would otherwise occur between pixels. This compromise between the smoothing of gaps and the preservation of pixel resolution results in a device that overcomes the otherwise crippling limitations of transmission-based 2D LC SLMs.

Generally, the effect of pixel smoothing is that the phase at any given pixel is dependent upon those surrounding it. As such, phase patterns that involve a single pixel behaving differently from its neighbors deviates from the expected values. This can be seen in fig. 2-5, where the phase response of the LC SLM was determined for pixel blocks of different sizes against a zero background to illustrate the effect of pixel smoothing on the phase response. The 1×1 pixel region (blue) has a much smaller phase response than that of the 3×3 and 6×6 pixel blocks. This smoothing effect can cause pulse distortions, as will be discussed further in section 2.4. Differences between the phase responses of the 3×3 and 6×6 pixel blocks are within the uncertainty of these measurements. More careful measurements are performed for calibration of the SLM, as will be described in the next section.
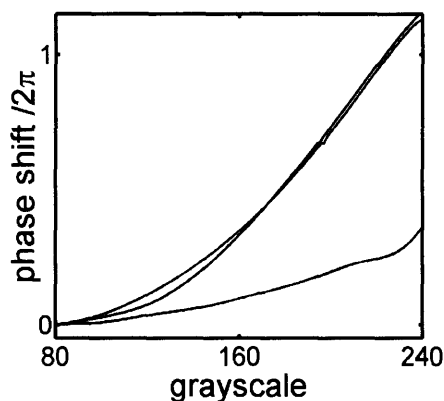
Figure 2-5: Phase response of the LC SLM as the applied greyscale value is scanned from 80-240, for regions of 1×1 pixel (blue curve), 3×3 pixels (green curve), and 6×6 pixels (red curve). The response of the 1×1 pixel region is smaller than that of the 3×3 and 6×6 pixel regions due to pixel smoothing.

2.2.3 Calibration of the LC SLM

Up to 256 phase retardation levels, or greyscale values, are available at each pixel of the liquid crystal mask, although only about 120 are used in practice as will be seen below. The phase modulation of the LC SLM as a function of the greyscale value was calibrated with intensity modulation via birefringence as well as interferometry using pulsed 800 nm light. While early experiments made use of the birefringence data, recent experiments have shown that the interferometric calibration is more accurate.
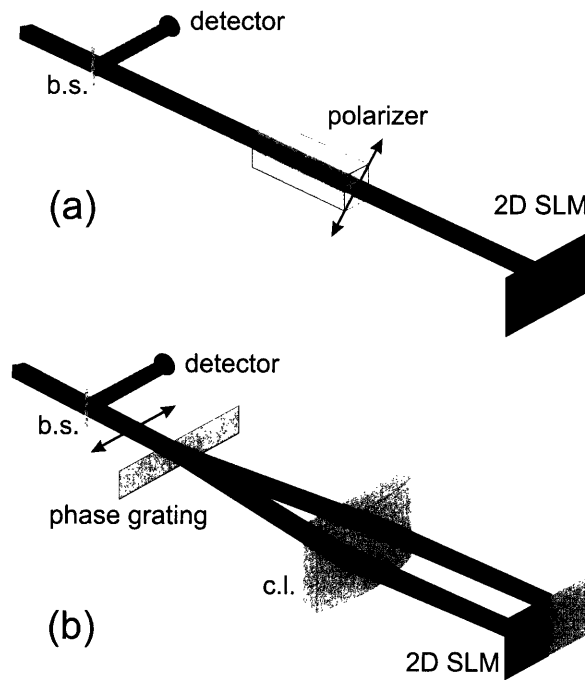
Figure 2-6: (a) Intensity calibration. The SLM rotated the polarization of the input light such that the reflected light, after passing through the polarizer a second time, is modulated in intensity. (b) Interferometric calibration. The light was split into mainly two diffraction orders and reflected by the SLM. One half of the LC SLM was scanned through the full range of phase modulation values possible while the other half of the SLM applied no phase modulation. The detector measured the interference of the two diffraction orders after they were recombined.

The setup for intensity modulation via birefringence is illustrated in fig. 2-6 (a). Light polarized at 45 degrees with respect to the liquid crystals was incident upon the LC SLM, reflected, and then separated out with a beam splitter. This converted a rotation of the polarization to a modulation in the intensity of the beam. The

29

intensity of the modulated light was recorded for the range of possible LC mask greyscale values and related to the phase shift [fig. 2-7 (a) and (b)].

The setup for interferometric calibration of the LC SLM is depicted in fig. 2-6 (b). Light with polarization parallel to the liquid crystals was split mainly into ±1 orders by a transmissive binary phase mask (transmissive diffraction grating) and then focused onto the LC SLM. The reflected light retraced its path until it was picked off by a beam splitter and measured by a photodiode. The phase of the light in one of the arms of the interferometer was modulated by scanning one half of the SLM through the full range of greyscale values while not adjusting the other half. The interference of the combined beams was then recorded as a function of greyscale, generating a plot of phase modulation vs. liquid crystal greyscale value [fig. 2-7 (c) and (d)]. The phase-mask based interferometer has the benefit that it employs common-path optics which greatly reduces phase noise due to vibrations in the optical mounts, etc.

Extracting the applied birefringence [in the case of 2-7(a)] or the applied phase shift [in the case of 2-7(c)] is a simple task. Greyscale values corresponding to phase shifts of 0, π, and 2π are identified in the raw data [the extrema in fig. 2-7(a) and (c)], and then the phase shifts are calculated by inverting eq. 2.4 piecewise across the ranges $0 - \pi$ and $\pi - 2\pi$ to determine the dependence of $\Delta\phi$ on the applied greyscale value g. In order to smooth out the noise apparent in the calibration curve, the raw data [fig. 2-7(a) and (c)] were first fit to a high-order (14th) order polynomial. This polynomial was then evaluated over the greyscale range of interest and finally inverted. The intensity modulation and interferometric calibration differ by a constant phase shift but are otherwise in good agreement and show that the device is able to modulate the phase of 800 nm light between 0 and 2π radians. This phase offset is due to a slight phase difference in one of the arms of the interferometer for the interferometric measurement. Depending on this phase offset, it may be more appropriate to use a sin function in eq. 2.4.

$$I(g) = \frac{1}{2}\left(1 + \cos[\Delta\phi(g)]\right) \qquad (2.4)$$

Note that equation 2.4 has been written explicitly for the case of the interferometric calibration. For the birefringence calibration it is only necessary to substitute sin for cos. This substitution is required since the two measurements differ by a constant phase that is the result of an offset within the interferometer. The relatively smooth calibration curves [2-7(b) and (d)] could then be fit well by a 4th order polynomial so that the greyscale value required for a desired phase shift could be easily calculated with our homemade driver software. Use of the polynomial fit to the calibration curve obviated the need for a lookup table, streamlining the process of calculating the greyscale mask pattern from the desired phase pattern.
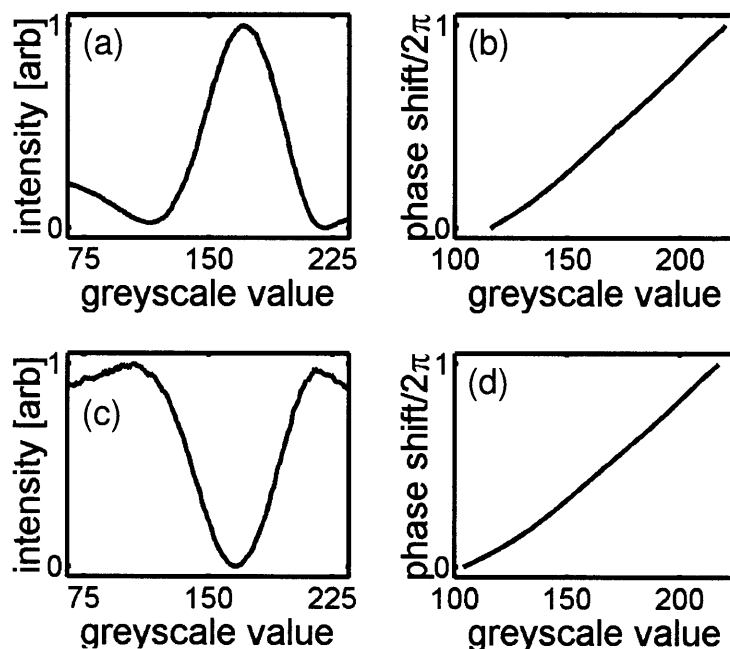
Figure 2-7: LC SLM calibration. Raw data (a) and (c) for birefringence and interferometric measurements, respectively. (b) and (d) corresponding calibration curves.

In experiments, the same phase calibration was used for all wavelengths, although this is expected to introduce small phase errors, as pointed out in [53] and [54]. The above calibration measurements were performed with a femtosecond Ti:sapphire oscillator of approximately 35 nm bandwidth. As such, the calibrations measured something like the average phase shift, or the phase shift at the center wavelength, λ_o. Therefore, assuming a constant index of refraction for a given pixel of the LC SLM at a given applied voltage V, the applied phase modulation is a function of

31

wavelength according to $\Delta\phi(V,\lambda) = \Delta\phi(V,\lambda_o)\lambda_o/\lambda$. Correction of this $1/\lambda$ phase error is then a simple matter of multiplying the desired phase at the calibrated center wavelength by the factor λ/λ_o. Although simulations have shown that the effects of these errors on output pulse shapes are relatively small, it should be straightforward to remedy in future experiments. Alternately, the phase shift could be calibrated at many different wavelengths.
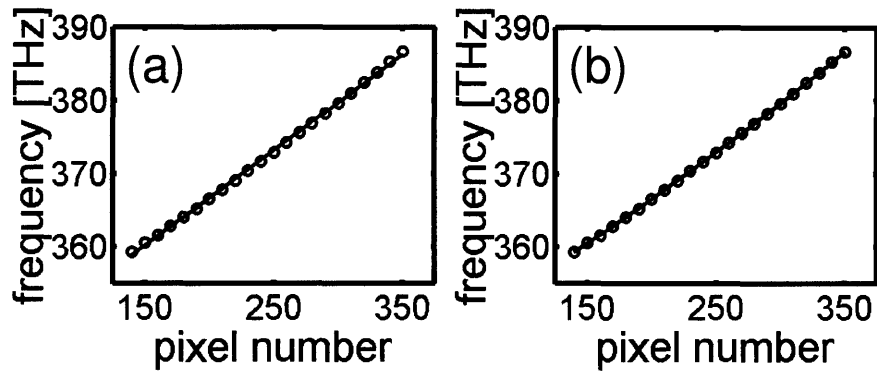
Figure 2-8: Frequency calibration data (points) and best fit to a line (a) and a second-order polynomial (b). The nonlinear character of the spectral dispersion is clearly visible and has to be incorporated when addressing the LC SLM.

An additional calibration step that is important for the pulse shaping apparatus is to accurately correlate the LC SLM pixels with the corresponding frequency components dispersed by the grating-lens pair, as pointed out in [53, 54, 55, 56] and elsewhere. The nonlinear spectral dispersion, to be expected from a grating-lens pair, was measured as follows. The polarization of the input beam was rotated by 45 degrees with respect to the SLM and the reflected beam was sent back through the polarizer and then to a spectrometer, in a setup nearly identical to the one shown in fig. 2-6 (a). By setting the phase modulation of the SLM to π radians along a vertical strip and zero everywhere else, all wavelengths but those impinging upon the vertical strip are rejected by the polarizer, and the wavelength corresponding to the peak of the transmitted output pulse can then be identified with a spectrometer. The center frequency of the peak intensity was then recorded as a function of the pixel position of the vertical strip on the LC SLM. An example of the measured spectral dispersion at the LC SLM is shown in fig. 2-8 (circles), where careful examination of the data

reveals that the dispersed frequency components do not fit well to a line (a) but do fit well to a quadratic polynomial (b). If a linear spectral dispersion is simply assumed, the output waveforms are distorted as has been shown in references [57, 54]. Furthermore, nonlinear spectral dispersion plays an important role in suppressing unwanted replica pulse features in the output waveforms. These points will be discussed further in section 2.4.

2.3 Shaped-Pulse Characterization

Characterization of ultrashort pulses requires specialized methods since there do not exist detectors with sufficiently fast response times to directly monitor ultrashort pulses. There are almost as many pulse characterization methods as there ultrafast research groups, each with its own approach and acronym: SPIDER [58]; FROG [59]; TADPOLE [60]; POLLIWOG [61]; GRENOUILLE [62]; PICASO[63]; STRUT [64]; etc. Many of these methods rely upon comparison of one pulse with another to extract detailed information about both the phase and the amplitude of the ultrashort pulse being measured. For most of the work in this thesis, however, we have used a relatively straightforward scheme known as non-collinear (or background-free) second harmonic generation (SHG) cross correlation, which we will simply refer to as cross-correlation.
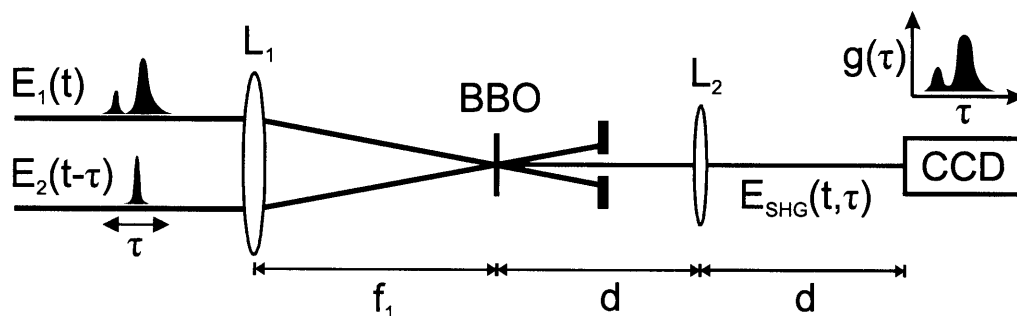

Figure 2-9: Schematic of SHG cross-correlation apparatus. Shaped pulse $E_1(t)$ and reference pulse $E_2(t)$ are focused into a BBO crystal, creating a SHG correlation signal (blue) whenever the pulses overlap in time.

For our SHG cross-correlation measurements we typically correlate a short laser pulse with a shaped laser pulse at variable time delays, as shown schematically in

fig. 2-9. An unknown pulse $E_1(t)$ and a reference pulse $E_2(t - \tau)$ with a variable delay τ are focused by a lens L_1 into a thin SHG crystal, typically beta barium borate (BBO). Note that the intensities rather than amplitudes of the unknown and reference pulse are being used since background-free SHG cross-correlation measurements are insensitive to temporal phase. The variable delay τ is controlled by changing the optical path length that the reference pulse travels with a computer-controlled motorized delay stage. When the two pulses are time-coincident in the SHG crystal, a third beam with twice the frequency (shown in blue) is generated. This third beam may be detected with an ordinary photodetector such as a photodiode, photomultiplier tube, or charge-coupled device (CCD) camera. The detector then records the time-integrated intensity of the second-harmonic beam for different reference pulse delays, building up a correlation trace. Simply put, the correlation trace is a slightly temporally broadened measurement of the shaped pulse. Mathematically, the SHG correlation trace $g(\tau)$ is given by

$$g(\tau) = \int_{-\infty}^{\infty} I_1(t) I_2(t - \tau) dt, \qquad (2.5)$$

where $I_1(t)$ and $I_2(t)$ are the intensities of pulses $E_1(t)$ and $E_2(t)$, respectively ($I(t) \propto |E(t)|^2$).

In order to measure time-dependent spatial profiles, we use two variations on SHG cross-correlation, which we call spatially-resolved cross-correlation and angle-resolved cross-correlation. For both methods an approximately 1 cm tall reference pulse is used in combination with a CCD camera for detection in order to simultaneously record cross-correlation information at many different heights within the unknown pulse. Spatially-resolved cross-correlation uses lens L_2 to image (1 : 1, where $d = 2f_2$, with d as defined in fig. 2-9) the correlation beam generated in the SHG crystal. Angle-resolved cross-correlation uses lens L_2 to Fourier-transform ($d = f_2$) the correlation signal (see section 2.6), producing the wavevector-distribution of the correlation beam on the CCD camera. These two methods will be discussed further below in the contexts of the measurements.

A variation of the intensity cross-correlation that we also use is SHG frequency-resolved optical gating (FROG). Trebino et al. have written an excellent, comprehensive review of FROG techniques [59]. The apparatus for SHG FROG is nearly identical to the apparatus for SHG intensity cross correlation, with the exception that a spectrometer is used for detection of the correlation signal. When a known reference pulse and an unknown pulse are used, as in the cross-correlation measurement, the method is termed XFROG (or cross-correlation FROG). In our case, we typically use conventional SHG FROG, where both of the input beams are replicas of the unknown pulse (created with a beamsplitter). Using an iterative phase-retrieval method (commercial software to do this is available through Femtosoft Technologies), the phase and intensity of the unknown pulse can be determined in both the time and the frequency domains. Analytically, the FROG signal is given by

$$f(\nu, \tau) = \left| \int_{-\infty}^{\infty} E_1(t) E_2(t - \tau) \exp(-i2\pi\nu t) dt \right|^2 . \tag{2.6}$$

Figure 2-10 shows a FROG measurement and retrieval of a nominally 40 fs laser pulse. The original measurement is shown in (a). Using the retrieval software, a reconstructed FROG trace was generated (b) with an error of 0.002 on a grid of 1024 x 1024 points. The extracted spectral intensity and phase are shown in (c), indicating the presence of a weak quadratic/cubic/quartic spectral phase. The temporal field amplitude and phase are shown in (d). As with the spatially-resolved SHG cross-correlation measurement technique, it is also possible to perform SHG FROG measurements in a spatially resolved manner, as will be described further in section 2.7.

Once a FROG measurement has been used to characterize the phase and amplitude of a laser pulse, that pulse may then be used to characterize an unknown pulse using a method called spectral interferometry [65, 66]. In spectral interferometry, an unknown and a well-characterized reference laser pulse are combined and sent into a spectrometer where they interfere with each other. The difference in phase between the two pulses creates interference fringes which may then be detected and used to
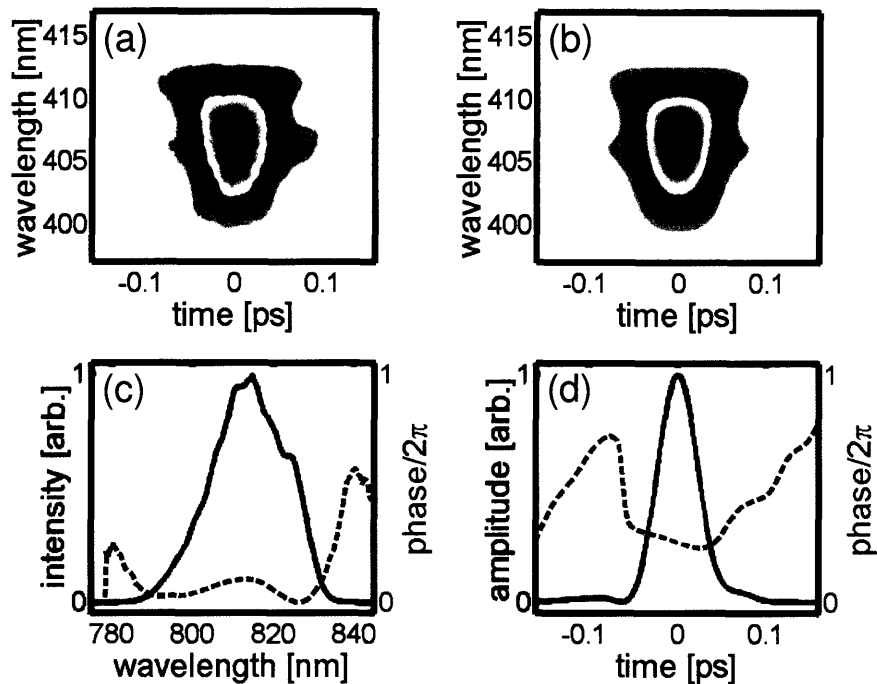
Figure 2-10: FROG measurement of an unshaped 40 fs laser pulse. (a) Original FROG data. (b) Reconstructed FROG trace. (c) Retrieved spectral intensity and phase. (d) Retrieved electric field amplitude and phase.

characterize the unknown pulse. Spectral interferometry has the advantages that the unknown pulse may be characterized in a single shot, (without scanning a delay line as with the FROG measurement), and that it is a linear measurement that can be performed on very weak unknown pulses. In one paper by Fittinghoff et al. [60], unknown pulses of energy 42 zeptoJoules (42×10^{-21} J) were characterized by this method.

The reference pulse is delayed (or advanced) by τ from the unknown pulse in order to create spectral fringes that are then used in characterizing the phase difference between the two pulses. Two identical pulses that are delayed by τ will have spectral fringes with a period of $\nu = 1/\tau$, where ν is frequency (not to be confused with angular frequency ω, where $\omega = 2\pi\nu$). Deviations from the expected $1/\tau$ fringe pattern reveal phase differences between the two pulses. A second measurement is then required to determine the amplitude of the unknown pulse, although this measurement may be done in parallel with the measurement of the fringes when using a dual-channel

spectrometer. Mathematically, spectral interferometry is described as

$$I_{meas}(\nu) \propto |E_{ref}(\nu) + E_{unk}(\nu)|^2 \tag{2.7}$$

$$\propto |E_{ref}(\nu)|^2 + |E_{unk}(\nu)|^2 + 2|E_{ref}|(\nu)|E_{unk}(\nu)| \cos(\Delta\phi(\nu)), \tag{2.8}$$

where $I_{meas}(\nu)$ is the intensity of the measured spectral interferogram, $E_{ref}(\nu)$ and $E_{unk}(\nu)$ are the fields of the reference and unknown pulses, and $\Delta\phi(\nu)$ is the phase difference between the reference and unknown pulses.

Figure 2-11 illustrates four measurements of an unknown pulse by spectral interferometry, where the reference pulse arrived 3.35 ps after the unknown pulse. Different spectral phases were applied to the unknown pulse with a diffraction-based pulse shaping apparatus (see section 2.8), spectral interferometry was used to reconstruct the applied phase. In (a), the fringes are closer together than expected, indicating a larger delay between the unknown and the reference pulses, whereas in (b), the fringes are further apart than expected, indicating that the delay decreased between the unknown and shaped pulses. The extracted linear spectral phase (blue lines) is in excellent agreement with the desired linear spectral phase (red lines). In (c) and (d), quadratic spectral phases (with opposite signs) have been used to "chirp" the unknown pulse such that the pulse has a time-dependent frequency with either the high frequency components arriving after the low frequency components (positive chirp) or before the low frequency components (negative chirp). The applied spectral phase was $\phi(\nu) = \pm 0.56(\nu - \nu_o)^2$, where ν is in THz and the center frequency $\nu_o = 378.2$ THz. The fringes are closer together in (c) on the low frequency side of the spectrum than they are on the high frequency side of the spectrum since the low frequency components have been shifted to later times (closer to the reference pulse) whereas the high frequency components have been shifted to earlier times (further from the reference pulse). The opposite scenario is true in (d). As before, the extracted spectral phase is in excellent agreement with the applied spectral phase in (c) and (d).
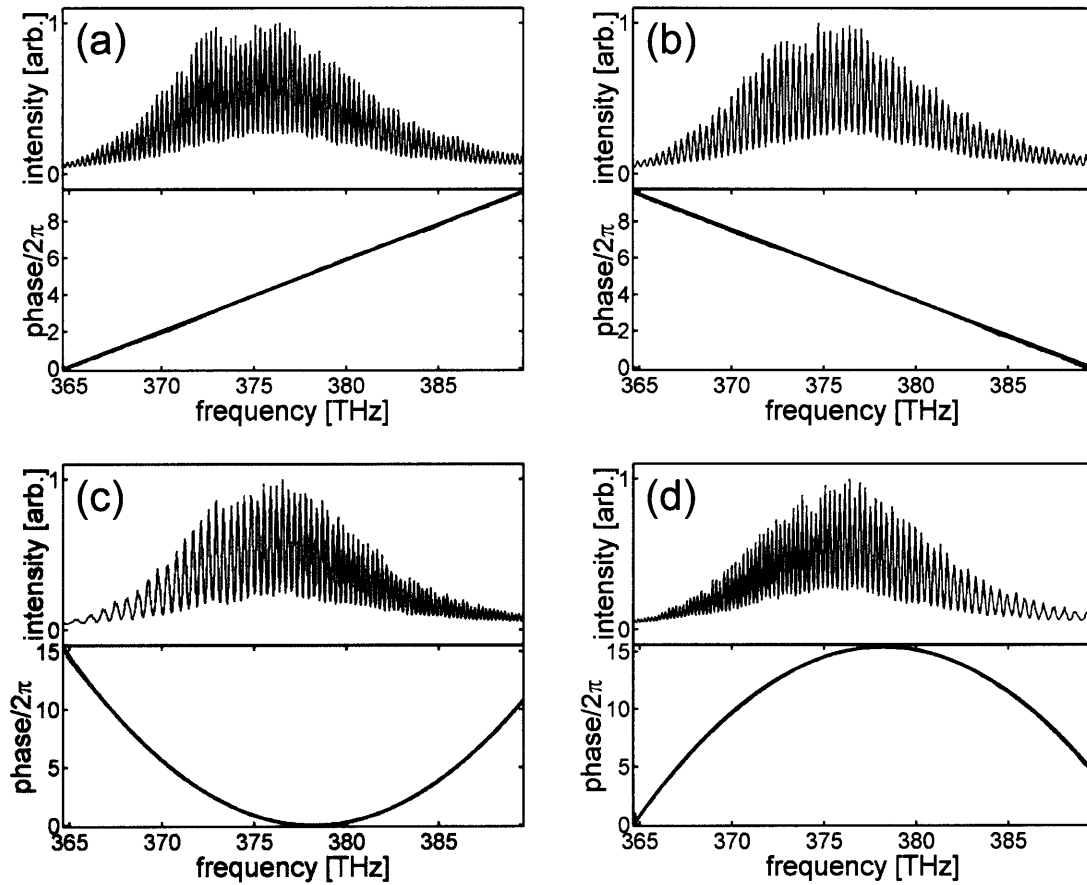
Figure 2-11: Measured spectral interferograms (top subpanels) and extracted/measured spectral phase (bottom, blue/red) for 4 different unknown pulses. Unknown pulse shifted to be 0.4 ps earlier (a) and 0.4 ps later (b) than expected with application of a linear spectral phase. Negatively (c) and positively (d) chirped pulses through application of a positive or negative quadratic spectral phase.

2.4 One-Dimensional Pulse Shaping

Most temporal pulse shaping schemes demonstrated to date manipulate the phase and/or amplitude of a broad-bandwidth input laser pulse in order to create a desired time-dependent optical waveform, as shown in fig. 2-1. Mathematically, the modulated laser spectrum can be described as the product of the input laser pulse $E_{in}(\nu)$ and the spectral modulation $M(\nu)$ applied by the pulse shaping apparatus, giving

$$E_{out}(\nu) = M(\nu)E_{in}(\nu), \tag{2.9}$$

or equivalently, via the convolution theorem,

$$e_{out}(t) = m(t) \otimes e_{in}(t). \tag{2.10}$$

In this section, we will evaluate different aspects of the above equations for temporal-only pulse shaping with pixelated LC SLMs. After a simplified but illustrative analysis of temporal-only pulse shaping with a hypothetical apparatus, we will proceed to the analysis and demonstration of actual experimental implementations. Detailed attention will be paid to waveform distortions resulting from the pixelation of the LC SLM as well as imperfections in the LC SLM. These waveform distortions have important consequences for the application of two-dimensional pulse shaping to coherent nonlinear optical spectroscopy, as will be discussed in chapter 4. Furthermore, the influence of nonlinear dispersion of the spectrum on these waveform distortions (see fig. 2-8) will be carefully considered.

2.4.1 General Analysis

An ideal LC SLM consists of N sharply defined pixels separated by a distance of Δx, with no gaps present between the pixels. The LC SLM may then independently modulate the phase (for a single mask LC SLM) or the amplitude and phase (for a dual-mask LC SLM) of the spectrally dispersed laser pulse. The modulating function $M(x)$ is then simply the convolution of the spatial profile $S(x)$ of a given spectral component (determined by the input beam spatial profile and the lens focal length) with the phase and amplitude modulation applied by the LC SLM,

$$M(x) = S(x) \otimes \sum_{n=-N/2}^{N/2-1} \text{squ}\left(\frac{x - x_n}{\Delta x}\right) A_n \exp(i\phi_n), \tag{2.11}$$

where x_n is the position of the nth pixel, A_n and ϕ_n are the amplitude and phase modulation applied by the nth pixel, Δx is the separation of adjacent pixels, and where the top-hat function $\text{squ}(x)$ is defined as

$$\text{squ}(x) = \begin{cases} 1 & |\, x \,| \le 1/2 \\ 0 & |\, x \,| > 1/2 \end{cases}. \qquad (2.12)$$

Assuming a linear spectral dispersion given by $\Omega_n = n\Delta\Omega$, where $\Omega_n = \nu_n - \nu_o$ and $\Delta\Omega$ is the frequency separation of adjacent pixels corresponding to Δx, and assuming that the spatial profile of a given spectral component is a Gaussian function $S(x) = \exp(-x^2/\delta x^2)$, the modulation function may be written as

$$M(\Omega) = \exp(-\Omega^2/\delta\Omega^2) \otimes \sum_{n=-N/2}^{N/2-1} \text{squ}\left(\frac{\Omega - \Omega_n}{\Delta\Omega}\right) A_n \exp(i\phi_n). \qquad (2.13)$$

Here, the width of the Gaussian function has been expressed in terms of $\delta\Omega$, the spectral resolution of the grating-lens pair, where $\delta\Omega = \delta x \Delta\Omega/\Delta x$. The spot size δx (measured as full-width at $1/e$ of the intensity maximum, assuming a Gaussian input beam) is dependent upon the input beam diameter and lens focal length as $\delta x = 4\pi F/\lambda D$. If we assume that the input laser pulse is bandwidth-limited (that the spectral phase is flat), we can then approximate the input laser pulse as

$$E_{in}(\Omega) = \sum_{n=-N/2}^{N/2-1} \text{squ}\left(\frac{\Omega - \Omega_n}{\Delta\Omega}\right) B_n, \qquad (2.14)$$

where B_n is the spectral amplitude of the input laser pulse at the nth pixel. Substitution of the above expressions for $M(\Omega)$ and $E_{in}(\Omega)$ into eq. 2.9 yields

$$E_{out}(\Omega) = \exp(-\Omega^2/\delta\Omega^2) \otimes \sum_{n=-N/2}^{N/2-1} \text{squ}\left(\frac{\Omega - \Omega_n}{\Delta\Omega}\right) A_n B_n \exp(i\phi_n). \qquad (2.15)$$

Finally, Fourier transformation of $E_{out}(\Omega)$ yields an expression for the output of the pulse shaping apapratus,

$$e_{out}(t) \propto \exp(-\pi^2 \delta\Omega^2 t^2)\text{sinc}(\pi\Delta\Omega t) \sum_{n=-N/2}^{N/2-1} A_n B_n \exp[i(2\pi\nu_n t + \phi_n)]. \qquad (2.16)$$

The term in the summation in eq. 2.16 describes the basic properties of the output pulse, such as would be obtained by modulating the amplitude and/or phase of the input pulse at the points $\Omega_n - n\Delta\Omega$ with a grating-lens apparatus that has perfect spectral resolution. The sinc term is the Fourier transformation of the top-hat pixel shape, where the width of the sinc function is inversely proportional to the pixel separation Δx, or equivalently, $\Delta\Omega$. The Gaussian term results from the finite spectral resolution grating-lens pair, where the width of the Gaussian function is inversely proportional to the spectral resolution $\delta\Omega$. Use of a LC SLM with a larger number of pixels over the same distance decreases Δx and therefore increases the width of the sinc function. As the pixel separation Δx decreases to be less than the spot size of a frequency component at the spectral plane, δx, the additional pixels do not result in a larger temporal range over which pulses may be shaped due to the Gaussian function that approaches zero at early and long times. Collectively, the Gaussian-sinc term is known as the time window.

While eq. 2.16 provides a compact and useful analytical result, it neglects three important limitations of LC SLMs. First, LC SLMs typically have a phase range that is only slightly in excess of 2π. Fortunately, since phases that differ by 2π are mathematically equivalent, the phase modulation may be applied modulo 2π. Thus, whenever the phase would otherwise exceed integer multiples of 2π, it is "wrapped" back to be within the range of $0 - 2\pi$. Second, the pixels of the LC SLM are not perfectly sharp, and there are gap regions between the pixels whose properties are usually somewhat intermediate between the adjacent pixels. Although smoothing of the pixelated phase and/or amplitude pattern would in general sound desirable, when it is combined with the phase-wraps, spectral phase or amplitude distortions are introduced at phase-wrap points, as will be shown below. Third, while the pixels are evenly distributed in space, the frequency components of the dispersed spectrum

are not, creating a nonlinear pixel to frequency mapping such as was shown in fig. 2-8. These three considerations make the determination of an exact analytical expression for $M(\Omega)$ difficult. Instead, we will formulate a general expression for $M(x)$ and then specify a procedure whereby a computer may be used to help evaluate the generated output pulse.

The finite spatial response of the LC SLM may be accounted for by smoothing the applied phase. Although the exact nature of the smooth pixel boundaries is not known, it can be approximated by convolving a spatial response function $L(x)$ with an idealized phase modulation function that would result in the case of sharply defined pixel and gap regions. For a phase-only LC SLM (section 2.2) with pixels separated by Δx and gaps of width w, the applied phase modulation is given by

$$
\phi(x) = L(x) \otimes \sum_{n=-N/2}^{N/2-1} \left\{ \mathrm{mod}[\phi_n, 2\pi]\mathrm{squ}\left(\frac{x - x_n}{\Delta x - w}\right) \right.
$$
$$
\left. +\mathrm{mod}[\phi_o, 2\pi]\mathrm{squ}\left(\frac{x - x_n + \Delta x/2}{w}\right)\right\}, \quad (2.17)
$$

where ϕ_o is the phase applied in the gap region. Note that in eq. 2.17 the phase values have been indicated modulo 2π, although 4π or 6π, etc., could be substituted depending on the properties of the actual device being used.

The next task will be to convert the spatial phase modulation function to a spectral phase modulation function in the case of nonlinear spectral dispersion. This can be written generically as

$$
M'(\Omega) \propto \int_{-\infty}^{\infty} \exp[i\phi(x)] \exp[-(x - x(\Omega))^2/\delta x^2]dx, \quad (2.18)
$$

Since $x(\Omega)$ represents the position of the frequency component Ω, eq. 2.18 performs a convolution of the phase applied by the mask as a function of position, $\phi(x)$, with a Gaussian function representing the spot size of the spectral component Ω. Unfortunately, due to the nonlinear dependence of $x(\Omega)$ on Ω, as well as the convolution

contained within $\phi(x)$, eq. 2.18 is not easily evaluated. Instead, $M'(\Omega)$ may be calculated with the aid of a computer. To do this, we first calculate $\phi(x)$ with about 10 grid points per pixel. Then $\phi(x)$ may be resampled on a grid of points evenly spaced in frequency, before evaluating eq. 2.18. Finally, the output pulse is calculated by fast Fourier transformation (FFT) of the product $E_{in}(\Omega)M'(\Omega)$. It is important to use the evenly-spaced frequency grid in order to make use of the computationally efficient (Cooley-Tukey) FFT algorithm.

2.4.2 Sampling Replica Pulses

The expression for a shaped output pulse with an idealized pulse shaping apparatus, (eq. 2.16), contains a summed term that is a complex Fourier series,

$$\sum_{n=-N/2}^{N/2-1} A_n B_n \exp[i(2\pi\nu_n t + \phi_n)]. \tag{2.19}$$

A property of Fourier series' (with evenly-spaced frequency samples) is that they repeat themselves with a period given by the reciprocal of the frequency increment. The present case is no exception, and the general waveform described by expression 2.19 is therefore repeated infinitely with a period of $1/\Delta\Omega$, although the Gaussian-sinc window (see eq. 2.16) suppresses repetitions that are at very long or very early times. Nonetheless, these pulse repetitions are a cause for concern since they can degrade the quality of a desired output waveform. Although these pulse repetitions have received some attention in the literature [67, 31, 56], it is typically without quantitative analysis, especially in the case of nonlinear spectral dispersion.

We refer to the undesired repetitions of the waveform mentioned above as *sampling replica* pulses since they are a direct consequence of the discrete sampling of the LC SLM. In a sense, the distinction between a "desired pulse" and a "sampling replica pulse" is an arbitrary one since both are part of a coherent optical waveform. Nonetheless, the distinction is useful in that it exposes the limitations inherent to pixelated modulators. One must also be careful when using the term "pulse." Although the input to a pulse shaper is usually expected to be a single pulse, the

desired output may consist of multiple pulses or some general output waveform. By "sampling replicas" we actually mean copies of the desired output waveform, whether the desired output waveform is simply a single delayed pulse, two oppositely chirped double-pulses, or a train of pulses, etc. It should be noted that nonpixelated devices, such as acousto-optic modulators (AOMs), allow for smoothly varying spectral phase and/or amplitude modulations free of sampling replica pulses (and modulator replica pulses, the subject of the next section) [26]. Despite these benefits, pulse shaping with AOMs is not widely used due to a lower efficiency and a significantly higher degree of complexity to operate especially for very short pulses. See reference [24] for a detailed comparison of pulse shaping with AOMs versus LC SLMs.

As described above, the phase applied by LC SLMs is of the form $\phi_{applied,n} = \mathrm{mod}[\phi_{desired,n}, 2\pi]$. Due to the mathematical equivalence of phase values that differ by integer multiples of 2π, there are an infinite number of ways to "unwrap" the applied phase. Sampling replica pulses constitute an important class of these equivalent phase functions, and their phase as a function of pixel is described by

$$\phi_{replica,n} = \phi_{applied,n} + 2\pi R n, \qquad (2.20)$$

where R is the sampling replica order and may be any nonzero integer ($R = 0$ corresponds to the desired pulse). Note that the analysis in this section will assume that the LC SLM has well defined pixels $[L(x) = \delta(x)]$ without gaps. In the case of linear spectral dispersion, $\phi_{replica,n}$ differ by the linear spectral phase $2\pi R\nu/\Delta\Omega$, which by virtue of the Fourier-shift theorem (see appendix 2.9) precisely corresponds to a temporal separation of $R/\Delta\Omega$. Therefore, many sampling replica pulses are produced, where each is temporally separated from the next by $1/\Delta\Omega$.

In the case of nonlinear spectral dispersion, the sampling replica pulses gain additional spectral phase. The nonlinear spectral dispersion is given below as a function of pixel number n in a power-series expansion:

$$\Omega_n = \overline{\Delta\Omega} + K n^2 + L n^3 + M n^4 + ... \qquad (2.21)$$

44

The variable $\overline{\Delta\Omega}$ is used here as the coefficient for the linear spectral dispersion to remind of its physical meaning (it is approximately the average frequency span per pixel), but should not be confused with the variable $\Delta\Omega$ that was used when the spectral dispersion was explicitly assumed to be linear. The phase difference $\Delta\phi_n$ between the replica pulse phase $\phi_{replica,n}$ and the applied phase $\phi_{applied,n}$ can now be expanded in a power series expression in terms of frequency,

$$
\begin{aligned}
\Delta\phi_n &= 2\pi R n \\
&= \alpha\Omega_n + \beta\Omega_n^2 + \gamma\Omega_n^3 + ...,
\end{aligned}
\tag{2.22}
$$

which can then be solved in powers of n by substitution of the expression for Ω_n given in eq. 2.21. Exact expressions for the first four coefficients of the spectral phase can thus be obtained:

$$
\begin{aligned}
\frac{\alpha}{2\pi R} &= \frac{1}{\overline{\Delta\Omega}} \\
\frac{\beta}{2\pi R} &= -\frac{K}{\overline{\Delta\Omega}^3} \\
\frac{\gamma}{2\pi R} &= -\frac{L}{\overline{\Delta\Omega}^4} + \frac{2K^2}{\overline{\Delta\Omega}^5} \\
\frac{\delta}{2\pi R} &= -\frac{M}{\overline{\Delta\Omega}^5} + \frac{5KL}{\overline{\Delta\Omega}^6} - \frac{5K^3}{\overline{\Delta\Omega}^7}.
\end{aligned}
\tag{2.23}
$$

The term α describes the expected linear delay of the sampling replica pulse of order R and is not dependent upon the nonlinear dispersion coefficients K, L, M, etc. The quadratic, cubic, and quartic spectral phases do, however, depend in varying degrees on the higher order spectral dispersion terms. All coefficients of the spectral phase are proportional to the replica order. Note that the above coefficients are completely general for a pixelated modulator, and apply regardless of whether phase and/or amplitude shaping of the pulse is used.

Figure 2-12 illustrates the principle of sampling replica pulses in the simple case
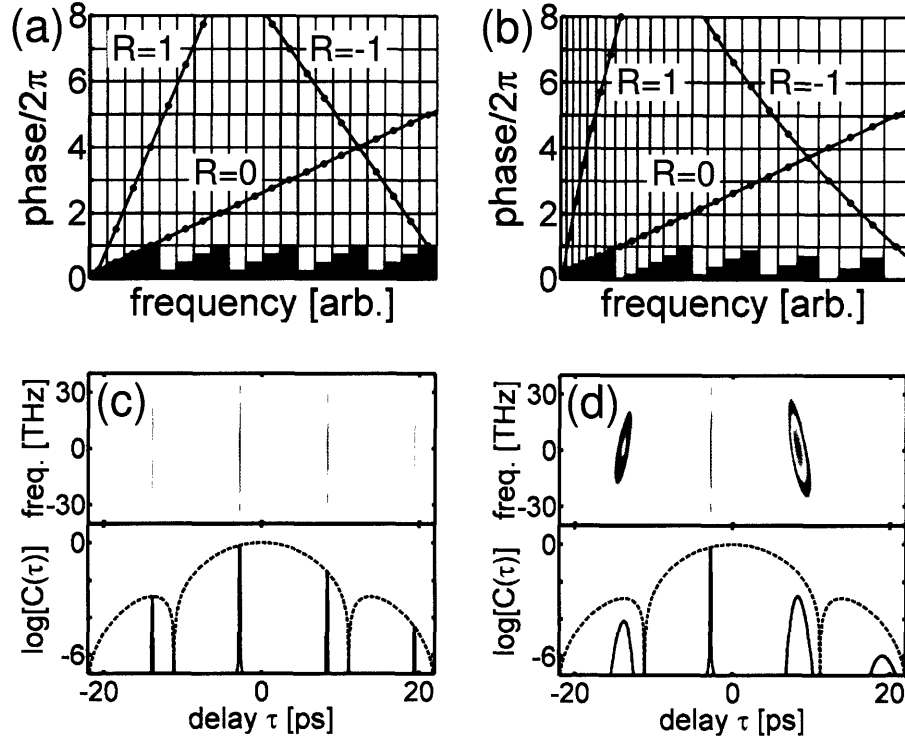
Figure 2-12: Illustration of sampling replica pulses. Applied phase (boxes), desired phase ($R = 0$), and sampling replica pulse phases ($R = \pm 1$) in the case of linear (a) and nonlinear (b) spectral dispersion. The black vertical lines represent pixel boundaries. Simulated XFROG and cross-correlation measurements (on a logarithmic scale) of the corresponding output waveforms for linear (c) and nonlinear (d) spectral dispersion. The extent of nonlinear spectral dispersion is exaggerated in (b) but not in (d).

when the desired spectral phase is linear with respect to frequency, with a slope of either $2\pi\Delta\Omega/4$ (for linear spectral dispersion) or $2\pi\overline{\Delta\Omega}/4$ (for nonlinear spectral dispersion). The desired phase, applied phase, and $R = \pm 1$ sampling replica phases, are shown in (a) for the case of linear spectral dispersion. A simulated XFROG measurement and cross-correlation measurement of the output waveform (both plotted on logarithmic scales) are shown in (c). The desired pulse occurs at about 2.6 ps. Three weaker replica pulses, each separated by about 11 ps, are also observed. Note in (c) that the relative intensities of the sampling replica pulses is determined by the Gaussian-sinc time window.

When the spectral dispersion is nonlinear, however, the spectral phase of the

sampling replica pulses is no longer linear as can be seen in fig. 2-12 (b). Although the magnitude of nonlinear spectral dispersion has been greatly exaggerated in (b) in order to make the nonlinear characteristics of the $R = \pm 1$ sampling replica pulse phases more apparent, the actual nonlinear spectral dispersion for our pulse shaping apparatus was used in the simulation in (d). There, simulated XFROG and cross-correlation measurements show that nonlinear spectral dispersion causes the replica pulses to become chirped. As expected from equations 2.23, the $R = \pm 1$ sampling replica pulses have opposite chirps and the weak $R = -2$ sampling replica pulse near $\tau = 18$ ps has a chirp twice that of the $R = -1$ sampling replica pulse near $\tau = 9$ ps. The slight nonuniform tilt (or curvature) of the $R = \pm 1$ replica pulses in the XFROG simulations is a result of non-negligible cubic and quartic spectral phase components.

The presence of higher order spectral phase (quadratic, cubic, etc.) on replica pulses in addition to the desired spectral phase typically has the effect of reducing their intensity by temporal spreading, as can be seen in the simulated cross-correlation plot in fig. 2-12 (d). One obvious exception is when the desired pulse itself is chirped, in which case one of the replica pulses may be partly (or even completely) compressed. In general, however, the combination of the Gaussian-sinc time window and the quadratic or higher-order spectral phase tends to suppress sampling replica pulses in a majority of situations to a tolerably low level.

Before moving on to a discussion of modulator replica pulses, in which the effects of pixel smoothing are discussed in detail, we will first examine the effects of LC SLM pixel gaps. Equation 2.17 described the general phase pattern resulting from an LC SLM with pixels separated by Δx and gaps of width w. If we assume linear spectral dispersion, phase-only modulation, and sharply-defined pixels, the spectral modulation applied by the LC SLM is given by

$$M(\Omega) = \mathrm{squ}\left[\frac{\Omega}{N\Delta\Omega}\right]\left\{\mathrm{comb}\left[\frac{\Omega}{\Delta\Omega}\right] \otimes \mathrm{squ}\left[\frac{\Omega - \Delta\Omega/2}{w\Delta\Omega/\Delta x}\right]\exp[i\phi_o] + \right.$$
$$\left.\left(\exp[i\phi_{applied}(\Omega)]\mathrm{comb}\left[\frac{\Omega}{\Delta\Omega}\right]\right) \otimes \mathrm{squ}\left[\frac{\Omega}{\Delta\Omega(1 - w/\Delta x)}\right]\right\}. \quad (2.24)$$

The first term within the curly brackets describes the spectral phase applied by the gap regions of the LC SLM, while the second term describes the spectral phase applied by the pixel regions of the LC SLM. The function $\mathrm{comb}(\Omega)$ is defined as

$$\mathrm{comb}(\Omega) = \sum_{n=-\infty}^{n=\infty} \delta(\Omega - n), \qquad (2.25)$$

requiring the use of the aperture function $\mathrm{squ}(\Omega/N\Delta\Omega)$ such that $M(\Omega)$ is defined to be zero outside the range of the LC SLM. The mask's temporal response may then be computed by Fourier transformation to be

$$m(t) \propto \mathrm{sinc}[\pi N \Delta\Omega t] \otimes \left\{ \mathrm{comb}[\Delta\Omega t] \frac{w\Delta\Omega}{\Delta x} \mathrm{sinc}\left[\pi \frac{w\Delta\Omega}{\Delta x} t\right] \exp[i\phi_o] + \right.$$
$$\left. \mathrm{comb}[\Delta\Omega t] \Delta\Omega (1 - \frac{w}{\Delta x}) \mathrm{sinc}\left[\pi\Delta\Omega(1 - w/\Delta x)t\right] \otimes \left(\sum_{n=-N/2}^{N/2-1} \exp[i(2\pi\nu_n t + \phi_n)] \right) \right\}.$$

$$(2.26)$$

The first term here describes the temporal response due to gap regions within the LC SLM and the second term describes the temporal response due to the pixel regions within the LC SLM.

Equation 2.26 illustrates two effects resulting from the presence of the gap regions. First, the gaps create "gap" replica pulses centered about time $t = 0$ with a period of $1/\Delta x$. The amplitude of the gap replica pulses is governed by a sinc envelope with a temporal width determined by the reciprocal of the spectral width of the gap. As the gap width w goes to zero, the gap replica pulses decrease in intensity. In the case of nonlinear spectral dispersion, the modulator replica pulses due to the gaps (except the one at time $t = 0$) become chirped as they gain additional spectral phase according to the arguments laid out above. The summation in the second term represents the desired phase-modulated output pulse, where the convolution of the desired output pulse with the function $\mathrm{comb}[\Delta\Omega t]$ creates sampling replica pulses separated by $1/\Delta\Omega$ as described above. As the pixel gap width increases from zero, the width of the term

48

sinc$[\pi\Delta\Omega(1 - w/\Delta x)t]$ grows, with the result that the sampling replica pulses are somewhat less suppressed than otherwise. In the case when no phase modulation is applied, the gap replica pulses in the first term and the sampling replica pulses in the second term cancel out such that the output pulse is a single unshaped pulse as expected. In practice, however, it turns out that pixel-smoothing effects tend to dominate the gap regions that would be expected for LC SLMs, as will be shown in the next section.

2.4.3   Modulator Replica Pulses

As opposed to the sampling replica pulses discussed in the previous section, there is an entirely different class of output waveform distortions that result from effects such as pixel gaps and smoothed-out pixel regions [finite spatial response $L(x)$] in combination with abrupt jumps or phase wraps. Somewhat loosely, we refer to these these distortions as *modulator replica* pulses since discrete (and usually unwanted) pulses are often produced [41]. In this section we will focus on the case in which the objective is to delay a pulse in time. The implications for other types of shaped pulses will also be addressed.
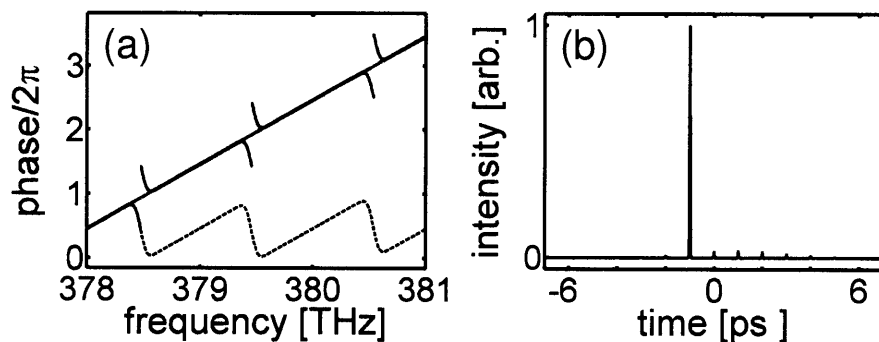
Figure 2-13: (a) Spectral phases with slope 2πps: desired phase (gray); applied phase (dashed); unwrapped applied phase (solid). (b) Corresponding simulated output pulse shape with weak modulator replica pulses separated by 1 ps.

Delaying a pulse in time, although it is a relatively simple "pulse shape," is an especially important capability for applications of two-dimensional femtosecond pulse shaping, such as phase-stable degenerate four-wave mixing spectroscopy [68]. Addi-

tionally, the output waveforms are sufficiently simple that they readily illustrate the origins of the distortions. As mentioned above, all that is required to delay a pulse by τ is to apply a spectral phase with the slope $-2\pi\tau\nu$. Since LC SLMs typically have the ability to apply a maximum spectral phase of only slightly in excess of 2π, the phase is applied modulo 2π. The presence of these phase-wraps in combination with a finite spatial response $L(x)$ creates periodic distortions in the applied phase. An example of these periodic distortions in the applied phase is shown in fig. 2-13(a). In this case, the desired spectral phase is a line (gray line) with a slope that corresponds to a delay of -1 ps, where only a small portion of the applied phase has been shown. The applied spectral phase (dashed curve) appears as a smoothed-out sawtooth function, due to the convolution with the finite spatial response $L(x)$ which is in this case sufficiently broad that it blurs out the distinctions between separate pixels. The periodic deviations in the applied phase become clear when it is "unwrapped" (black curve). Figure 2-13(b) shows a simulation of the output pulse intensity resulting from the phase pattern of fig. 2-13(a). Note that the spacing of the modulator replica pulses is inversely proportional to the spacing of the phase wraps. If the LC SLM could apply phase shifts modulo 4π, then the modulator replica pulses would be separated by only 0.5 ps. Furthermore, the lower number of phase wrap points would also reduce the intensity of the modulator replica pulses. In the limit of no phase wrap points, the modulator replica pulses disappear.

As the desired spectral phase becomes steeper and steeper, more and more phase wrap points are introduced, causing the modulator replica pulses to grow in intensity relative to the desired pulse [fig. 2-14]. Due to this, the peak intensity of the delayed pulse is lower than that predicted by the Gaussian-sinc time window of the pulse shaping apparatus (eq. 2.16). Figure 2-14 (c) plots measured (dots) and simulated peak intensities (black curve) as a function of delay. For reference, the dashed line shows the Gaussian-sinc time window. Note that the results of simulations that account for modulator replica effects are in good agreement with experimental measurements of variably delayed pulses, although there is a noticeable asymmetry in the measured peak intensities at positive times compared to negative times. This asymmetry is
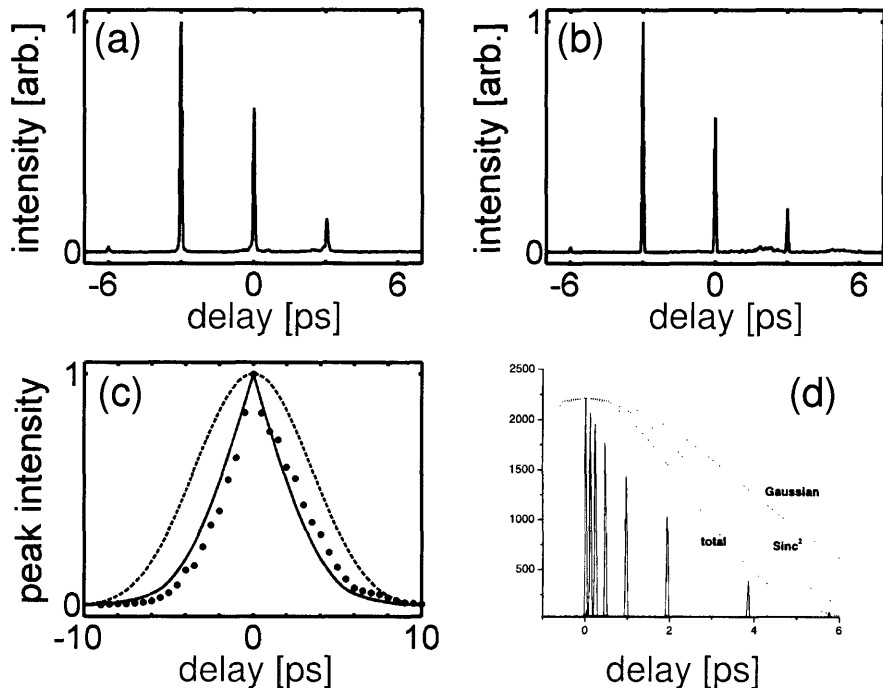
Figure 2-14: (a) Experimental cross-correlation measurement of a pulse shifted to negative 3 ps with modulator replica pulses and (b) a simulation of the cross-correlation measurement. (c) Delayed pulse peak intensity (dots) with the simulated time window including the effects of modulator replica pulses (solid) compared to Gaussian-sinc time window for the pulse shaping apparatus used in this thesis. (d) Similar results observed by Wang et al. in [56], with a 512-element LC SLM, compared to the Gaussian, sinc, and Gaussian-sinc time window of their apparatus.

due to space-time coupling effects [69] which have not been implemented in the simulations. Wang et al. [56] observed a similar delay-dependent intensity dependence for variably-delayed pulses performed with a different LC SLM, [2-14 (d), figure by permission of Prof. A.M. Weiner of Purdue University] although they did not identify the origin of the unexpectedly fast rolloff as a function of delay.

Modulator replica pulses can also be strongly influenced by nonlinear spectral dispersion. As mentioned above, it is the periodicity of the phase wraps that determines the temporal separation of modulator replica pulses. In the case of linear dispersion, then, it follows that the phase wraps will only be evenly spaced when the slope of the spectral phase is $2\pi/A\Delta\Omega$, where A may be any nonzero integer. For instance, a linear spectral phase with slope of $2\pi/4\Delta\Omega$ produces a phase wrap every 4 pixels

51

with replica pulses separated by $1/4\Delta\Omega$. Correspondingly, a linear spectral phase with a slope of $2\pi/4.5\Delta\Omega$ produces phase wraps in alternating 4- and 5-pixel groups that repeats every 9 pixels. The resulting replica pulses therefore have a periodicity of $1/9\Delta\Omega$.

Nonlinear spectral dispersion in general destroys the periodicity of the phase wraps as they tend to be closer together on one side of the spectrum and further apart on the other side of the spectrum. In this case, modulator replica pulses occur with a temporal separation corresponding to the average phase wrap period $2\pi/\tau$, where the slope of the desired phase is $2\pi\tau$, and where other possible modulator replica pulses are chirped to a much lower intensity. The above effects are illustrated in the simulations shown in fig. 2-15, where the slope of the desired spectral phase is $2\pi/4.5\Delta\Omega$ in the case of linear spectral dispersion (a) and $2\pi/4.5\overline{\Delta\Omega}$ ps in the case of nonlinear spectral dispersion (b). In (b), only 4 modulator replica pulses are observed, while in (a), additional modulator replica at intermediate times are observed. The modulator at intermediate times in (a) have become chirped to a nearly negligible intensity in (b), although careful examination of the baseline in (b) near 1.5 ps and 4 ps reveals two "noisy" regions corresponding to the chirped modulator replica pulses.

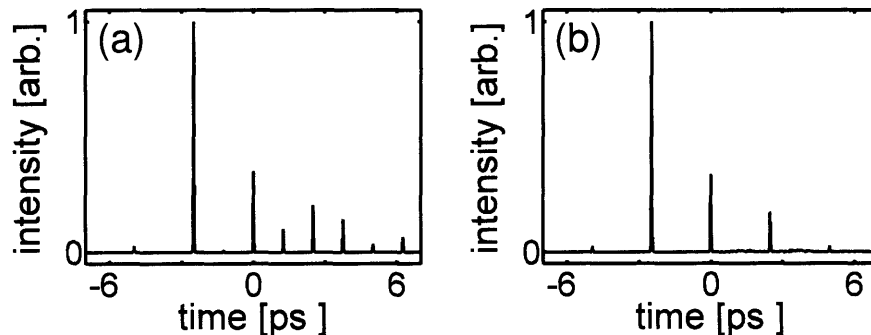Figure 2-15: Simulations illustrating the dependence of modulator replica on the periodicity of pixel wraps in the cases of linear spectral dispersion (a) and nonlinear dispersion (b).

So far, we have focused on the simple case of delayed pulses, which are accompanied by modulator replica pulses for LC SLMs that have smooth pixels. Not all phase patterns of interest require the use of phase wraps in adjacent pixels. For

example, a sinusoidal phase pattern with a peak-peak amplitude of less than 2π is used in many coherent control experiments to produce a series of output pulses with an even spacing (for instance, [8, 15]). Since no phase wraps are required for these waveforms, there are no distortions introduced due to smooth pixel boundaries. In fact, the smooth pixels now have the desirable effect of *reducing* the amplitude of sampling replica pulses, as can be seen in fig. 2-16.
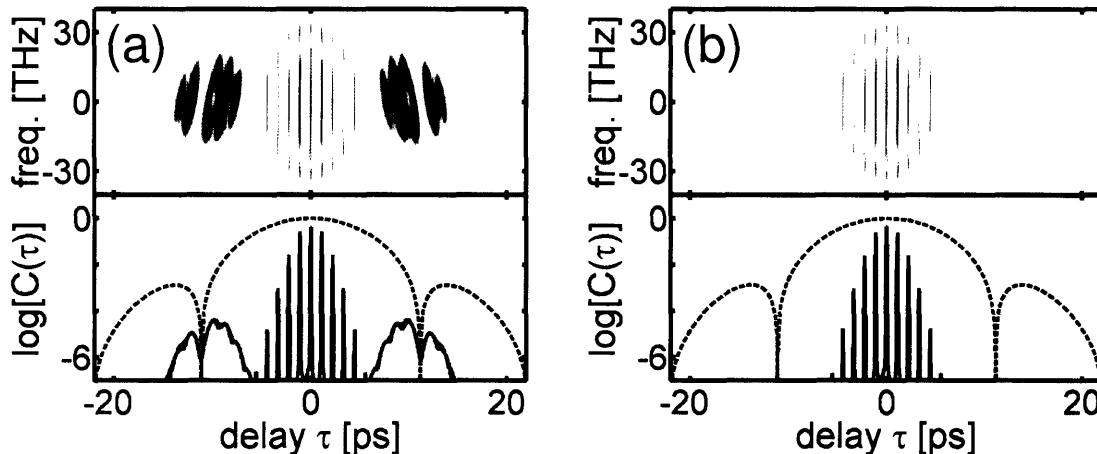
Figure 2-16: Simulated XFROG and cross-correlation measurements (on a logarithmic scale) of waveforms generated by application of a sinusoidal spectral phase that does not exceed 2π with (a) a LC SLM that has sharp pixels and (b) the present device that has smooth pixels.

To summarize the replica pulse effects discussed above, fig. 2-17 shows experimental XFROG measurements (courtesy of the group of Prof. Roland Sauerbrey at the Friedrich-Schiller University in Jena, Germany) and simulated XFROG measurements that take into account nonlinear spectral dispersion and pixel smoothing for the Jenoptik 640-pixel phase-only LC SLM. Each successive row of the measurements and simulations displays an XFROG measurement of the waveform resulting from the application of a linear spectral phase with a slope necessary to delay the pulse to positive times, from 0 to 14 ps in increments of 2 ps. The average frequency span per pixel is such that the sampling replica period is 14 ps, as can be seen at negative times for the chirped sampling replica pulse that always leads the desired pulse by 14 ps. Multiple modulator replica pulses occur at integer multiples of the desired delay, most notably for the 2 and 4 ps delayed pulses. Weak chirped modulator replica

53
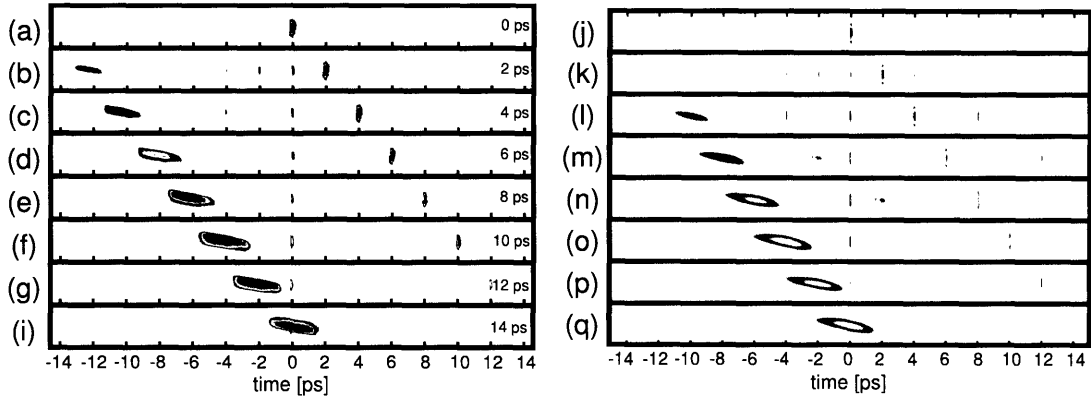
Figure 2-17: Experimental (a)-(i) and corresponding simulated (j)-(q) XFROG measurements of waveforms resulting from the application of a linear spectral phase, illustrating both sampling and modulator replica pulses. The y-axis of the plots is wavelength, increasing upwards, and the colormap is logarithmic. The measurements (courtesy of the group of Prof. Roland Sauerbrey of FSU in Jena, Germany) are rescaled individually so the maximum intensity in each is the same color, while each of the simulations uses the same scale and colormap such that the maximum intensity decreases with increasing delay. The "desired" waveform in each case is a single pulse with a temporal delay between 0 and 14 ps.

are observed at times not corresponding to integer multiples of the desired delay in the simulations, for instance -2 ps in (m) or +2 ps in (n). These chirped modulator replica pulses are due to the choice of delaying the pulses in time increments of $1/7\overline{\Delta\Omega}$, which created larger repeat units in the wrapped phase such as was described for the pulses shown in fig. 2-15. Careful study of the experimental measurements (magnified 10x on a computer screen) revealed that these chirped modulator replica were also present in the experiments at the same times and with approximately the same chirp, although the colormap makes these features difficult to observe.

2.5   Real-Space Shaping

The simplest two-dimensional pulse shaping scheme is real-space shaping, in which each row (or more typically, each group of rows) of the LC SLM is used to shape different horizontal slices of the laser pulse, producing many independent outputs [38, 39]. No additional analysis is required to describe real-space shaping as it is equivalent

54

to having many temporal-only pulse shapers, each at a different height within the beam of a laser pulse. In real-space shaping, a lens is used to image the LC SLM to the plane of the sample in order to avoid diffraction effects that would otherwise blur the shaped outputs. Specifically, a horizontally-aligned 30 cm cylindrical lens was used to image the face of the SLM onto a BBO crystal with approximately 1:1 imaging (see fig. 2-18). The shaped pulse was measured by spatially resolved cross correlation with an expanded unshaped reference pulse that was variably delayed along a motorized delay line. The second harmonic radiation created by each incident beam alone was blocked, and the intensity of the cross-correlation signal was recorded by imaging (1:1) the BBO crystal onto a CCD camera for various delays of the reference pulse. A blue colored-glass filter was used to eliminate scattered 785 nm light originating from the incoming pulses. Note that this arrangement allows for a simultaneous cross-correlation measurement of all of the shaped outputs which are separated in the vertical direction.
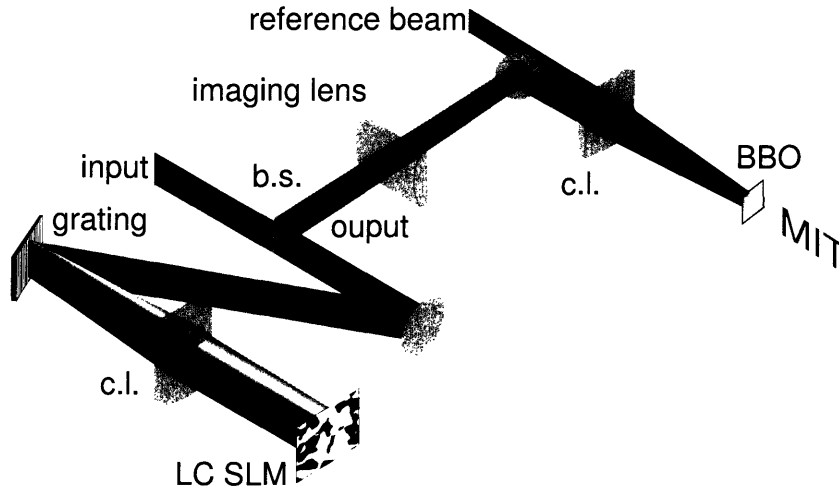
Figure 2-18: Setup for real-space shaping. The cylindrical lens imaged the face of the LC SLM onto the BBO crystal. An unshaped reference pulse was used for spatially resolved cross-correlation with the shaped pulses.

Cross-correlation signals for an unshaped pulse and two shaped outputs are shown in fig. 2-19. The cross-correlation intensity is plotted as a function of the delay time and the vertical spatial dimension. As expected, the unshaped pulse is located along

a straight vertical line around zero delay. The vertical intensity distribution reflects the Gaussian spatial intensity distribution of the incident laser beam. For a first demonstration of real-space shaping, a linear spectral phase modulation was applied to the different vertical regions of the SLM. The slope of the linear spectral phase was varied from one region to the next by constant increments. The shaped output consists of approximately 40 independently specified regions, each region being 3 pixels high. In figures 2-19 (b) and (c) the delay varies by ±0.022 ps/pixel along the positive spatial dimension. The slope of the expected position/delay ratio in the shaped pulses as indicated by the straight line is in good agreement with the experimental results. The tilt of the individual regions apparent in fig. 2-19 (c) was due to a slight misalignment in the cylindrical lens of the grating/lens pair.
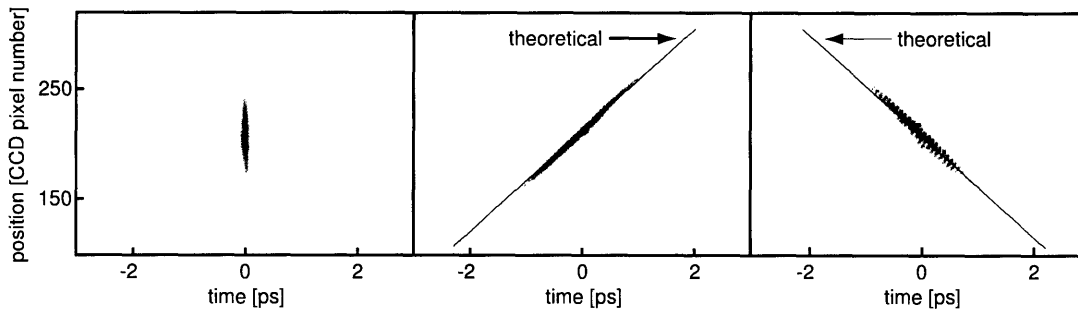
Figure 2-19: Spatially resolved cross-correlation data. (a) Unshaped pulse. (b) Positive and (c) negative delay sweeps in increments of ±0.022 ps/pixel. The straight lines in (b) and (c) indicate the expected time delay.

The high spatial resolution obtainable via real-space shaping is shown in fig. 2-20. Here, about 18 spatial regions of the LC SLM were used to create linear (a) and parabolic (b) delay sweeps. Each region on the LC SLM was 3 pixels high, and the temporal delay between successive regions was large enough that each region was clearly visible. Since this LC SLM consists of 480 pixels, up to 160 independent regions may be generated. Subsequent experiments have suggested that the factor limiting the spatial resolution of a given region to about two or three rows of the LC SLM is in fact the slightly blurry imaging used to address the LC SLM (see section 2.2.2). The absolute size of the actual output waveform may be easily manipulated with imaging optics subsequent to the LC SLM designed to magnify or demagnify

the spatial profile of the beam to a desired size at the sample plane.
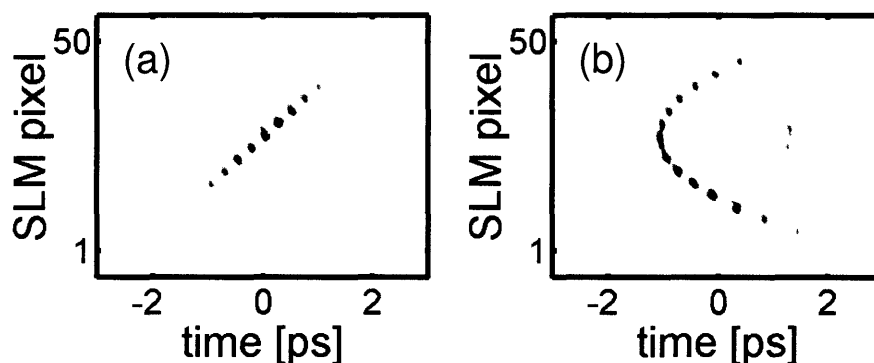
Figure 2-20: Linear (a) and parabolic (b) delay sweeps for LC SLM regions that are only 3 pixels high. Weak modulator replica pulses are evident in both waveforms.

Two examples of sophisticated two-dimensional waveforms generated through real-space shaping are illustrated in fig. 2-21. The pulse shapes are about 4 mm high and 1.5 ps in duration. An adaptation of the Gerchberg-Saxton algorithm was used to calculate the phase mask patterns necessary to generate the user-defined two-dimensional pulse shapes presented in fig. 2-21 (a) and (b) [70, 57]. The benefit of this algorithm is especially significant for two-dimensional phase-only pulse shaping because the iterative Fourier transform technique calculates a complicated SLM pattern consisting of many independently shaped outputs in just a few seconds while standard simulated annealing or genetic algorithms would take many hours to perform the same task. See section 2.7 for a description of the algorithm.
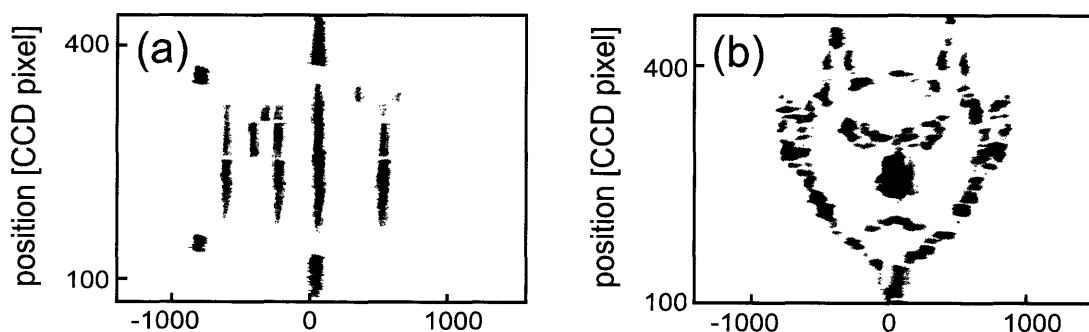
Figure 2-21: (a) Complex user-defined two-dimensionally-shaped laser pulse. (b) Unexpected manifestation of Satan in output waveform during laser malfunction.

2.6 Beam Shaping

Just as a LC SLM can modulate spectral phases and/or amplitudes to produce a desired temporal waveform, it can also be used to manipulate the spatial profile of a beam (Fourier beam-shaping). Before describing a method called wavevector shaping that is a hybrid of Fourier beam-shaping and temporal pulse shaping in section 2.7, we will present a brief analysis of Fourier beam-shaping.

Methods for beam shaping are well known (for example, [71, 72, 73, 74, 75]) and simple beam shaping devices, such as attachments for laser pointers and certain types of holograms, are commonly encountered outside of the lab. A generic schematic illustration for beam shaping is shown in fig. 2-22, where a single input beam $E_{in}(x, y)$ is redistributed to become two output spots at the plane $e_{out}(x, y)$. This redistribution is accomplished by modulating the phase of the input beam E_{in} at the mask plane $M(x, y)$ prior to Fourier transformation by a lens L. The phase modulation element M is positioned one focal length before the lens and the output beam E_{out} is generated at the plane one focal length after the lens (dotted line).
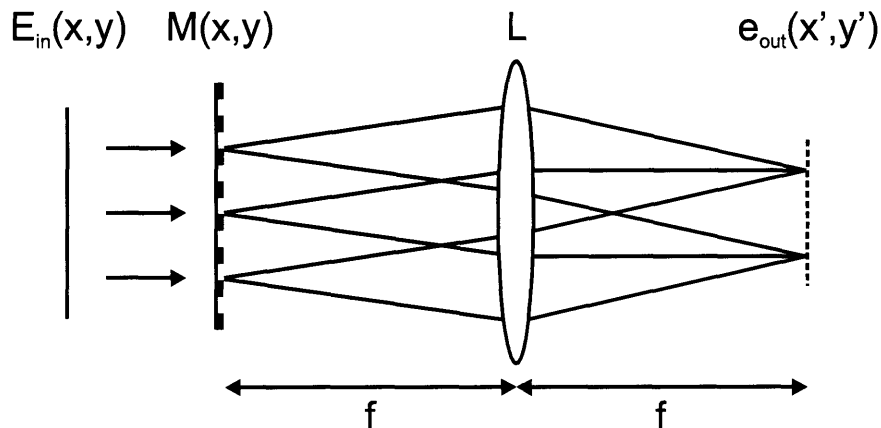
Figure 2-22: Schematic illustration of Fourier beam shaping. The input beam E_{in} is modulated by the phase pattern M before Fourier-transformation by a lens with focal length f, producing the output beam E_{out} at the plane given by the dotted line.

The analysis of beam shaping is quite similar to the analysis for 1D pulse shaping in section 2.4.1 with the exception that the input field is assumed to be monochromatic. The output beam $E_{out}(x, y)$ directly after the LC SLM $M(x, y)$ is given by

58

$$E_{out}(x, y) = M(x, y)E_{in}(x, y), \tag{2.27}$$

where $E_{in}(x, y)$ is the input beam prior to the modulator. Assuming a phase-only LC SLM with no gaps and square pixels of size $\Delta x \times \Delta y$, the phase modulation applied by the LC SLM is given by

$$M(x, y) = \exp\left[i\phi(x, y)\right], \tag{2.28}$$

where the applied phase $\phi(x, y)$ is

$$\phi(x, y) = L(x, y) \otimes \sum_{l=-N/2}^{N/2-1} \sum_{m=-N/2}^{N/2-1} \text{mod}[\phi_{l,m}, 2\pi] \text{squ}\left(\frac{x - x_l}{\Delta x}\right) \text{squ}\left(\frac{y - y_m}{\Delta y}\right). \tag{2.29}$$

Here x_l represents the positions of the columns of the LC SLM and y_m represents the positions of the rows of the LC SLM. As before, in order to produce an intuitive (albeit approximate) analytical result, we will assume that the pixels are very sharply defined $[L(x, y) = \delta(x)\delta(y)]$. $M(x, y)$ can then be simplified to yield

$$M(x, y) = \sum_{l=-N/2}^{N/2-1} \sum_{m=-N/2}^{N/2-1} \exp[i\phi_{l,m}] \text{squ}\left(\frac{x - x_l}{\Delta x}\right) \text{squ}\left(\frac{y - y_m}{\Delta y}\right). \tag{2.30}$$

Assuming that the input pulse with spatial amplitude $B_{x,y}$ is a diffraction-limited beam (i.e. that its phase is flat, such as for a plane wave), the output beam can now be easily calculated

$$e_{out}(\nu_x, \nu_y) \propto \text{sinc}(\pi\Delta x\nu_x)\text{sinc}(\pi\Delta y\nu_y) \times$$
$$\sum_{l=-N/2}^{N/2-1} \sum_{m=-N/2}^{N/2-1} B_{l,m} \exp[-i(2\pi\nu_x x_l + 2\pi\nu_y y_m - \phi_{l,m})]. \tag{2.31}$$

59

As described in section 2.9, wavevectors ν_x and ν_y are linearly proportional to position in the spatial Fourier plane (x', y'), according to the relations $\nu_x = x'/f\lambda$ and $\nu_y = y'/f\lambda$.

Analogous to the time window discussed in section 2.4, there is an equivalent *position window* in Fourier beam shaping, given by $\text{sinc}(\pi w \nu_x)\text{sinc}(\pi w \nu_y)$. This position window places approximate limits on the size of the region in the spatial Fourier plane for shaping the output beam $e_{out}(x', y')$. Unlike temporal-only pulse shaping, there is no Gaussian term in the position window. In Fourier beam shaping, phase modulations may be directly imparted to different regions of the input beam, whereas in pulse shaping, the phase modulations are applied to a convolved spectral and spatial profile (see eq. 2.16). Since both temporal-shaping and Fourier beam-shaping share a Fourier-transform relationship between their outputs and the phase and/or amplitude modulations applied to the inputs, similar modulation functions produce analogous results in each. A linear spatial phase (i.e. a prism) shifts a beam in space just as a linear spectral phase shifts a pulse in time. A quadratic spatial phase (i.e. a lens) spreads out a beam in space just as a quadratic spectral phase can chirp a pulse in time. A periodic spatial phase (i.e. a diffraction grating) creates multiple output spots just as a sinusoidal spectral phase creates multiple output pulses, and so forth. These dualities will be exploited in the next section where beam shaping methods and pulse shaping methods are combined.

Two simple examples of Fourier beam-shaping are shown in fig. 2-23. Beam (a) was produced with a radially symmetric phase pattern, where an axial cross-section through the phase pattern resembled the shape of the letter w. Beam (b) was produced with a phase pattern consisting of many horizontal regions, where a linear spatial phase was applied along the length of each region, with increasing slopes in consecutive regions.

60
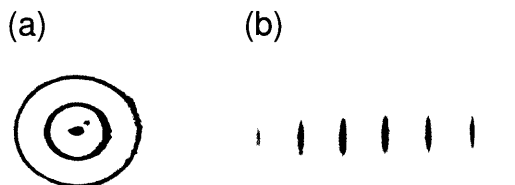
Figure 2-23: Output beams generated through Fourier beam-shaping. In (a), the weak rings toward the upper right corner of the image due to stray reflections within the imaging apparatus.

2.7 Wavevector Shaping

In a sense, the real-space pulse shaping method described in section 2.5 possesses an asymmetry between pulse shape and beam shape. That is, real-space shaping allows the pulse to be shifted in time or divided into several pulses, but it does not allow the time-integrated energy of the beam to be similarly redistributed in space. By combining temporal pulse shaping with Fourier beam-shaping, a scheme we refer to as wavevector shaping, several new and interesting properties emerge [40, 41], as described in the remainder of this chapter.

2.7.1 Wavevector Shaping, General Analysis

The experimental apparatus for wavevector shaping is nearly identical to that of real-space shaping, with the only difference being that the lens used in real-space shaping to image the LC SLM regions to the sample plane is replaced with a lens of twice the focal length so that the sample resides at the focal plane of the shaped pulse (fig. 2-24). By this means, the vertical spatial profile and the temporal profile are related to the modulated input field by Fourier (and inverse Fourier) transformation:

$$e_{out}(\nu_y, t) = \int_{-\infty}^{\infty} \int_{-\infty}^{\infty} M(y, \nu) E_{in}(y, \nu) \exp\left[i2\pi(\nu t - \nu_y y)\right] d\nu \, dy. \tag{2.32}$$

For a phase-only LC SLM without gaps, the modulation applied by the LC SLM is given by
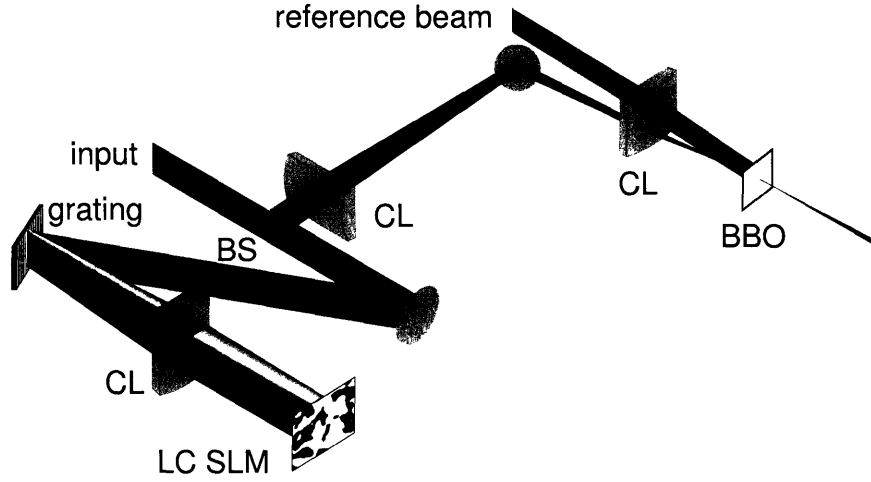
Figure 2-24: Setup for wavevector shaping. The cylindrical lens spatially Fourier transforms the output field onto the plane of the BBO crystal. An unshaped reference pulse is used for spatially-resolved cross-correlation with the shaped pulses.

$$M(x, y) = S(x) \otimes \exp\left[i\phi(x, y)\right],$$ (2.33)

where the spatial profile $S(x)$ of the input beam is assumed to have a constant width for all values of y. The applied phase $\phi(x, y)$ is given by

$$\phi(x, y) = L(x, y) \otimes \sum_{m=-N/2}^{N/2-1} \sum_{n=-N/2}^{N/2-1} \mathrm{mod}[\phi_{m,n}, 2\pi] \mathrm{squ}\left(\frac{x - x_n}{\Delta x}\right) \mathrm{squ}\left(\frac{y - y_m}{\Delta y}\right),$$ (2.34)

where y_m is the position of the mth row of the SLM and x_n is the position of the nth column of the SLM. As was the case for 1D pulse shaping, eqs.2.32-2.33 are not easy to evaluate analytically, especially due to the nonlinear spectral dispersion. If we assume for the purpose of obtaining a simple (but approximate) analytical result, that the spectral dispersion is linear ($\Omega_n = \Delta\Omega n$) and that the pixels are sharply defined [$L(x, y) = \delta(x)\delta(y)$], then the modulation applied by the LC SLM is given by

$$M(y, \Omega) = S(\Omega) \otimes \sum_{m=-N/2}^{N/2-1} \sum_{n=-N/2}^{N/2-1} \exp[i\phi_{m,n}] \mathrm{squ}\left(\frac{\Omega - \Omega_n}{\Delta\Omega}\right) \mathrm{squ}\left(\frac{y - y_m}{\Delta y}\right). \quad (2.35)$$

As in section 2.4.1, $S(\Omega) = \exp(-\Omega^2/\delta\Omega)$, where $\delta\Omega$ represents the spectral resolution of the grating-lens pair. This time, the generic input spatial and spectral intensity profile is approximated by

$$E_{in}(y, \Omega) = \sum_{m=-N/2}^{N/2-1} \sum_{n=-N/2}^{N/2-1} \mathrm{squ}\left(\frac{\Omega - \Omega_n}{\Delta\Omega}\right) B_{m,n} \mathrm{squ}\left(\frac{y - y_m}{\Delta y}\right) B_{m,n}, \quad (2.36)$$

where the indices m and n represent the spatial and the spectral coordinates, respectively. Substitution of equations 2.36 and 2.35 into equation 2.32 yields the following expression for the output,

$$e_{out}(\nu_y, t) \propto \exp\left[-\pi^2 \delta\Omega^2 t^2\right] \mathrm{sinc}(\pi\Delta\Omega t)\mathrm{sinc}(\pi\Delta y \nu_y)$$
$$\sum_{m=-N/2}^{N/2-1} \sum_{n=-N/2}^{N/2-1} B_{m,n} \exp\left[i(-2\pi\nu_y y_m + 2\pi\Omega_n t + \phi_{m,n})\right]. \quad (2.37)$$

Somewhat intuitively, the output waveform contains a time-position window which is governed along the temporal dimension by a Gaussian-sinc time widow (as in 1D temporal shaping) and which is governed along the spatial dimension by a sinc position window (as in Fourier beam shaping).

2.7.2 Wavevector Shaping, Simple Demonstrations

Wavevector shaping is capable of producing a wide variety of output waveforms with specified spatial, temporal, and spectral properties. Figure 2-25 illustrates the simplest subset of these waveforms with a series of nine experiments. The unmodulated pulse, originally centered in space and time, has been steered to different positions

located on a circle in space-time. Application of a linear spectral phase gradient shifts the pulse in time, while application of a (vertical) spatial phase gradient shifts the beam upwards. A phase gradient along an intermediate direction shifts both the beam and the spot.
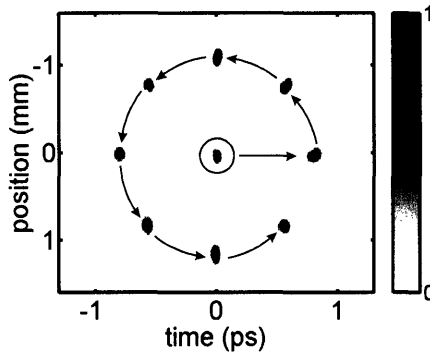
Figure 2-25: A single pulse, originally centered in space and time, has been steered around to different positions all located on a circle in space-time.

A more complicated waveform is shown in Figure 2-26, where a ring-shaped waveform (a) was produced by the application of a conical phase pattern by the LC SLM (b). The applied phase pattern has the appearance of concentric rings since the desired conical phase pattern has been applied modulo 2π. Although the output waveform was the expected shape, two features of (a) warrant discussion. First, there is a bright spot in the center of the waveform. The bright spot is a modulator replica pulse (or equivalently, the zeroth order diffraction spot) and is a feature observed in most wavevector-shaped pulses generated with the present LC SLM. Additionally, the ring has a slight fuzziness to it, especially at positive times due to neglecting to incorporate the nonlinear spectral dispersion when calculating the desired phase pattern.

Although cross-correlation measurements are often adequate to describe shaped waveforms, in the case of the ring-shaped waveform shown in fig. 2-26, there is a great deal of information about the pulse that is not revealed. By recording the spectral intensity of the cross-correlation signal for all positions as a function of time, a technique which we have dubbed spatially-resolved FROG (SR-FROG), additional details about the shaped waveform are obtained. The setup for SR-FROG differs from

64
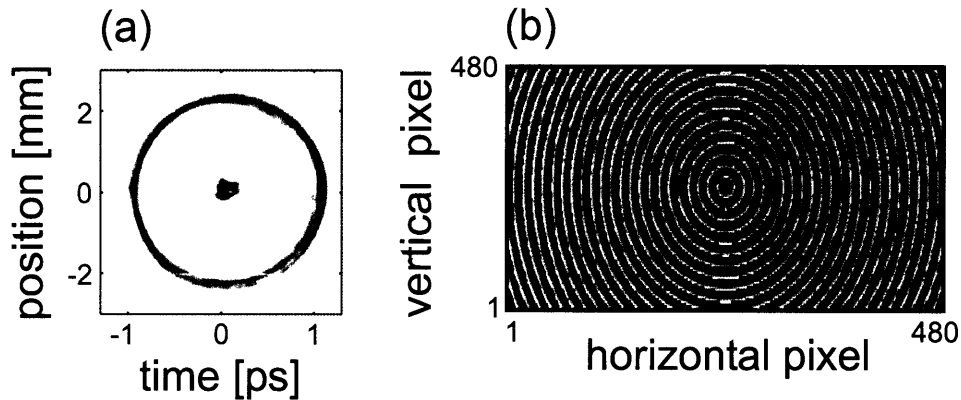
Figure 2-26: A waveform in the shape of a ring (a) was generated by a phase pattern in the form of a cone (b). The spot at time and position zero in (a) is a modulator replica pulse.

the spatially-resolved cross-correlation apparatus (fig. 2-9) only in that an imaging spectrometer has been used instead of a CCD, in order to produce a spectrally and spatially resolved cross-correlation measurement. An isosurface of an SR-FROG trace of a shaped waveform resulting from application of a phase cone is shown in fig. 2-27 (a). The faces display the FROG intensity projected along the corresponding perpendicular axes. For example, integrating the intensity along the frequency axis recovers the spatially resolved cross-correlation. It is easy to understand how the waveform is generated considering two limiting cases. First, a cross section through the phase cone along the frequency axis shows that one half of the spectrum is shifted toward negative and the other half toward positive times. Since the derivative of the phase with respect to the spatial coordinate is zero, the beam is shifted neither up nor down. On the other hand, a vertical cross section shows that the whole spectrum in the upper half is spatially shifted upward and the opposite is true for the lower half. In this case, the derivative with respect to the frequency axis is zero and no shift along the time axis occurs. The whole cone rearranges the laser pulse intensity such that it appears as a circle in a space-time plot. A simple simulation of the SR-FROG measurement that assumes linear spectral dispersion and sharp pixel boundaries is shown in fig. 2-27 (b).

The Fourier-transform relationship between real-space shaping and wavevector

65
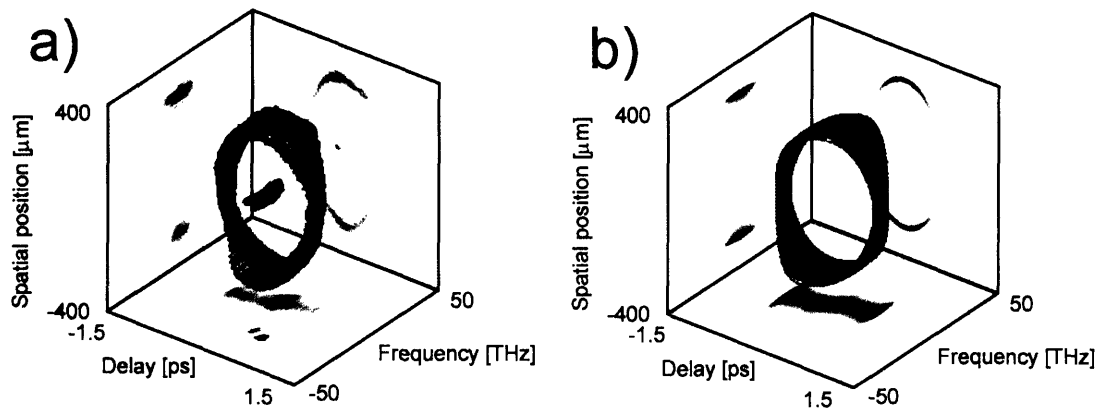
Figure 2-27: (a) Measured and (b) calculated SR-FROG trace. In both cases an isosurface corresponding to half the maximum value is shown. The three faces show the projections along the corresponding axis.

shaping is illustrated in fig. 2-28. Here, the waveforms resulting from an applied phase pattern were recorded for both real-space shaping (b) and wavevector shaping (c), with the only difference in the experimental apparatus being the choice of lens CL to determine whether real-space shaping mode or wavevector shaping mode was used. The real-space shaping output may be conceived as the waveform generated at the plane of the LC SLM [fig. 2-28(a), left]. In this case, the phase pattern used to generate the flying-V real-space shaping waveform consisted of about 30 horizontal regions of the LC SLM, where linear spectral phases of different slopes were applied within each region such that the temporal intensity was distributed along the shape of the letter V. The cylindrical lens CL transformed the flying-V waveform into one consisting of a series of fringe patterns with progressively smaller fringe spacings (c). The fringe spacing is determined by the angle at which the pulse pairs in (b) cross at any given time. Therefore, the smaller fringe patterns in (c) correspond to the

66

larger spatial separation between pulse pairs in (b) at long times, and vice versa. As before, the bright spot in (c) at time zero corresponds to the zeroth order diffraction spot. Note that the same distance scale is used on the y-axes of (b) and (c), indicating correctly that the overall size of the fringe patterns in (c) is *larger* than than the flying-V waveform in (b). Although this may seem counterintuitive, it is a the consequence of a small input beam size and a long focal length lens. For example, the spot size in (c) at time $t = -0.6$ ps is approximately 2 mm. This output spot size is expected for an input spot size in (b) of approximately 0.2 mm, considering that the focal length of the lens CL was 50 cm, according to the relation

$$2W_o = \frac{4\lambda}{\pi}\frac{F}{D}.$$
(2.38)

Here, D is the input spot size (0.2 mm), F is the lens focal length (50 cm), and $2W_o$ is the output spot size (2.5 mm).
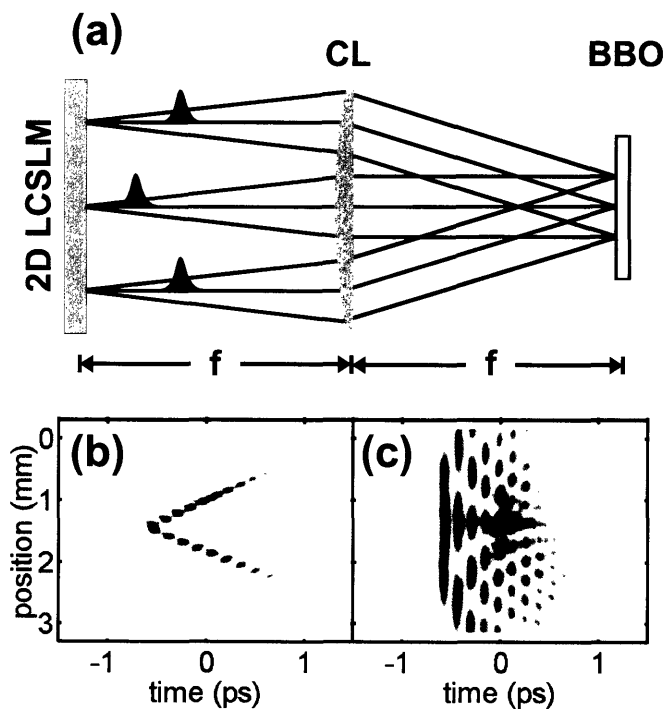
Figure 2-28: (a) Schematic illustration of the Fourier relationship between real-space shaping and wavevector shaping. The real-space shaping waveform in (b) and the corresponding wavevector-shaping waveform in (c) were generated with the same phase pattern.

2.7.3 Wavevector Shaping, Arbitrary Intensity Profiles

The conceptually simple examples of wavevector shaping shown thus far only begin to explore the range of waveforms obtainable through wavevector shaping. A more powerful and general approach is to view wavevector shaping as a two-dimensional diffractive technique, where the two dimensions available are the vertical spatial dimension and the horizontal spectral dimension. Based on this approach, we were able to generalize the Gerchberg-Saxton algorithm [76] to generate two-dimensionally shaped laser pulses. Prior to this, the algorithm had been applied to transverse beam shaping [75] and to temporal-only pulse shaping [70, 57]. Using our implementation, almost any gray scale image can be converted to a corresponding space-time image and the phase pattern needed to generate the waveform is iteratively determined by the algorithm. The outcome of such a procedure is shown in fig. 2-29. As in the simpler waveforms illustrated in fig. 2-25, the spatial distribution of light has been changed considerably from that of the incoming pulse. Note that the standard simulated annealing or genetic algorithm approaches used in determining the phase pattern necessary to create a user-defined waveform for one-dimensional pulse shaping (for instance, [77, 78, 79]) would be prohibitively time consuming. For a LC SLM with 7-bit resolution in each of 480×480 pixels, there is a staggering $2^{1612800}$ ($> 10^{485501}$) possible combinations of phase patterns, compared with the mere 2^{896} ($> 10^{269}$) combinations possible with a conventional 7-bit, 128 pixel one-dimensional LC SLM.

A schematic illustration of the Gerchberg-Saxton algorithm applied to wavevector shaping is illustrated in fig. 2-30. The algorithm uses two constraints, the spatial/spectral amplitude profile of the input pulse at the plane of the SLM $A_o(y, \Omega)$, and the desired wavevector/temporal amplitude profile of the output waveform $d(\nu_y, t)$, to determine the phase pattern $\phi(y, \Omega)$ required to generate the desired output waveform. The algorithm begins in the position/frequency domain with the input pulse amplitude $A_o(y, \Omega)$ and an input phase which is unimportant and can be set to any value for the initialization step. Next, the input pulse is Fourier-transformed
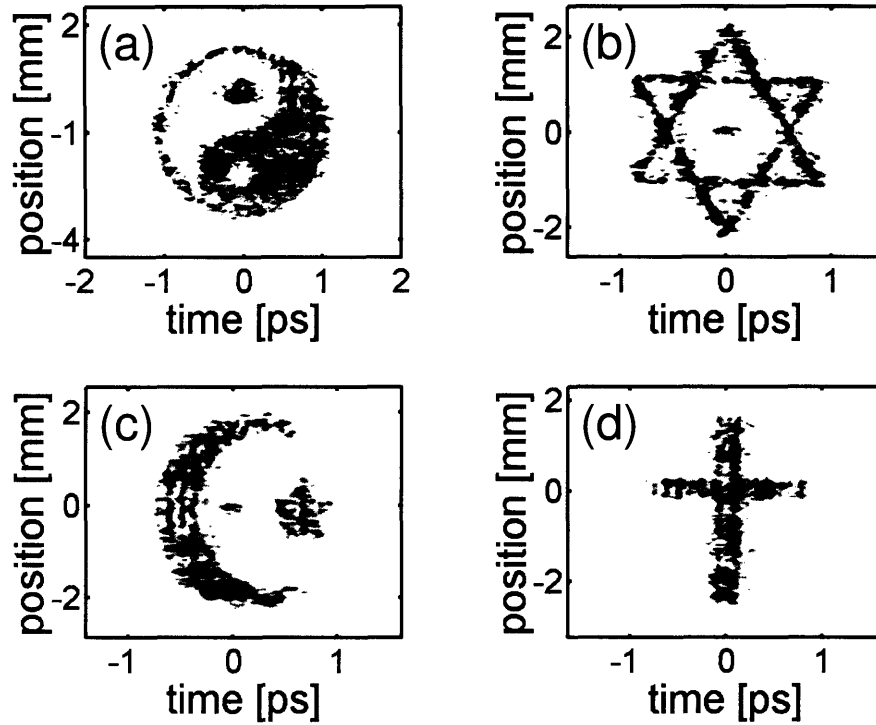
Figure 2-29: (a)-(d) Complex user-defined waveforms generated via wavevector shaping.

(frequency to time) and inverse-Fourier-transformed (position to wavevector), after which the wavevector/time amplitude profile $a_k(\nu_y, t)$ labelled by iteration index k is replaced by the desired amplitude $d(\nu_y, t)$. The new field $d(\nu_y, t)\exp[i\theta_k(\nu_y, t)]$ is then subjected to inverse Fourier-transformation (time to frequency) and Fourier-transformation (wavevector to position), at which point one cycle of the algorithm has been completed. The next cycle begins after the amplitude profile of the field $A_k(y, \Omega)\exp[i\theta_k(\nu_y, t)]$ is replaced by the original input pulse amplitude $A_o(y, \Omega)$ profile. After many cycles, typically 5-30, the phase pattern $\phi(y, \Omega)$ is obtained. Taken all together, the algorithm performs successive transformations between the position/frequency and wavevector/time domains, imposing amplitude constraints in each domain [$A_o(y, \Omega)$ or $d(\nu_y, t)$, respectively] but retaining the phase terms in every step. Reference [75] proves the convergence of the Gerchberg-Saxton algorithm for many implementations in Fourier beam-shaping applications. Note that the graininess of the images in fig. 2-29 is largely a result of the smoothness of the pixels in our

Initialize

$A_o(y,\Omega)\exp[i\varphi_k(y,\Omega)]$
$k=0$

①   ②

$A_o(y,\Omega)\exp[i\varphi_k(y,\Omega)]\xrightarrow{\textbf{FT \& IFT}} a_k(\upsilon_y,t)\exp[i\theta_k(\upsilon_y,t)]$

replace $A_k(y,\Omega)$ **replace $a_k(\upsilon_y,t)$**
with $A_o(y,\Omega)$ **with $d(\upsilon_y,t)$**

$A_k(y,\Omega)\exp[i\varphi_k(y,\Omega)]\xleftarrow[k\to k+1]{\textbf{FT \& IFT}} d(\upsilon_y,t)\exp[i\theta_k(\upsilon_y,t)]$

④   ③

$\varphi_k(y,\Omega)$
Output phase
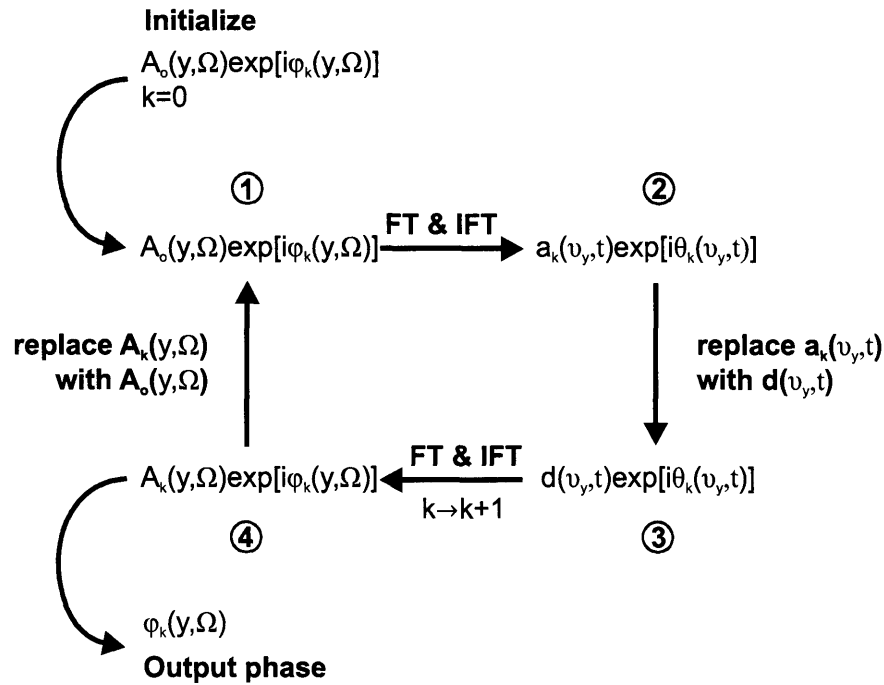
Figure 2-30: Schematic illustration of the Gerchberg-Algorithm applied to wavevector shaping. See text for description.

optically-addressed 2D LC SLM. Simulations of the waveforms in fig. 2-29 (a) and (b) that account for pixel smoothness in two dimensions reproduce the graininess quite well (fig. 2-31) while simulations with perfectly sharp SLM pixels (not shown) produce much smoother output waveforms.

Some fundamental differences between real-space and wavevector shaping warrant discussion. First, in real-space shaping, the spatial distribution of energy in the incident laser pulse is preserved in the final waveform (up to a constant magnification factor depending on the choice of imaging optics), regardless of the temporal profile of each horizontal slice. Furthermore, real-space shaped waveforms are inherently pixelated along the vertical direction, although a large number of pixels in the vertical dimension may at times give the impression of continuous patterns. On the other hand, wavevector shaped pulses are not directly mapped from the LC SLM to the sample, allowing the energy to be distributed across the sample nearly arbitrarily and in smoother patterns. The locations of replica features in the two techniques predisposes wavevector shaping to waveforms possessing inversion symmetry and real-
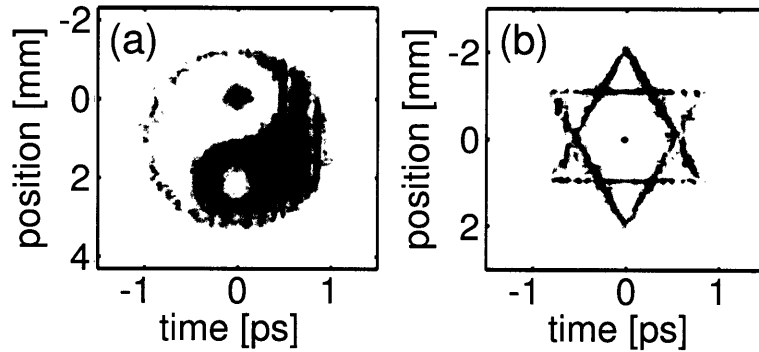
Figure 2-31: (a)-(b) Simulation of complex user-defined waveforms created via wavevector shaping, accounting for the smoothness of pixel boundaries in the 2D LC SLM.

space shaping to waveforms with mirror symmetry about the time axis. Lastly, unlike real-space shaping, wavevector shaping allows the spatial redistribution of the spectral intensity and manipulation of spectral phase within a shaped laser pulse, important capabilities that will be the subjects of the next two sections.

2.7.4   Wavevector Shaping, Modifying Spectral Content

Static optical elements such as prisms and diffraction gratings have traditionally been used to spatially disperse the spectral components of a beam of light. While these widely-used optical elements are simple and robust, they are also inflexible. First, a given prism or grating only possesses a single degree of freedom influencing the spectral dispersion, namely the angle of incidence, and adjusting this degree of freedom is often cumbersome and time consuming. Frequently, gratings or prisms must be exchanged in an optical apparatus when a different amount of dispersion is desired. Furthermore, both prisms and gratings are limited to dispersing spectral components in the "natural" order (forwards or backwards) of the colors of the rainbow. The wavevector shaping apparatus provides the ability to control the spectral dispersion in a nearly arbitrary manner and with excellent fidelity. Although a pixelated LC SLM is used here, it should be possible to create a piezo-controlled, deformable mirror membrane that would be able to apply a smoothly-varying spatial tilt to the input spectral components such that the output spectrum would also be smoothly-varying.

71
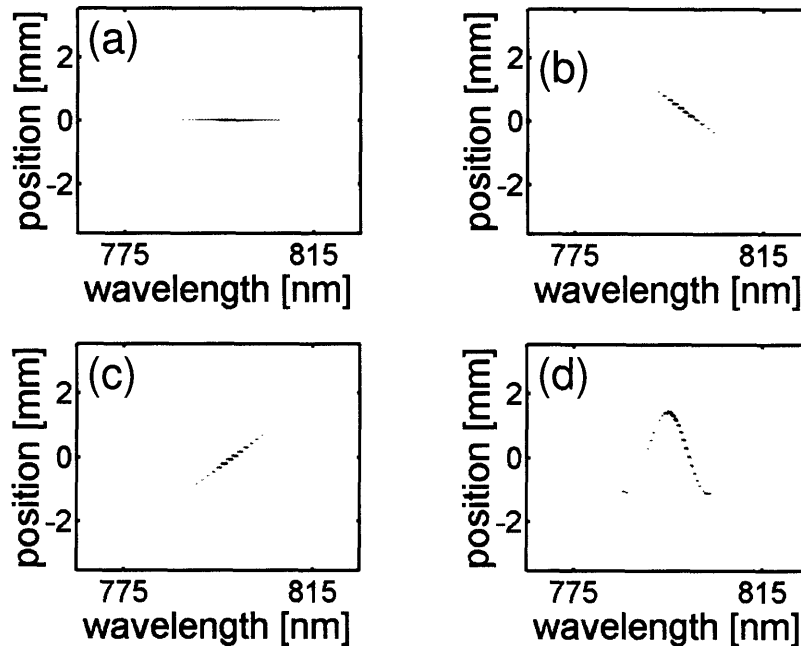
Figure 2-32: Reconfigurable spectral dispersion by the wavevector shaping apparatus. (a) Unmodulated spectrum. Positive (b) and negative (c) dispersion of the spectrum. (d) Sinusoidal dispersion of the spectrum, a simple example of a task not possible by conventional dispersive elements.

Fig. 2-32(b) and (c) demonstrates the reconfigurable dispersion of our laser spectrum in the order of the colors of the rainbow to different vertical positions. An "unnatural" dispersion configuration is shown in (d), in which frequency components have been dispersed to different vertical positions in the shape of a sine wave. The phase pattern applied by the LC SLM in figs. 2-32 and 2-33 consists of linear spatial phases with different slopes applied to different vertical slices of the LC SLM in order to shift the spot of a given spectral component to the desired height. Spectra at different vertical spatial positions were measured by placing a homemade imaging spectrometer at the focal plane of the output (see figs. 2-24 and 2-28).

One possible application of controllable spectral dispersion is in the area of optical networking, particularly wavelength-division multiplexing. Similar ideas have been explored in the literature. For instance, De Souza et al. [80] and Ford et al. [81] have used tilting micromirror elements at the spectral plane of apparatuses similar to ours. The micromirrors were capable of two-state operation, such that multiple spectral

bands, or channels, were steered to one of two locations. Patel and Silberberg [82] used a LC SLM to independently modulate the polarization of multiple channels of an input pulse to be one of two polarization states, such that after the output passed through a birefringent crystal, the different channels were spatially separated into two polarization groups. Elsewhere, LC SLMs have been used to 'steer' an input beam (that has not been spectrally dispersed) to multiple locations, for example Tan et al. [83, 84].

To the best of our knowledge, however, there has not been a report demonstrating the combination of beam steering with spectral selectivity, which may be generically stated as routing a beam of light containing M frequency bands to any of N locations. Such a device would have numerous possible applications in optical communications. A demonstration of the wavelength-routing capabilities of the wavevector shaping apparatus is shown in fig. 2-33, where the frequency components of an input beam have been divided into 20 channels (vertical lines in fig. 2-33), and 20 positions, or addresses (horizontal lines in fig. 2-33), have been identified. By varying the phase pattern on the 2D SLM, any of the 20 channels may be directed to any of the 20 addresses. The method allows for further sophistication by using more general spatial phase patterns within a given channel such that the channel may be split amongst many locations as desired. Lastly, the same methods may be used to accomplish the reverse tasks to those demonstrated above, namely, combining light from multiple sources with different frequency bands into a single output beam.

2.8   Diffraction-Based Phase and Amplitude Pulse Shaping

While the wavelength-routing capabilities briefly mentioned above are beyond our present research interests, the ability to modify the spectral amplitude of the output beam at a given location does have immediate application in a new and useful variation on phase and amplitude femtosecond pulse shaping. Namely, variable amounts
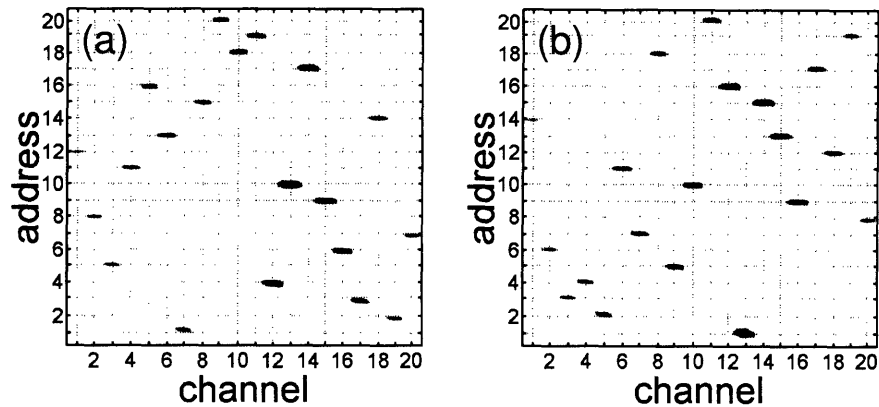
Figure 2-33: Demonstration of spectral routing, in which different frequency component, or channels, are routed to different vertical spatial locations.

of the input spectrum may be diffracted slightly upwards and with a controlled phase such that the spectral phase and amplitude of the diffracted beam may be independently determined, even though the 2D LC SLM itself only performs phase modulations on the input light. This scheme is extendable to several independent and phase-stable outputs, a scheme that opens up exciting prospects for coherent nonlinear spectroscopic experiments (see chapter 4). This diffractive mode of operation is reminiscent of acousto-optic modulation, (a method also used for pulse shaping [26]), although the 2D LC SLM allows for 480 independent channels (one for each spectral component) and has a very high diffraction efficiency (>95%).

In our diffraction-based pulse shaping scheme [41], the laser spectrum is dispersed horizontally, and a sawtooth phase function is applied along the vertical direction by the 2D LC SLM to each frequency component (fig. 2-34[a]). Much like a blazed diffraction grating, the direction of the first-order diffracted light for a given frequency component is determined by the period of the sawtooth phase function, which is set constant for all frequency components within the laser bandwidth. The spatial phase (i.e. vertical position) and amplitude of the sawtooth pattern may be varied for each spectral component in order to modulate the phase and amplitude, respectively, of the light diffracted into the first order. Finally, a spatial aperture may be used to mask out all but the first-order diffracted light before an additional lens collimates the beam.
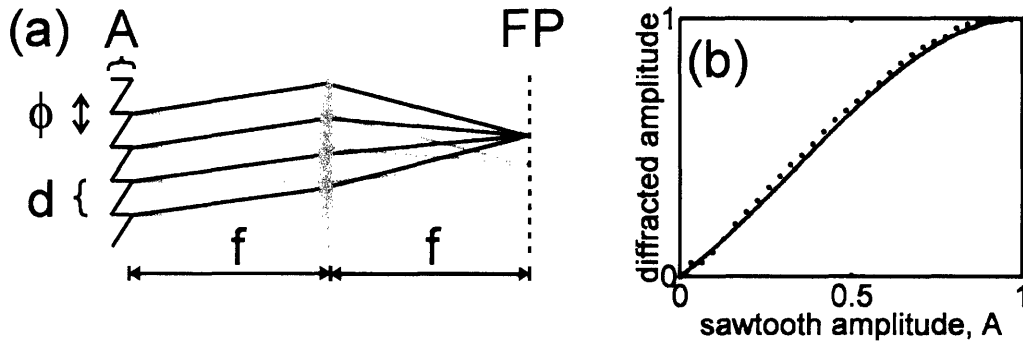
Figure 2-34: (a) Schematic illustration of diffraction-based pulse shaping. A sawtooth phase modulation with period d, amplitude $A(\Omega)$, and phase $\phi(\Omega)$ is applied by the 2D LC SLM to a given spectral component in order to control the phase and amplitude of the light diffracted into first order. A lens with focal length f produces at the focal plane FP a spatial Fourier transform of the light at the 2D LC SLM. (b) Measured amplitude (dotted line) of diffracted light as a function of sawtooth amplitude A, in good agreement with the expected sinc behavior (solid curve).

The phase and amplitude dependence of the diffracted light may be easily understood in terms of Fraunhofer diffraction (fig. 2-34[a]). The sawtooth phase modulation $\Lambda(y)$ applied by the 2D LC SLM to a given spectral component is of the form

$$\Lambda(y) = \mathrm{comb}\left(\frac{y-\epsilon}{d}\right) \otimes \left(\mathrm{squ}\left(\frac{y}{d}\right)\exp\left[i\frac{A\mu y}{d}\right]\right), \tag{2.39}$$

where y is the spatial coordinate, d is the period of the sawtooth function, and ϵ is the spatial displacement of the sawtooth function. The amplitude of the sawtooth function has been expressed as a product of the maximum phase shift attainable by the SLM, μ, and a fractional amplitude parameter A. Similar to eq. 2.9, the modulated input beam is given by

$$E_{out}(y) = \Lambda(y)E_{in}(y). \tag{2.40}$$

The resulting diffraction at the focal plane of the lens can be determined by inverse Fourier-transformation to be

$$e_{out}(\nu_y) = \lambda(\nu_y) \otimes e_{in}(\nu_y). \tag{2.41}$$

75

The function $\lambda(\nu_y)$ can be determined by use of the convolution and Fourier-shift theorems to give

$$\lambda(\nu_y) \propto \mathrm{comb}(\nu_y d)\exp(-i2\pi\epsilon\nu_y)\mathrm{sinc}\,(\pi d\nu_y + A\mu/d)\,. \qquad (2.42)$$

This result may be simplified by considering the phase and amplitude in the vicinity of the first-order diffraction spot (where $\mathrm{comb}(\nu_y d) = \delta(\nu_y + 1/d)$), yielding

$$e_{out1}(\nu_y^{(1)}) \propto e_{in}(\nu_y)\exp(i2\pi\epsilon/d)\mathrm{sinc}[\pi - A\mu/2], \qquad (2.43)$$

where the notation $\nu_y^{(1)}$ indicates that only wavevectors in the vicinity of the first order diffraction are being considered. It is assumed that the other diffraction orders are sufficiently well separated in space to be unimportant (i.e. they may be blocked with an aperture). From eq. 2.43 it is clear that the phase of the diffracted light may be controlled by varying the spatial phase, i.e. the vertical position, of the sawtooth function, while the amplitude of the diffracted light follows a sinc dependence on the amplitude parameter A. Figure 2-34(b) shows that the measured amplitude of the diffracted light agrees well with the expected sinc behavior. For the present 2D LC SLM, $\mu = 2\pi$.

An interesting aspect of eq. 2.43 is that the spectral phase of the diffracted light is independent of μ, the maximum phase modulation achievable by the SLM. Therefore, a 2D SLM with $\mu < 2\pi$ still has the ability to shift the phase of the diffracted light by up to 2π, although the maximum attainable amplitude is less than 1. For example, a 2D SLM with a maximum phase shift of π in reflection mode would have a corresponding maximum achievable amplitude in diffraction mode of $\mathrm{sinc}(\pi/2) = 0.64$. If the loss of efficiency can be tolerated in applications, then the diffraction-based approach would allow, for example, direct phase and amplitude pulse shaping in the near to mid infrared with 2D microelectromechanical (MEMS) SLMs that are currently available but can only provide a 2π phase shift for wavelengths up to 900 nm [85]. In the present scheme, a SLM with $\mu > 2\pi$ would not benefit from the additional phase modulation range.

Finally, eq. 2.43 may be adapted to account for all spectral components by varying the sawtooth phase and amplitude parameters ϵ and A for different frequencies. The resulting first-order diffraction at the focal plane of the lens is

$$e_{out1}(\Omega, \nu_y) \propto e_{in}(\Omega, \nu_y^{(1)}) \exp[i\phi(\Omega)]\text{sinc}[\pi(1 - A(\Omega))]. \qquad (2.44)$$

For experimental measurements in this section, nearly bandwidth-limited 805 nm, 1.5 mJ, 40 fs pulses from a 1 kHz repetition rate amplified Ti:Sapphire laser were used. The focal length of the lens in fig. 2-34 was 40 cm. The period of the sawtooth pattern on the 2D LC SLM was 0.67 mm for all spectral components. For the relatively small fractional bandwidth laser pulses used here, the large sawtooth period produced negligible spatial chirp. Laser pulses which are very short and therefore have a large fractional bandwidth may require the use of a wavelength-dependent sawtooth period in order to avoid spatial chirp. The wavelength-dependent sawtooth period necessary to diffract all spectral components to exactly the same spatial location is easily determined. Since the first-order diffraction occurs when $\nu_y = -1/d$, and since the wavevector $-1/d$ corresponds to the position $y' = f\lambda/d$, it follows that d should be chosen to be $d = d_o\lambda/\lambda_o$. Here, d_o is the period of the sawtooth at a given wavelength λ_o.
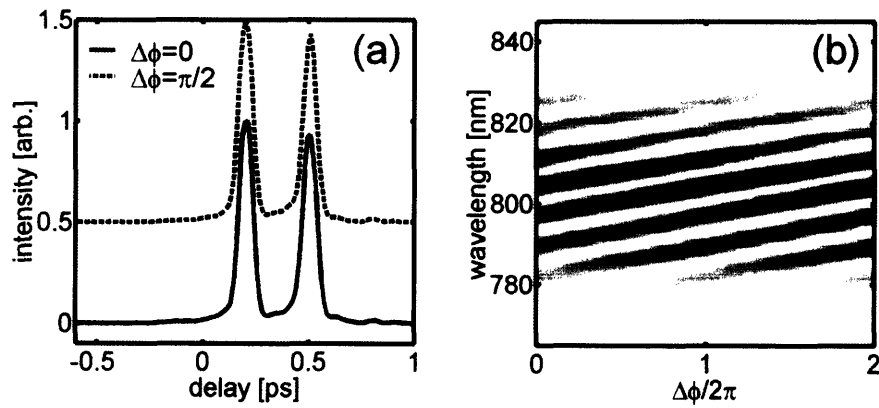
Figure 2-35: (a) Intensity cross correlations of two phase-related double-pulse waveforms. (b) Spectral intensity profiles of many double-pulse waveforms measured as the phase difference between the two pulses was scanned.

The phase and amplitude shaping capability achievable with diffraction-based

pulse shaping is illustrated in fig. 2-35. Intensity cross-correlations of two phase-related double-pulse waveforms were performed with an unshaped reference pulse (fig. 2-35[a]). To create the double-pulse, a 3.3 THz cosine-squared amplitude modulation was applied to the laser pulse in combination with a linear spectral phase of slope 0.35 ps. The measured pulse positions are in agreement with the expected positions at 0.2 ps and 0.5 ps. The relative phase of the pulses in a double pulse waveform may be inferred by observing the spectral position of the cosine-squared spectral amplitude modulation that produces the waveform. A measurement of the spectral intensity of many double pulse waveforms is shown in fig. 2-35(b) as the relative phase between the two pulses, $\Delta\phi$, is scanned. Comparison of vertical slices through fig. 2-35(b) for $\Delta\phi = 0$ and $\Delta\phi = \pi/2$ reveals that the fringes in the spectral intensity of the two waveforms in fig. 2-35(a) are shifted by $\pi/2$.

A notable property of diffraction-based pulse shaping is that it suppresses modulator replica pulses. To demonstrate this, first, an intensity cross-correlation was performed on a shaped pulse resulting from the application of a linear spectral phase with a slope of 2 ps (fig. 2-36[a]). In this case, there was no phase variation in the vertical dimension of the 2D LC SLM and no vertical deflection of the shaped pulse, although the apparatus itself was identical to the one used for real space shaping described in section 2.5. Modulator replica pulses are visible at -4, 0, 2, and 4 ps in addition to the intended pulse at -2 ps. The modulator replica pulses are larger for the optically addressed, reflection mode 2D LC SLM used in the present experiments than they would be with standard transmissive 1D LC SLMs since the 2D LC SLM has rather smooth pixel boundaries [39]. Next, the same linear spectral phase modulation was applied through diffraction-based pulse shaping, with the effect that the modulator replica pulses are distributed both in time and space, as shown in the spatially-resolved cross-correlation in fig. 2-36(b). To perform the spatially-resolved cross-correlation, the background-free cross-correlation signal at the BBO crystal was imaged on to a CCD camera. The relative intensities of the replica features in the diffraction-based shaped waveform, when summed over all positions (fig. 2-36[c]), are quite similar to those in obtained through reflection-mode pulse shaping (fig. 2-36[a]).
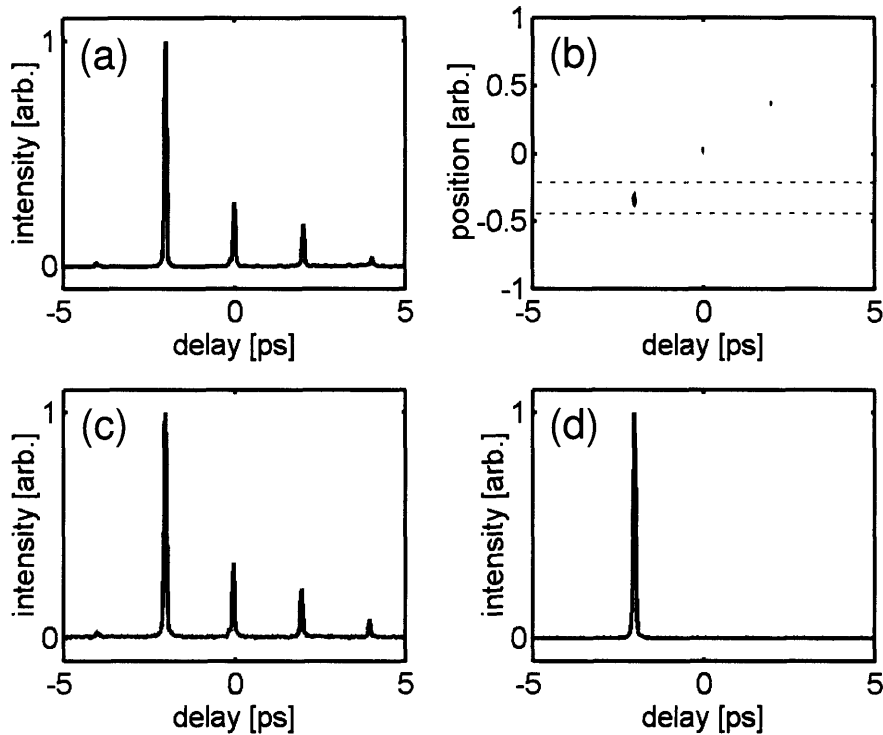
Figure 2-36: (a) Intensity cross correlation of the waveform resulting from the application of a linear spectral phase with slope 2 ps in a conventional (reflective) manner. (b) Spatially-resolved intensity cross-correlation of a waveform with the same spectral phase modulation as in (a) but generated using the diffraction-based pulse shaping scheme. Many higher order diffracted pulses are displaced in both space and time. (c) Integral of (b) over all positions, including many diffraction orders. (d) Integral of (b) over position in the vicinity of the first order diffracted light (between the dashed lines).

Lastly, the spatially resolved cross-correlation measurement (fig. 2-36[b]) shows that the modulator replica pulses are eliminated in the vicinity of the first order diffracted light, such as would be obtained if a spatial filter were used to block all but the first-order diffracted light (fig. 2-36[d]).

Although modulator replica pulse distortions are often in the form of simple and discrete pulses, as was shown above, they can also result in more complicated waveform distortions, especially when the modulator replica features overlap with the desired waveform such as when the desired waveform is not simply a short pulse. In these cases, the replica features and desired waveform interfere, resulting in distorted pulse shapes. Figure 2-37 illustrates the complications arising when replica

79
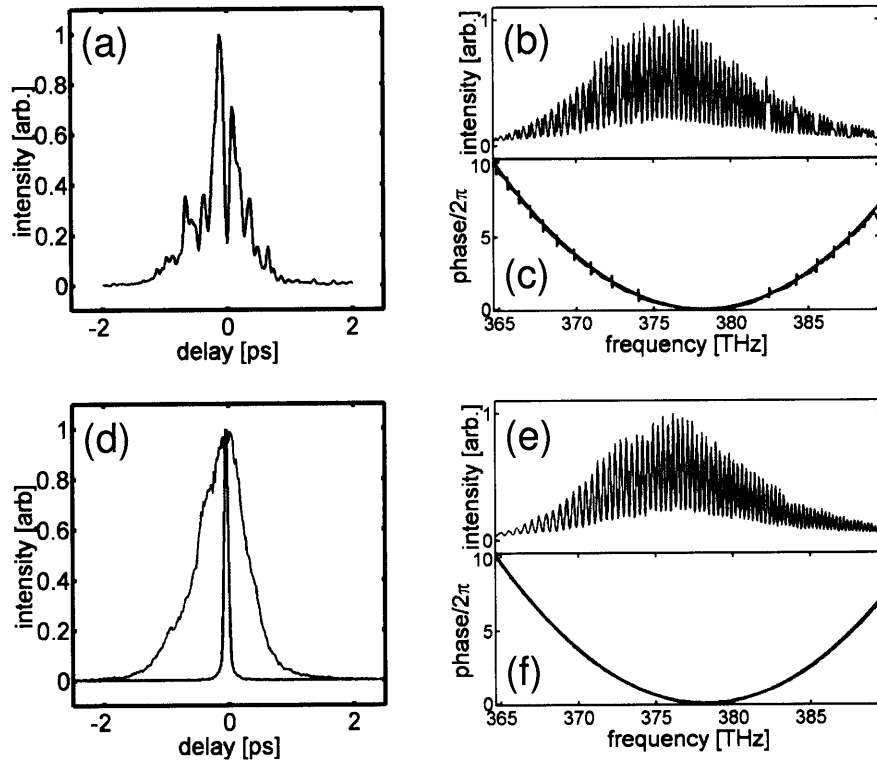
Figure 2-37: (a) Intensity cross correlation of the waveform resulting from the application of a large quadratic spectral phase in a conventional (reflective) manner. (b) Spectral interferogram of a chirped pulse generated with the reflective pulse shaping arrangement and (c) the corresponding extracted phase (blue curve) and desired phase (red curve). (d) Intensity cross-correlation of the same spectral phase modulation as in (a) but generated using the diffraction-based pulse shaping scheme (green curve). An unchirped pulse (blue curve), scaled so that its maximum is equal to that of the chirped pulse, is shown for comparison. (e) Spectral interferogram of a chirped pulse generated with the diffractive pulse shaping arrangement and (f) the corresponding extracted (blue curve) and desired (red curve) phases.

features interfere with the desired waveform. In the conventional, reflective pulse shaping mode, the waveform resulting from the application of a large quadratic spectral phase (0.05 ps^2) is greatly distorted by replica features overlapping in time and space with the desired, chirped waveform [fig. 2-37(a)]. To give an idea for how smoothing effects can distort the desired spectral phase, spectral interferometry was used to characterize a pulse shaped with nearly the same amount of chirp (0.06 ps^2) also using reflective pulse shaping arrangement. Examination of the spectral interferogram in (b) reveals periodic jumps in the spectral fringes. These jumps correspond

to the phase wrap locations and can be seen more clearly in (c), where the extracted phase (blue curve) has many noticeable deviations from the desired spectral phase (red curve). In contrast, diffraction-based pulse shaping separates the replica pulses from the desired waveform, resulting in a clean, chirped pulse whose structure is determined primarily by the spectrum of the laser pulses [fig. 2-37(b), green]. For reference, an unshaped pulse is shown on the same scale as the diffraction-based chirped pulse [fig. 2-37(d), blue]. The spectral interferogram (e) of a pulse with a chirp of 0.06 ps^2 that was generated with the diffraction-based apparatus now oscillates smoothly, and the extracted phase (blue curve) agrees nearly perfectly with the desired phase.
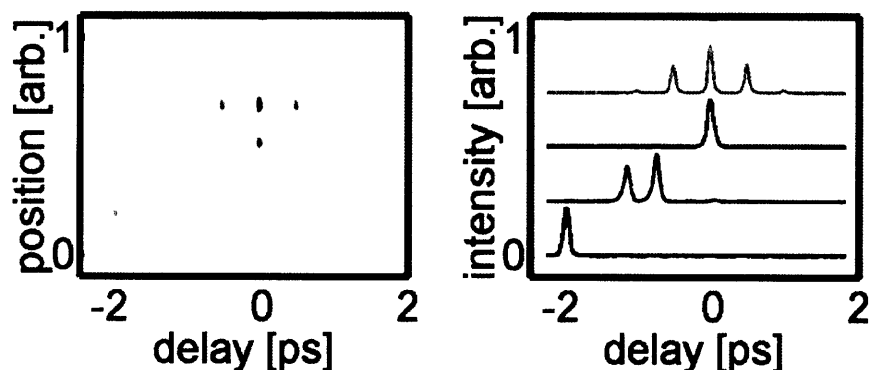
Figure 2-38: Demonstration of multiplexed phase and amplitude pulse shaping. (a) Angle-resolved intensity cross-correlation of four differently shaped waveforms. All but the first order diffraction was blocked by a pair of razor blades. (b) Separate cross-correlation traces through each of the four shaped waveforms.

The above results have demonstrated high quality phase and amplitude pulse shaping of a single output with diffraction-based pulse shaping. A further capability of the device is the generation of multiple phase and amplitude shaped outputs suitable for various applications, including phase-coherent nonlinear spectroscopy with multiple beams whose wavevectors meet the appropriate phase-matching condition [68]. To achieve this, four regions of the 2D LC SLM, each consisting of 60 rows of pixels, were used to generate four independently shaped outputs. Since the four regions of the 2D LC SLM used the same sawtooth period, all four shaped outputs were incident upon the same first-order position at the focal plane (FP in fig. 2-34[a]) although with different angles of incidence. A pair of razor blades was used to mask

81

all but the first order diffracted light at the focal plane. The four separate cross-correlation signals were simultaneously recorded by using a lens at 1-f distance from the focal plane to map the angular distribution of the cross correlation signal onto a CCD. The angle-resolved cross correlation signal and slices from each region are shown in figs. 2-38(a) and (b), respectively. The capabilities described here will be demonstrated in coherent nonlinear optical spectroscopy experiments in chapter 4.

2.9 Appendix 1: Mathematical conventions and important Fourier analysis relations

The conventions for Fourier transformation used in this thesis are listed below. Conjugate variables ν and t are used instead of ω and t, avoiding the awkward factor of $1/\sqrt{2\pi}$ used by many in Fourier transformation and inverse Fourier transformation. Similarly, ν_x and x are used instead of k_x and x for the wavevector-position variables, where $k_x = 2\pi\nu_x$. The conventions for transforming between the frequency-domain and the time-domain are shown in eq. 2.45, and the conventions for transforming between the position-domain and the wavevector-domain are shown in eq. 2.46. Note that lower-case and upper-case functions are used in the corresponding domains, such as $F(\nu)$ and $f(t)$. The convolution of two functions $F_1(\nu)$ and $F_2(\nu)$, symbolically represented by $F_1(\nu) \otimes F_2(\nu)$, is defined in eq. 2.47. See references [71, 86, 87] for further information on Fourier transformation and convolutions in the context of optics.

$$F(\nu) = \int_{-\infty}^{\infty} f(t) \exp(-i2\pi\nu t) dt \qquad f(t) = \int_{-\infty}^{\infty} F(\nu) \exp(i2\pi\nu t) d\nu \qquad (2.45)$$

$$G(y) = \int_{-\infty}^{\infty} g(\nu_y) \exp(i2\pi\nu_y y) d\nu_y \qquad g(\nu_y) = \int_{-\infty}^{\infty} G(y) \exp(-i2\pi\nu_y y) dy \qquad (2.46)$$

$$C(\nu) = F_1(\nu) \otimes F_2(\nu) = \int_{-\infty}^{\infty} F_1(\nu')F_2(\nu - \nu') d\nu' \qquad (2.47)$$

1	$\exp[-\Omega^2/\Delta\Omega^2]$	$\Leftrightarrow$	$\Delta\Omega\sqrt{\pi}\exp[-\pi^2\Delta\Omega^2 t^2]$
2	$\text{squ}[\Omega/\Delta\Omega]$	$\Leftrightarrow$	$\Delta\Omega\text{sinc}(\pi\Delta\Omega t)$
3	$\text{comb}[\Omega/\Delta\Omega]$	$\Leftrightarrow$	$\text{comb}[\Delta\Omega t]$
4	$A(\Omega)B(\Omega)$	$\Leftrightarrow$	$a(t)\otimes b(t)$
5	$E(\Omega)\exp[i2\pi\tau\Omega]$	$\Leftrightarrow$	$e(t+\tau)$
6	$e(y)\exp[i2\pi\sigma y]$	$\Leftrightarrow$	$E(\nu_y-\sigma)$

Table 2.1: Commonly encountered Fourier-transform relations. Note that Ω is used here ($\Omega = \nu - \nu_o$) instead of ν.

Frequently used Fourier-transformation pairs are listed in table 4.1, including the convolution theorem (line 4), and the Fourier-shift theorem for both the frequency-time and position-wavevector domains (lines 5 and 6, respectively). The function $\text{comb}(x)$ is defined as

$$\text{comb}(y) = \sum_{m=-\infty}^{m=\infty} \delta(y-m), \tag{2.48}$$

and the function $\text{squ}(x)$ is defined as

$$\text{squ}(x) = \begin{cases} 1 & |x| \le 1/2 \\ 0 & |x| > 1/2 \end{cases}. \tag{2.49}$$

In the paraxial or small-angle limit, Fourier-transformation by a lens maps (via Fraunhofer diffraction [71, 86, 87]) the modulated beam's wavevector distribution at the plane 1-f prior to the lens to position at the focal plane 1-f after the lens (fig. 2-39). The plane of the modulator will use the position variable y while the focal plane of the lens will use the position variable y'. The projection of the wavelength λ_y onto a line perpendicular to the optical axis is related to the angle of the diffracted ray

$$\sin\theta_y = \frac{\lambda}{\lambda_y} = \lambda\nu_y, \tag{2.50}$$

where $\nu_y = 1/\lambda_y$. For small θ_y, the position of the diffracted light at the focal plane of the lens is given by

83

$$\tan\theta_y = \frac{y'}{f} \approx \theta_y \approx \sin\theta_y = \lambda\nu_y, \tag{2.51}$$

yielding

$$y' = f\lambda\nu_y. \tag{2.52}$$

Equation 2.52 provides the means by which to translate the calculated diffracted waveforms in terms of the variable ν_y to position y' at the focal plane of the lens.
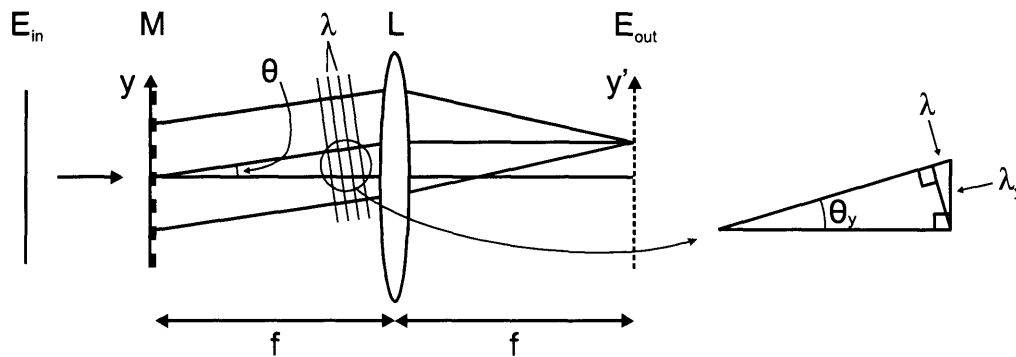
Figure 2-39: Schematic illustration of Fourier-transformation by a lens. Within the paraxial limit, the lens maps wavevector (immediately after the mask plane) to position (at the focal plane).

Table 2.2 provides a short list of commonly used pulse shapes, and the phase and/or amplitude patterns required to generate them assuming a perfect ability to modulate the spectral phase and amplitude. Corrections for the Gaussian-sinc time window or gaps are not included in table 2.2. See reference [31] for a description of these procedures.

The entries in table 2.2 specify the phase/amplitude patterns required to generate a desired waveform, assuming an input pulse with infinite spectral bandwidth (a δ-pulse). In practice, of course, pulses of limited spectral bandwidth are used, in which case the output pulse is the convolution of the input pulse with the δ-pulse response. The last entry specifies a general recipe for creating a desired series of n pulses with relative amplitudes A_n at times τ_n and with spectral phases $\phi(\Omega)$, a general case which includes several other shapes listed in table 2.2. There, the sum

84

1	shift waveform center to time τ	$\exp[-i2\pi\tau\Omega]$
2	chirped pulse (quadratic, spectral phase)	$\exp[i(\alpha\Omega^2 + \beta\Omega^3)]$
3	square pulse, $\mathrm{squ}[t/\Delta t]$	$\mathrm{sinc}(\pi\Delta t\Omega)$
4	pulse train, separation τ between pulses	$\exp[ia\sin(2\pi\tau\Omega)]$
5	double-pulse, separated by τ	$\cos(2\pi\tau\Omega)$
6	n-pulses with specified amplitudes, times, phases	$\sum_n A_n \exp[-i2\pi\tau_n\Omega + i\phi_n(\Omega)]$

Table 2.2: A list of commonly-used pulse or beam shapes and the idealized phase and/or amplitude profiles required for their generation.

should be evaluated, and then expressed in amplitude/phase form ($A(\Omega)\exp[i\phi(\Omega)]$) to determine the desired amplitude/phase to be applied to the laser spectrum. In some cases, the desired amplitude would be negative, such as when creating a square pulse with spectral amplitude $A(\Omega) = \mathrm{sinc}(\pi\Delta t\Omega)$. Since a negative amplitude is equivalent to a positive amplitude combined with a π phase shift (in the complex representation) the absolute value of the desired amplitude modulation should be applied, $A(\Omega) = |\mathrm{sinc}(\pi\Delta t\Omega)|$, and the spectral phase should be shifted by π in the regions which require a negative amplitude, $\phi(\Omega) = \pi\mathrm{sign}\ [\mathrm{sinc}(\pi\Delta t\Omega)]/2$. This procedure should be used whenever a negative amplitude is required.

Note that the entries in table 2.2 may be used in combination with each other by simply using the product of multiple phase/amplitude functions. For instance, a chirped pulse train, where each pulse of the train has been chirped equally, requires the combination of a quadratic spectral phase (line 2) and a sinusoidal spectral phase (line 4). The overall phase modulation to apply in that case would then be $\exp[i(\alpha\Omega^2 + a\sin(2\pi\tau\Omega))]$.

Chapter 3

Coherent Control of Lattice Excitations Travelling at Light-Like Speeds

Based on the work by Auston [88] and others, femtosecond laser pulses with durations of 200 fs or less have been used to generate broadband pulses of THz radiation as short as a single or even a half cycle [89]. This development opened the door for femtosecond-based sources of coherent far-infrared radiation, for which there is little practical alternative. The terahertz, or far-infrared spectral region, usually considered to be 0.1-10 THz ($\lambda = 3 - 0.03$ mm $\Leftrightarrow$ $3.3 - 330$ cm^{-1}), is intermediate between electronic sources that can operate out into the many gigahertz regime and optical sources that can operate out to approximately the mid-infrared region. To date, terahertz sources based on femtosecond-laser excitation have been applied to numerous problems of interest, including molecular spectroscopy within flames [90], tomographic imaging [91], and sensing of biological agents [92].

Terahertz sources have also been proposed for applications in coherent control [93], signal processing [94], nonlinear THz spectroscopy [95, 96, 97, 98], quantum computation [99], etc., although many of these proposed applications require a degree of control over the terahertz waveforms that until recently has not been possible [100, 101]. Additionally, many scientists have interests in generating very large pulses

of THz radiation for nonlinear spectroscopic studies in the THz region of the spectrum (for instance [102, 103, 104, 105]). The Nelson group in particular has had a long-standing goal of initiating and studying large-amplitude displacements in ionic crystals in order to determine non-parabolic contributions to their potential energy surfaces that are known to exist but which have received almost no attention in the literature due to technological difficulties in making large-amplitude THz fields required for such experiments.

In this chapter we will describe a new approach to generating THz radiation based on phonon-polaritons, which are coupled lattice-vibrational and electromagnetic modes of ionic crystals that propagate at light-like speeds. Sections 3.1, 3.2, and 3.3 provide a brief introduction to phonon-polaritons and discuss methods for generating and detecting them. Sections 3.4 and 3.5 describe experiments in which the two-dimensional pulse shaping method presented in chapter 2 are applied to the control of phonon-polaritons and the generation of large-amplitude THz pulses. Section 3.6 presents a new and simple method for THz waveform generation based on shaping of the transverse spatial profile of a single, short excitation laser pulse.

3.1   Introduction to Phonon-Polaritons

Phonon-polaritons are coupled lattice-vibrational and electromagnetic modes of ionic crystals that propagate at light-like speeds with frequencies typically in the range 0.1-5 THz. Simply put, they are part vibration and part radiation. The coupled nature of phonon-polaritons results in the ability to use them as both a probe of the host material, for instance to study soft phonon modes in a ferroelectric crystal, and as a source of coherent electromagnetic radiation, such as for dielectric spectroscopy in the otherwise difficult to access THz frequency range. A brief theoretical description of phonon-polaritons is included below. For a more detailed analysis, see references [106, 18, 107, 108, 109, 110]

Phonon-polaritons in ionic crystals such as $LiTaO_3$ or $LiNbO_3$ are described by the following set of coupled equations,

$$\ddot{Q}(t) = -\omega_{TO}^2 Q(t) - \Gamma \dot{Q}(t) + b_{12} E(t) \tag{3.1}$$

$$P(t) = b_{21} Q(t) + b_{22} E(t) \tag{3.2}$$

where $Q(t)$ is the normal mode coordinate of the transverse optical phonon with frequency ω_{TO}, Γ is a phenomenological damping constant, $E(t)$ is electric field, $P(t)$ is polarization, and where $\dot{Q}(t)$ and $\ddot{Q}(t)$ represent first and second temporal derivatives of $Q(t)$, respectively. A single oscillator model is assumed valid here. The constants b_{12}, b_{21}, and b_{22} will be discussed below. $P(t)$, $E(t)$, $Q(t)$, etc. have been expressed as scalar quantities, which is sufficient for the present analysis. In physical terms, equation 3.1 describes a damped harmonic oscillator with an additional term $b_{12} E(t)$ governing the coupling of the polar vibrational displacements to to an electric field. Equation 3.2 describes the dielectric response of the coupled system in two terms, where the first term describes the polarization response due to the phonon mode (essentially dipole times ionic displacement) and where the second term describes the polarization response of the crystal due to all other effects. Using equations 3.1 and 3.2 and the constitutive relation for the electric polarization $P(t)$ we will next determine the relative permittivity of the coupled system.

The constitutive relation for electric polarization is

$$P(\omega) = \epsilon_o \chi(\omega) E(\omega)$$

$$= \epsilon_o \left(\varepsilon_r(\omega) - 1 \right) E(\omega) \tag{3.3}$$

where ϵ_o is the permittivity of free-space, $\chi(\omega)$ is the dielectric susceptibility, and $\varepsilon_r(\omega)$ is the relative permittivity. Inserting trial plane-wave solutions of the form $Q(t) = |Q(t)| \exp[i(kx - \omega t)]$ and $E(t) = |E(t)| \exp[i(kx - \omega t)]$ into equation 3.1 yields an expression for Q in terms of frequency,

$$Q(\omega) = \frac{b_{12}E(\omega)}{\omega_{TO}^2 - i\omega\Gamma - \omega^2}. \tag{3.4}$$

Substitution of eq. 3.4 into eq. 3.2 yields an expression for the polarization in terms of electric field which may then be equated to eq. 3.3, giving

$$P(\omega) = \left(\frac{b_{12}b_{21}}{\omega_{TO}^2 - i\omega\Gamma - \omega^2} + b_{22} \right) E(\omega) = \epsilon_o(\varepsilon_r(\omega) - 1)E(\omega). \tag{3.5}$$

Eq. 3.5 may now be used to solve for $\varepsilon_r(\omega)$:

$$\varepsilon_r(\omega) = \left(1 + \frac{b_{22}}{\epsilon_o} \right) + \frac{1}{\epsilon_o} \frac{b_{12}b_{21}}{\omega_{TO}^2 - i\omega\Gamma - \omega^2}. \tag{3.6}$$

Equation 3.6 contains two terms, the first of which is nonresonant and describes the system at frequencies above ω_{TO}, and the second of which describes the system near resonance.

The constants b_{12}, b_{21}, and b_{22} will now be determined by considering limiting cases for the relative permittivity. When $\omega \to \infty$, the resonant term in eq. 3.6 disappears, leaving

$$\varepsilon_r(\infty) = 1 + \frac{b_{22}}{\epsilon_o}. \tag{3.7}$$

Similarly, when $\omega \to 0$, we are left with

$$\varepsilon_r(0) = \varepsilon_r(\infty) + \frac{b_{12}b_{21}}{\epsilon_o \omega_{TO}^2}. \tag{3.8}$$

From the above equations, the constants b_{12}, b_{21}, and b_{22} are determined to be

$$b_{22} = \epsilon_o(\varepsilon_r(\infty) - 1)$$
$$b_{12}b_{21} = \omega_T^2 \epsilon_o(\varepsilon_r(0) - \varepsilon_r(\infty)). \tag{3.9}$$

Rather than explicitly working with b_{12}, b_{21}, and b_{22}, we will use ε_o and ε_∞, where these are defined as $\varepsilon_\infty \equiv \varepsilon_r(\infty)$ and $\varepsilon_0 \equiv \varepsilon_r(0)$, since these quantities have a clear

90

physical meaning. Now, we may rewrite eq. 3.6 as:

$$\varepsilon_r(\omega) = \varepsilon_\infty + \frac{\omega_{TO}^2(\varepsilon_o - \varepsilon_\infty)}{\omega_{TO}^2 - i\omega\Gamma - \omega^2}.$$ (3.10)

An important and well-known property of $LiTaO_3$ and $LiNbO_3$ is that phonon-polaritons exhibit a large dispersion resulting from a splitting between the relevant transverse optic phonon mode and the longitudinal optic phonon mode. In the optical regime, the dispersive properties of materials are often described in terms of a wavelength (or frequency) dependent index of refraction. Here, instead, the dispersion is customarily presented in terms of the dispersion relation $\omega(k)$. Using $\varepsilon_r(\omega) = n(\omega)^2 = c^2 k^2/\omega^2$, where n is refractive index, and assuming no damping, we obtain

$$\omega = \sqrt{\frac{\omega_{TO}^2\varepsilon_o + c^2 k^2}{2\varepsilon_\infty} \pm \frac{1}{2}\sqrt{\left(\frac{\omega_{TO}^2\varepsilon_o + c^2 k^2}{\varepsilon_\infty}\right)^2 - \frac{4\omega_{TO}^2 c^2 k^2}{\varepsilon_\infty}}}.$$ (3.11)
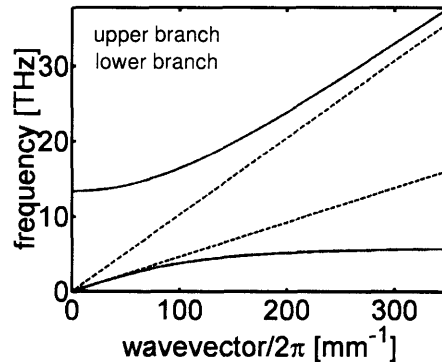
Figure 3-1: Simulated dispersion curve for $LiTaO_3$.

Two branches of solutions are obtained in the dispersion relation, the upper branch and the lower branch, as shown in fig. 3-1 (solid lines). For reference, fig. 3-1 also shows the asymptotic dispersion relations for far-infrared radiation, at frequencies far below the phonon resonance (dashed blue line), and for near-infrared radiation, at frequencies far above the phonon resonance (dashed red line). For the experiments presented here, only the lower branch of the dispersion curve is accessed, and only in the range of approximately 0.2-1 THz, where the dispersion is approximately linear

91

and the phonon-polaritons are considered to be primarily light-like.

3.2   Impulsive Stimulated Raman Scattering

For the experiments described in this thesis, phonon-polaritons are generated via impulsive stimulated Raman scattering, or ISRS, by irradiating the host crystal, either LiTaO$_3$ or LiNbO$_3$ with a short (<100 fs) laser pulse. Before examining the generation of phonon-polaritons, which are dispersive modes and behave differently than ordinary vibrational modes, we will first examine ISRS in the general case.

The basic physical picture of ISRS is most conveniently understood in the time domain in terms of a damped and driven harmonic oscillator, described by the differential equation

$$\ddot{Q}(t) + \Gamma \dot{Q}(t) + \omega_o^2 Q(t) = F(t), \tag{3.12}$$

where Q is the normal mode coordinate of a generic vibrational mode with resonant frequency ω_o, a damping term governed by Γ, and a driving term $F(t)$. Here, the driving term is the laser excitation pulse. In the "impulsive" limit, where an excitation laser pulse is much shorter than the period of the mode being excited, the force exerted by the laser excitation pulse is proportional to the product of the differential polarizability $(\partial \alpha / \partial Q)_o$ and the intensity of the excitation pulse $I_{exc}(t)$ [111, 112]

$$F(t) \propto - \left(\frac{\partial \alpha}{\partial Q} \right)_o I_{exc}(t). \tag{3.13}$$

If we consider the solution of eq. 3.12, when the input laser pulse is considered to be a delta-like pulse that arrives at time $t = 0$, the response function of the oscillator, $G(t)$, may be determined to be

$$G(t) \propto \Theta(t) \exp\left(-\frac{\Gamma t}{2} \right) \sin(\sqrt{\omega_o^2 - \Gamma/4}t), \tag{3.14}$$

where $\Theta(t)$ is the Heaviside step-function given by

$$H(t) = \begin{cases} 0 & t < 0 \\ 1 & t > 0 \end{cases}. \qquad (3.15)$$

The Heaviside step-function is necessary such that $G(t)$ is zero for negative times (i.e. prior to the excitation pulse). When an input pulse $I(t)$ of short but finite duration is used, $Q(t)$ may be determined by convolving the input pulse with $G(t)$,

$$Q(t) = I_{exc}(t) \otimes G(t). \qquad (3.16)$$

From equations 3.16 and 3.14, the expected response for a single vibrational mode is therefore a smoothed and damped sinusoid. Figure 3-2 shows ISRS measurements (taken with a setup similar to that described in [113]) of quartz; the crystalline solid bismuth germinate ($Bi_4Ge_3O_{12}$); and liquid tetrachloroethane. In the case of the signal from quartz, the expected 128 cm^{-1} mode is observed as a damped sinusoid. For bismuth germinate and tetrachloroethane, many vibrational modes are observed, giving rise to complex transient signals with many peaks in the frequency spectra.
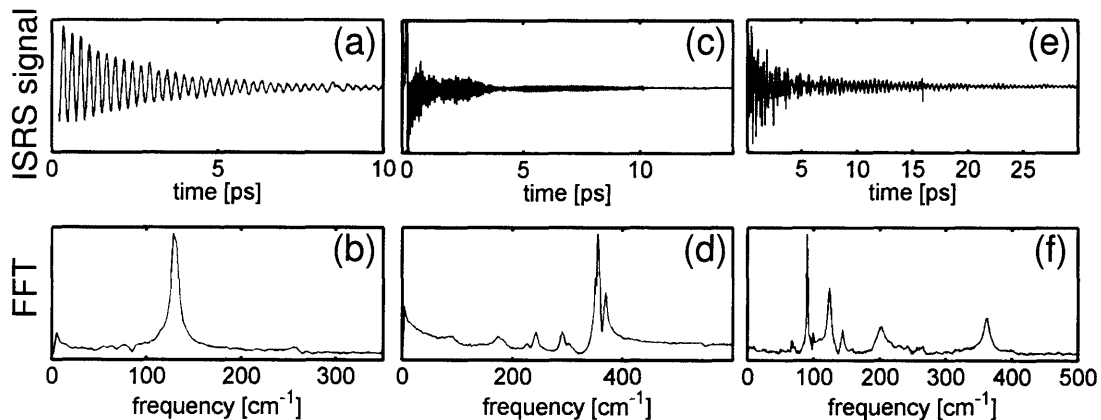
Figure 3-2: ISRS responses for (a) quartz, (c) tetrachloroethane, and (e) bismuth germinate (c), and their Fourier-transforms (b), (d), and (f), respectively.

The range of vibrational frequencies accessible by the input laser pulse is a simple function of the duration of $I_{exc}(t)$. In this case, we will use a Gaussian excitation pulse $I_{exc}(t) = I_o \exp(-\Delta\Omega^2 t^2/4)$, where $\Delta\Omega$ is the full-width half maximum of the

laser pulse spectral intensity (which is inversely proportional to the pulse duration). The range of available frequencies can then be determined by substituting eq. 3.14 into eq. 3.12, to get

$$Q(\omega) \propto \frac{\exp(-\omega^2/\Delta\Omega^2)}{\omega_o^2 - \omega^2 - i\Gamma\omega}.$$
(3.17)

Of course, to excite a vibrational mode in an "impulsive" manner, the excitation laser pulse duration must be shorter than half the oscillation period. This statement is equivalent to the result shown in eq. 3.17, where it is clear that the spectral bandwidth $\Delta\Omega$ of the laser pulse must span the resonance frequency of interest in order for $\omega/\Delta\Omega$ to be sufficiently small that $Q(\omega)$ is nonzero. Such an interpretation connects with the frequency-domain description of stimulated Raman scattering, since it says that the pump and Stokes frequencies must be contained within the broad bandwidth of the laser excitation pulse. Unlike conventional stimulated Raman scattering, where the pump and Stokes beams each consist of a single frequency, for ISRS, there is a continuum of pump and Stokes frequency pairs contained within the bandwidth of the laser pulse, all of which contribute (to varying degrees) to the response of the sample.

3.3   Generation and Detection of Phonon-Polaritons

In the case of phonon-polariton modes, eq. 3.1 can be modified to include the driving term $F(t)$, giving

$$\ddot{Q}(t) + \omega_{TO}^2 Q(t) + \Gamma\dot{Q}(t) - b_{12}E(t) = F(t),$$
(3.18)

which, together with eq. 3.2, describes the excitation of phonon-polariton modes. Unlike the vibrational modes illustrated in figure 3-2, where the motion of a given oscillator is essentially independent of the motion of other oscillators that are many unit cells away, phonon-polaritons show strong dispersion at long wavelengths due to long-range interactions among oscillators. This is caused by the coupling of os-

94

cillators through the electric field term $E(t)$. Because of this collective behavior, the observed frequency of phonon-polaritons generated via ISRS is a function of the phonon-polariton wavevector, as seen in fig. 3-1.

Another difference between phonon-polariton modes and ordinary vibrational modes is that phonon-polaritons, which are light-like in the experiments reported here, propagate rapidly across macroscopic distances in the host crystal. The group velocity, given by $\partial \omega / \partial k$, is a significant fraction of the speed of light in vacuum, as is evident in fig. 3-1. In lithium tantalate, it is approximately 1/6 the speed of light in vacuum ($n \approx 6$). The angle at which the phonon-polaritons propagate relative to the input pulse, θ_f is a simple geometric function of the group velocity of the excitation pulse, v_{exc} and the phase velocity of the phonon-polariton, v_{pol},

$$\theta_f = \sin^{-1}\left(\frac{v_{pol}}{v_{exc}}\right). \tag{3.19}$$

The end result is that phonon-polaritons resemble the wave left behind a boat that travels quickly across a pond, as can be seen in the illustration in fig. 3-3. For LiTaO$_3$, $\theta_f(\omega) \approx 70^o$.
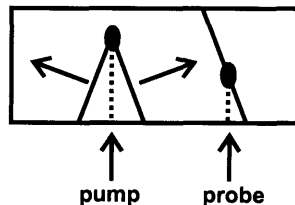
Figure 3-3: Phonon-polariton generation and detection with a short excitation pulse.

Phonon-polaritons may be detected in a variety of ways, but most of them rely upon the Pockel's effect [114, 115] in which an electric field modulates the index of refraction of a material. For the experiments reported here in the uniaxial crystals LiTaO$_3$ and LiNbO$_3$, the phonon-polaritons and laser excitation pulse are polarized parallel to the optic axis of the crystal, which in fig. 3-3 points out of the page. Analysis of the electro-optic tensor for LiTaO$_3$ and LiNbO$_3$ [114, 115] yields the following equations for the ordinary ($n_o(E_{pp})$) and extraordinary ($n_e(E_{pp})$) indices of refraction at optical wavelengths in the presence of an applied electric field E_{pp}

polarized along the extraordinary crystal axis,

$$n_e(E_{pp}) = n_e(1 - r_{33}n_e^2 E_{pp}) \qquad (3.20)$$

$$n_o(E_{pp}) = n_o(1 - r_{13}n_e^2 E_{pp}), \qquad (3.21)$$

where E_{pp} is the phonon-polariton electric field, r_{13} and r_{33} are the relevant electro-optic tensor elements, and n_e and n_o are the extraordinary and ordinary refractive indices in the absence of an applied field (see table 3.1). Through a variation in the index of refraction, then, the phonon-polariton amplitude may be determined. Many schemes can be used to detect these refractive index variations, but we make use of only two of these schemes, birefringence and shadowgraph imaging. Birefringence detection is illustrated in fig. 3-12, and shadowgraph imaging is illustrated in fig. 3-5. The former provides the time-dependent phonon-polariton response at a specified region of the crystal where the probe beam passes, while the latter provides the complete temporal and spatial evolution.

material	n_o	n_e	r_{13}	r_{33}
LiNbO$_3$	2.257	2.176	9.6	30.9
LiTaO$_3$	2.176	2.180	8.4	30.5

Table 3.1: Constants for modulation of the index of refraction due to phonon-polaritons from reference [115]. Units for r_{13} and r_{33} are pm/V.

For birefringence detection, a small, point-like probe beam polarized at $45°$ with respect to the optic axis is sent into the crystal (fig. 3-3) and then through a polarizer before its intensity is recorded by a photodetector. The electric field of the phonon-polaritons modulate the crystal's indices of refraction along the ordinary and extraordinary axes, influencing the polarization state of the transmitted probe beam. The variation in the polarization state influences the intensity of the probe beam upon passing through the polarizer, and this intensity is recorded as a function of probe delay in order to map out the time-dependent phonon-polariton waveform as it passes by a single point.

For shadowgraph imaging, a large probe beam is used to illuminate an extended region of the crystal in which the phonon-polariton is propagating. This large probe beam is then imaged to a CCD camera with a lens (typically 10 cm) which is situated two focal lengths after the crystal and approximately two focal lengths before the camera. Finally, the CCD camera is slightly displaced toward or away from the probe beam, yielding slightly out of focus images of the phonon-polaritons. The probe and excitation pulses are both polarized parallel to the crystal's extraordinary axis. The shadowgraph effect is similar in origin to the bright and dark patterns at the bottom of a swimming pool due to waves on the water's surface. Shadowgraphy converts phase shifts due to refractive index variations to amplitude modulations. More precisely, the amplitude of the recorded image is proportional to the second spatial derivative of the phase variations, by $\partial \phi^2 / \partial\ x^2$ [116].

A distinction should be drawn at this point between *shadowgraph imaging* and *Talbot self-imaging*, since the terms are often not correctly used. In Talbot self-imaging, there exist multiple planes before and after the actual image plane at which an amplitude-image of a periodic phase-object is produced. As pointed out by Koehl [117], the distance between these multiple amplitude-image planes is a function of the period of the phase-object being imaged, and thus the Talbot self-imaging plane is only well defined when the object being imaged is actually periodic. For that matter, the position of a self-imaging plane relative to the proper image plane is a function of the period of the phase-object being imaged, and therefore only the subset of phase-objects with the correct period are formed into a true amplitude-image at a given observation plane. The Talbot self-imaging phenomenon is merely a very special case of shadowgraph imaging, and one that is in fact seldom achieved.

Regardless of the detection method (birefringence detection or shadowgraph imaging), it is important that the group velocity of the probe be matched to the projection of the phonon-polariton phase velocity along the direction of the probe. In the analogy of a phonon-polariton wave resembling the wake left behind a boat travelling across a lake, the above condition is equivalent to requiring that the probe pulse act like a second boat that "surfs" along the first boat's wake always at a fixed point of the os-

cillation cycle. Since the measured phase shift (or birefringence) is an integral over the phase shifts (or birefringences) encountered by the probe pulse as it passes through the crystal, any difference between probe group velocity and the phonon-polariton phase velocity will cause a distortion in the measured phase shift (or birefringence). When the excitation pulse and the probe pulse are parallel and have the same group velocities, such as in fig. 3-3 (assuming that the excitation and probe pulses have the same polarization), the velocity matching conditions are automatically fulfilled.

For birefringence detection, a static birefringence in the generation crystal will cause the ordinary and extraordinary polarization components of the probe pulse to travel at different speeds and can introduce small distortions. As a benchmark, the static birefringence of a 1 mm crystal of $LiTaO_3$ for 800 nm light causes the extraordinary polarization component to lag behind the ordinary polarization component by only 5 optical cycles, or about 14 fs, which is less than the pulse width. In $LiNbO_3$, however, the static birefringence is roughly 20 times larger, causing the ordinary polarization component to lag the extraordinary polarization component by 100 optical cycles, or 270 fs, leading to weakly observable distortions. Although the lag substantially exceeds the pulse duration, it does not exceed most phonon-polariton features reported in this thesis. We generally work with phonon-polariton frequency components less than 2 THz, so the lag, which is less than 1/4 cycle, leads only to some blurring of the sharpest features.

For the shadowgraph imaging measurements shown here, we used a probe pulse with a different center wavelength from the excitation pulse so that scattered light from the relatively intense excitation pulse can be spectrally filtered from the weak probe pulse which is recorded by a CCD camera. This is usually done by frequency-doubling of a portion of the laser output to create a probe pulse at half the center wavelength of the excitation laser pulse. Due to wavelength-dependent group velocities in $LiNbO_3$ and $LiNbO_3$, however, the frequency-doubled probe pulse propagates much more slowly than the excitation pulse, creating a "smearing" effect that seriously degrades the measurements. This problem is alleviated by steering the frequency-doubled probe pulse such that the projection of the polariton phase velocity in the

direction of the probe is equal to the group velocity of the probe pulse itself. This can only be done to velocity-match the probe with either the left-going or the right-going phonon-polariton response. The condition for velocity matching is

$$\cos\left(\frac{\pi}{2} - \theta_f + \theta_t\right) = \frac{v_{pro}}{v_{pol}}, \tag{3.22}$$

where θ_t is the angle between the probe pulse and the excitation pulse inside the crystal, and v_{pro} is the group velocity of the probe pulse. For an 800 nm excitation pulse and a 400 nm probe pulse in $LiTaO_3$, velocity matching is achieved for $\theta_t \approx 3.5^o$, which corresponds to an angle of about 8° between the two beams in air (assuming the laser excitation pulse enters the crystal with normal incidence). A schematic illustration of this smearing effect is shown in fig. 3-4. When the slower probe pulse propagates *parallel* to the faster pump pulse (black spot), the intersection between the probe beam (blue line) and the phonon-polariton response (red lines) shifts as a function of time, as can be seen in frames (a)-(c). If the probe pulse is tilted slightly to one side, however, one of the phonon-polariton responses always intersects at the same point within the probe beam, as can be seen in frames (d)-(f), where the right-travelling phonon-polariton has been velocity matched.

3.4   Control of Phonon-Polaritons via Two-Dimensional Femtosecond Pulse Shaping

Ultrafast optical control over electronic and/or vibrational responses of atoms, molecules, and crystals has advanced dramatically in recent years [6, 118, 119, 79, 7, 120, 11, 12, 14, 13]. Experiments in this field have typically been conducted using femtosecond pulse shaping techniques [24] for generation of complex excitation light fields that yield specified coherent responses or that manipulate complex phenomena such as photochemical reactions. Typically, these light fields, and the material responses generated by them, are specified as a function of time but not macroscopic spatial location. For ultrafast responses that move coherently across macroscopic distances,

99
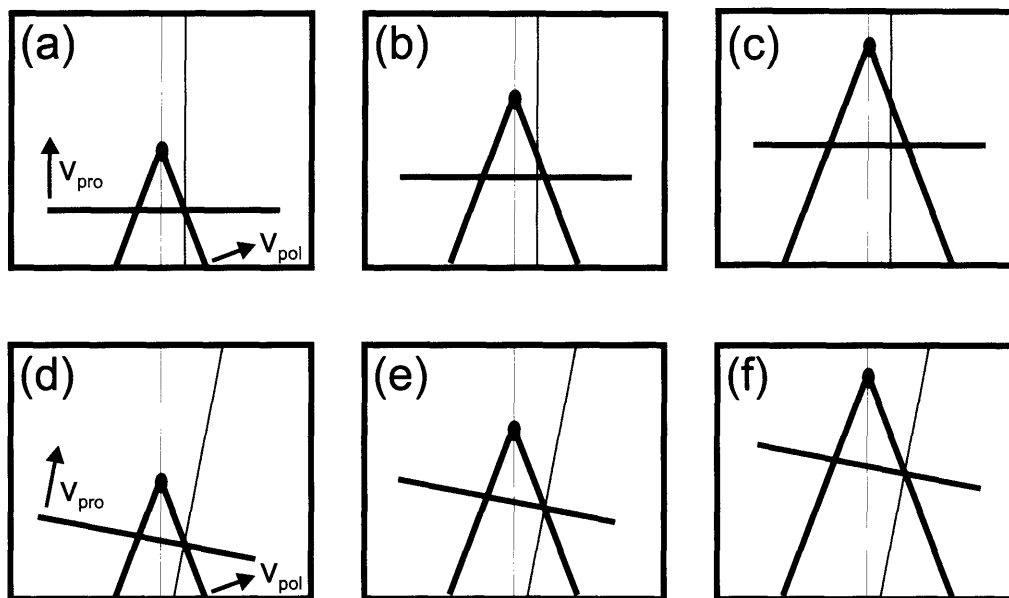
Figure 3-4: (a)-(c) Illustration of smearing effect when imaging phonon-polaritons. Here, an 800 nm pump pulse (black spot) propagating normal to the front face of the crystal generates phonon-polaritons (red lines) that travel in the direction of V_{pol}. The 400 nm probe pulse (thick blue line) travels more slowly along the thin blue line than the phonon-polariton, resulting in serious distortions of the signal. (d)-(f) Geometry for avoiding smearing distortions by tilting probe beam, such that the right-travelling phonon-polariton response always intersects the probe pulse at the same point within its beam along the thin blue line.

more complete optical control over both spatial and temporal evolution requires the use of time- and position-dependent excitation fields. Here we demonstrate versatile, programmable spatiotemporal coherent control over phonon-polaritons, with possible applications in multiplexed generation of tailored terahertz signals that could be propagated and used inside or outside the crystalline sample in which they are generated [100].

Recently developed methods in spatiotemporal femtosecond pulse shaping (described in chapter 2) were used to transform a single 800-nm pulse of 50-fs duration into an array of such pulses, arriving at different times and different locations in a lithium tantalate (LiTaO$_3$) single crystal. Vibrational waves were thereby created at multiple, programmably-specified times and points of origin such that after some propagation, the waves began to overlap and undergo constructive or destructive in-

100

terference to produce spatiotemporally controlled responses. The initial lattice vibrational amplitudes and phases at each point of origin were fully specified through spatiotemporal shaping of the optical intensity profile since the ISRS excitation process is governed by the optical intensity and not the optical phase.

Images of the propagating waves were recorded at different times by probe pulses that were variably delayed with respect to the excitation pulses. Spatiotemporal imaging [117] of phonon-polaritons in this manner is possible because of the substantial refractive index changes induced by the lattice vibrational displacements. The excitation pulses, probe pulses, and the phonon-polariton electric fields were all polarized along the optic axis of a 2-mm-thick $LiTaO_3$ crystal at 295 K. An amplified, 1-kilohertz repetition rate Ti:sapphire laser system was used, and after pulse shaping, a total of 10 to 50 μJ of energy was typically distributed among all of the excitation pulses. For all experiments, the crystals were kept at 295 K. The phonon-polaritons have frequencies in the 0.2 to 2 terahertz range, and their phase and group velocities are approximately constant at $c/6.4$ [121]. Thus, the lattice waves we generate propagate coherently at about one-sixth the speed of light in vacuum, and even single-cycle waves with THz bandwidths show negligible spreading or loss of bandwidth as they move across millimeter distances over durations of tens of picoseconds. The excitation and detection processes are illustrated schematically in fig. 3-5.

Phonon-polariton responses to excitation light fields consisting of 1, 2, 4, and 9 spots oriented along a line parallel to the $LiTaO_3$ optic axis are illustrated in fig. 3-6. Each spot received just one excitation pulse, and all of the excitation pulses arrived at the same time (t = 0). Near to the optical excitation sources, i.e., in the near field, the separate wavelets can be independently observed and monitored. After some propagation, which occurs preferentially in the direction perpendicular to the polarization, constructive and destructive interferences begin to occur among wavelets that originated from different sources. Finally, in the far field, the superposition is complete and results in a phonon-polariton wavefront whose properties are dictated by both the spatial and temporal features of the shaped optical excitation waveform. In the case of 9-pulse excitation, the near-field response is too short-lived to view
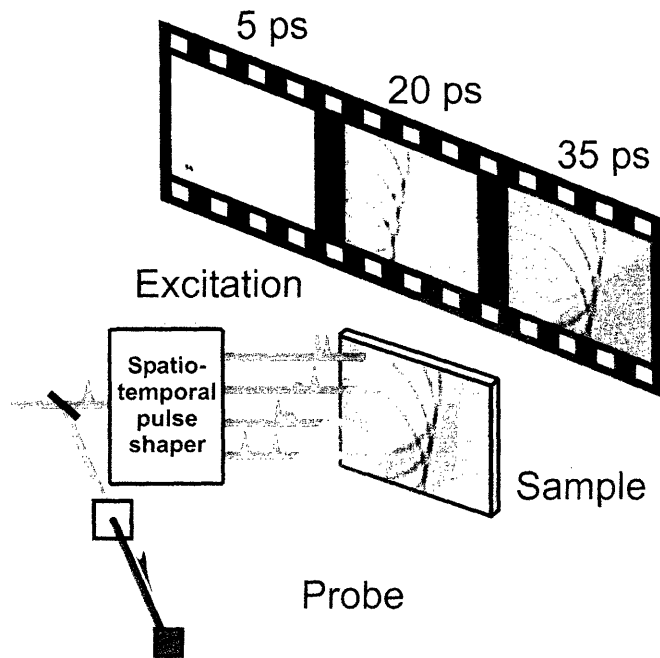
Figure 3-5: Schematic illustration of the spatiotemporal coherent control experiment. A single beam with a single femtosecond pulse is transformed by the pulse shaper into many excitation beams and pulses that reach specified sample locations at specified times. These launch lattice phonon-polariton waves that move through the sample at light-like speeds, superposing coherently to form a far-field response that is dictated by the excitation spatial and temporal profiles. Variably delayed probe pulses are passed through the sample and projected onto a CCD camera to monitor the phonon-polariton spatial and temporal evolution.

here. Experiments were conducted with up to 50 distinct excitation spots. Note that the figures consist of excerpts from far more complete sets of images which, when viewed in rapid succession, appear as "movies" of phonon-polariton propagation.

Programmable manipulation of the far-field wavefront is illustrated in fig. 3-7. By varying the times at which excitation pulses arrive at distinct spots [fig. 3-7, left], different control objectives, including wavefront tilting, focusing, and the direction of responses toward specified sample regions or "addresses," were achieved. For example, a linear delay sweep in the excitation waveform generated a phonon-polariton plane wavefront with a downward tilt [fig. 3-7 (A)], while the superposition of a linear and a parabolic delay sweep produced phonon-polaritons that focus about a millimeter away from the excitation region with either an upward or a downward tilt [fig. 3-7, (B)

102
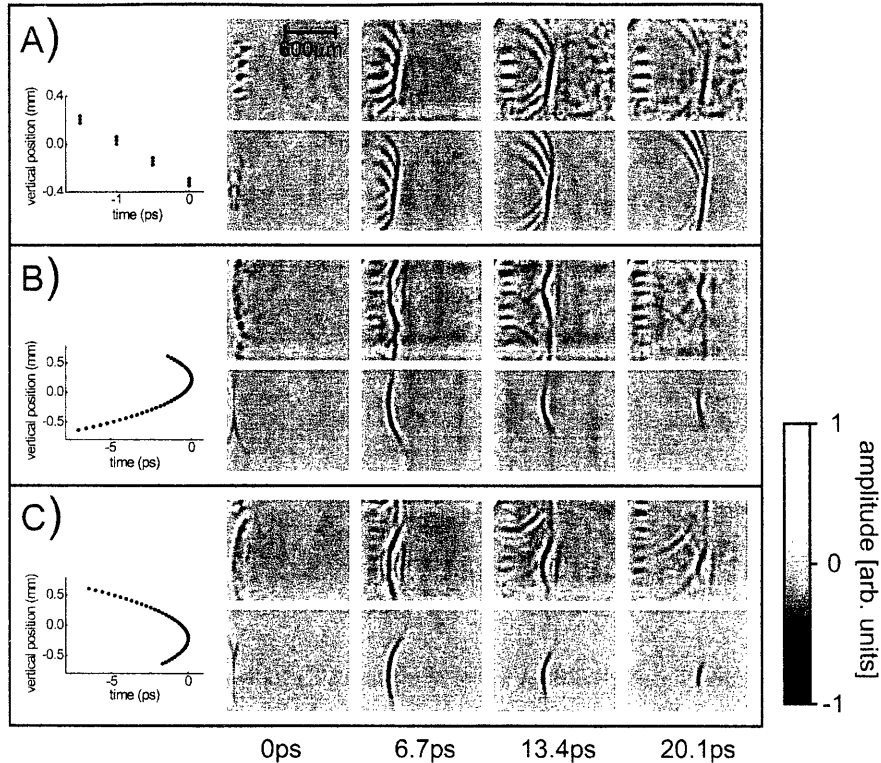
Figure 3-7: Phonon-polariton phased-array generation. Responses to excitation pulses with specified arrival times and sample locations are shown. The upper half of each row shows experimental results and the lower half shows the corresponding simulations. The inset to the left of each row illustrates the type of excitation waveform used in each case. (A) Tilted phonon-polariton wavefronts resulting from four pulses arriving at the sample at progressively later times, with a linear relation between temporal delay and spatial location of the spot. The direction of propagation depends on the slope of temporal delay vs. position in the excitation waveform. (B) and (C) Phonon-polariton focusing plus steering specified through a parabolic plus linear relation between temporal delay and spatial location of approximately 50 spots.

wavevectors. Note that some features that appear in the data of fig. 3-7 (and fig. 3-8) are due to left-propagating polaritons, polariton reflections off of various crystal faces, imperfections in the excitation waveform or the probe geometry, or photorefractive damage (which does not seem to influence the polariton generation efficiency).

Further spatiotemporal coherent control schemes allow for coherent manipulation of a propagating response by an excitation field that moves along with it through the sample. In fig. 3-8 (A), the coherent addition of phonon-polariton wavepackets as they propagate through the host crystal is demonstrated. The output of the pulse
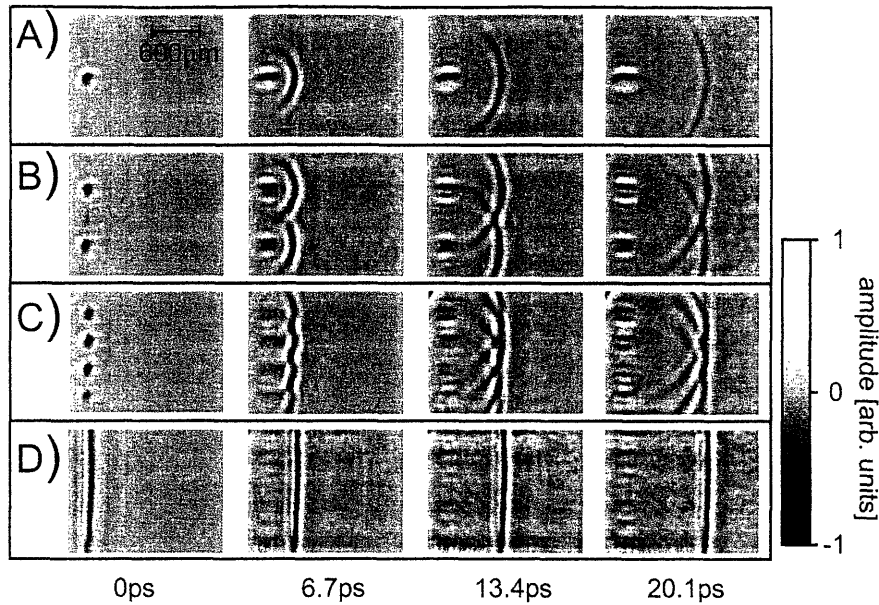
Figure 3-6: Phonon-polariton spatial coherent control. Responses to impulsive excitation with (A) one, (B) two, (C) four, and (D) nine excitation regions are shown. The time delay between successive frames is 6.7 ps. Phonon-polariton responses moving from left to right are shown. Their counterparts moving in the opposite direction are not shown.

and (C), respectively]. This type of terahertz phased-array generation is reminiscent of array sources ubiquitous in radar and ultrasound technologies [122] that operate at far lower frequencies. The single-cycle phonon-polariton responses propagate with no measurable dispersion across macroscopic distances, in excellent agreement with the simulations shown in the lower panels of fig. 3-7. Although single pulses have been used at each excitation region, multiple pulses or complex time-dependent waveforms could be used, permitting, for example, periodic excitation at each spot with the far-field wavefront manipulated through phase or frequency scanning as well as the time delay scanning illustrated here.

The simulations were performed by specifying the spatiotemporally controlled relative positions and times of origin of the separate terahertz responses, matching the initial terahertz field amplitude distribution at each region of origin to that observed experimentally, and propagating the terahertz responses in two spatial dimensions. A constant index of refraction was assumed, which is valid for low phonon-polariton

103

shaper is cylindrically focused such that each beam reaches a vertical "line" about 1 mm high and 50 μm wide at the sample. The approximately 20 beams are separated horizontally, and the time between pulses is delayed such that the pulses move from left to right across the crystal at a speed that matches the phonon-polariton group velocity. The phonon-polariton response generated by the first excitation pulse and travelling to the right is thereby amplified by successive excitation events, yielding an increase in phonon-polariton amplitude of about 10x and an intensity increase of about 100x. By comparison, the data also show left-propagating responses that originate from each excitation region and that are not amplified and appear far weaker.

A systematic scan of the delay time between adjacent excitation regions corroborates that the amplification is maximal when the group velocity of the propagating phonon-polariton wavepacket is properly matched. In fig. 3-8 (B), the maximum is found at a sweep velocity of (50 ± 10) μm/ps, which is in excellent agreement with the group velocity of 47 μm/ps for the experimentally determined central wavevector of 42 mm^{-1}. The gain as a function of the number of excitation pulses is illustrated in fig. 3-8 (C) and demonstrates that substantial terahertz wave amplification may be accomplished through spatiotemporal coherent control. In conjunction with internal or external terahertz focusing elements, the present results permit large amplitude phonon-polariton wavepacket generation. A comparable amplitude is not achievable by using just a single excitation pulse because its intensity would be well above the damage threshold of the crystal. Although the principle of constructive addition of phonon-polaritons has been demonstrated earlier with just two manually adjusted pulses [123], a previous attempt at multiple-pulse constructive addition produced barely detectable results due to an incompletely developed pulse shaping apparatus [124].

The present capabilities also point toward spectroscopic applications including the programmable steering of phonon-polaritons into integrated terahertz waveguide structures [94] for multiplexed waveguide-based terahertz spectroscopy measurements. The generation of amplified and focused, high-intensity phonon-polaritons may enable nonlinear terahertz spectroscopy and control of nonlinear lattice dynamics, an-
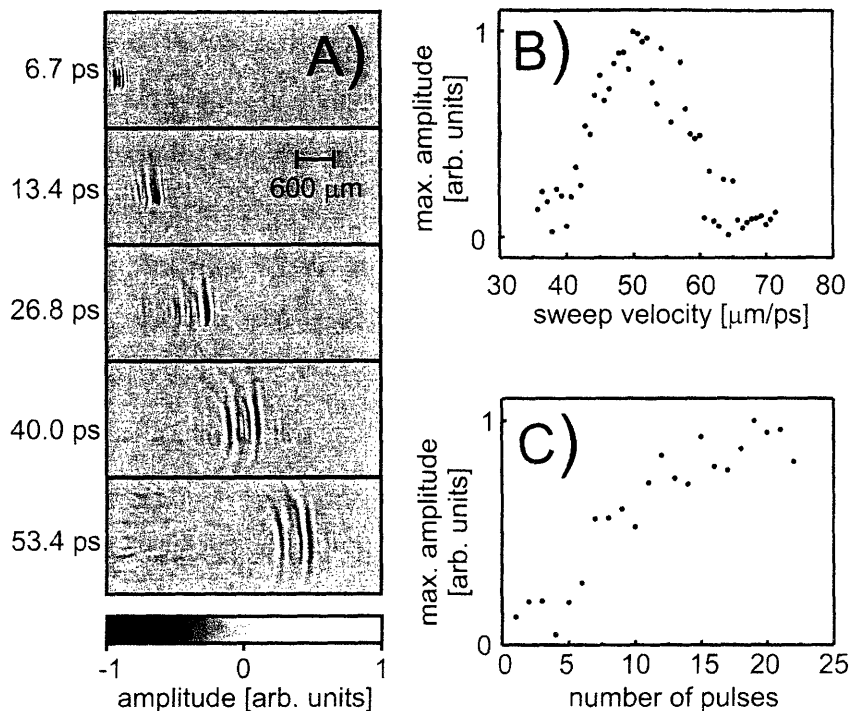
Figure 3-8: Phonon-polariton generation and amplification. (A) Amplification is realized by a series of "line" sources moving from left to right at a rate that matches the phonon-polariton group velocity. The last excitation pulse arrives before the fourth frame. Thereafter the amplified response continues moving to the right. Phonon-polariton amplification as a function of (B) the delay between two regions and (C) the number of amplifying beams.

harmonic crystals near structural phase transitions, or liquid-state intermolecular dynamics [96].

3.5 Improved, Echelon-Based Phonon-Polariton Amplification

A long-standing goal of the Nelson group has been to generate and observe large displacements in ionic crystals in order to determine anharmonic contributions to the potential energy surface. For the class of materials known as ferroelectrics [18], which are ionic crystals possessing a permanent electric dipole within the unit cell, these anharmonic components of the potential-energy surface give rise to a number of

properties of great technological importance. For instance, ferroelectric materials are widely used as piezoelectric transducers and actuators, insulators in high dielectric constant capacitors, ferroelectric random access memory (FRAM) in computers, and they are promising candidates for large-scale (many megabytes or larger) non-volatile random access memory devices widely anticipated in the computer industry. Although non-parabolic potential energy contributions have been modelled theoretically [19], there has only been one report in the literature (to the best of our knowledge) which has measured properties related to the nonlinear lattice potential in the THz frequency range [102]. This frequency range is of particular interest since the vibrational modes in many cases correspond to modes along the known non-parabolic potential energy surface.

The dearth of measurements of the nonlinear contributions to the potential energy surface for ferroelectrics at THz frequencies is largely due to the lack of good sources of high-intensity coherent THz radiation. In this section, we will demonstrate an improved method for generating large-amplitude phonon-polariton amplitudes based on the travelling-wave amplification scheme described in section 3.4. These large amplitude phonon-polariton waves may be used to probe the lattice potential of the host crystal in which they are generated, or the large THz electromagnetic component may be coupled out of the generation crystal for use with other materials.

As described above, a single excitation pulse may be only used to generate phonon-polaritons of a certain maximum amplitude without causing irreversible damage to the generation crystal (i.e. ablation of the crystal). Multiple, spatially separated excitation pulses allow for a "gentler" means to create very large amplitude phonon-polaritons, as shown in section 3.4. In order to create the largest possible phonon-polariton amplitudes using the distributed addition scheme, then, the individual pulses should each be as close to the permanent damage threshold as is possible. Although the pulse-shaping approach did allow for generation of phonon-polaritons larger than is possible with a single laser excitation pulse, none of the individual pulses within the excitation waveform was near to the crystal damage threshold. This was partly due to the efficiency of the pulse shaping apparatus itself, and limited in part

by grating efficiency. Additionally, the damage threshold of the liquid crystal spatial light modulator (LC SLM) itself placed a limit on the largest input pulse that can be used.
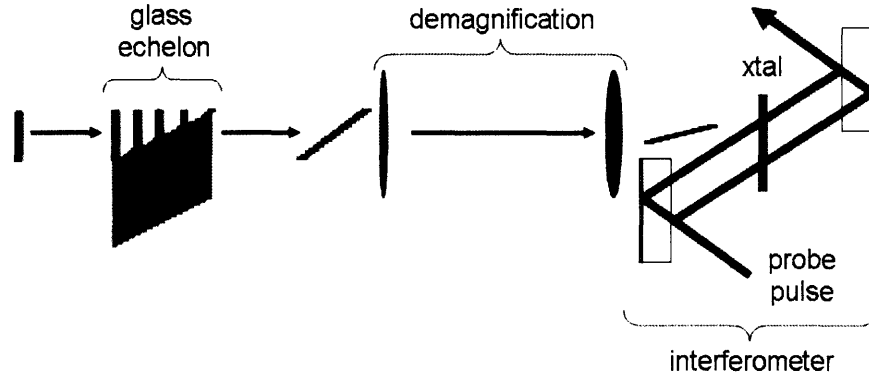
Figure 3-9: Echelon-based scheme for creating large amplitude phonon-polaritons.

In order to extend the phonon-polariton amplification scheme described in section 3.4 to be able to generate very large amplitude phonon-polaritons, we used refractive delays imparted by a glass echelon to create a series of pulses distributed in space and time, as shown in fig. 3-9. The echelon itself consists of stack of 40 anti-reflection coated glass substrates arranged in a step-like structure, where each substrate is approximately 0.375 mm thick. The echelon therefore delays the pulse within different regions of the laser beam by varying amounts, producing the same type of waveform used for phonon-polariton amplification in section 3.4. Demagnification of the beam transmitted by the glass echelon was then used to decrease the spatial separation of consecutive excitation spots to the appropriate size for generating the very large phonon-polariton amplitudes. Since the glass substrates have a much higher damage threshold than the LC SLM used in section 3.4, this apparatus may be used with more intense input laser pulses than is possible with the LC SLM apparatus. Note that the relatively simple imaging interferometer shown in fig. 3-9, a variation on a Jamin interferometer [125], contains only two mirrors and is passively phase-stabilized since both arms of the interferometer propagate through the same set of optics. Ordinary aluminum-coated mirrors on 0.375 inch glass substrates were used, and they were oriented with the uncoated surface facing the probe beam as

indicated. The probe wavelength here was 400 nm, and the probe pulse was velocity-matched by tilting it at an angle in to avoid smearing in the measurement of the amplified phonon-polariton response.
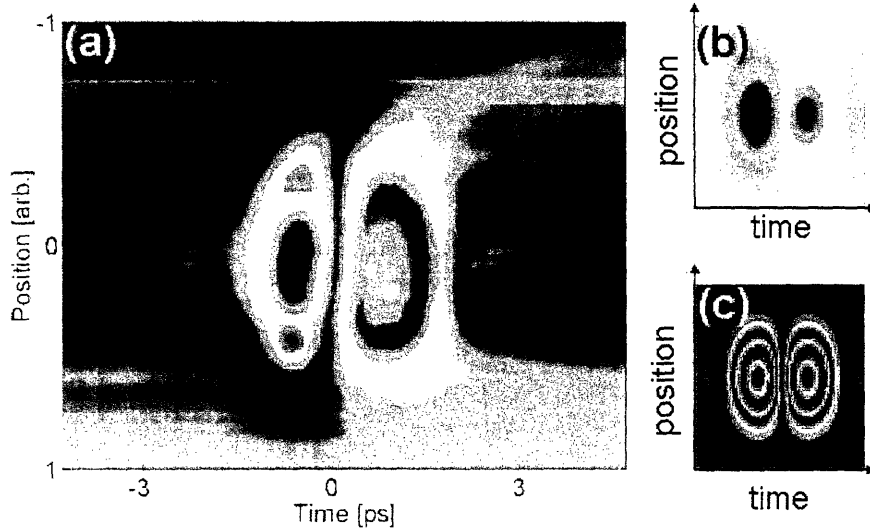
Figure 3-10: (a) Interferometric measurement of a large-amplitude phonon-polariton single-cycle wave generated with an echelon-based pulse shaping scheme. (b) Actual shape of the phonon-polariton field. (c) Simulation of the effects of interferometric measurement of a large-amplitude phonon-polariton, leading to a concentric-ring type structure observed in (a).

Fig. 3-10 (a) shows a measurement of a large-amplitude phonon-polariton wave as it passes by a vertical line within the crystal. Due to the large amplitude of the phonon-polariton, the phase shift imparted to the signal arm of the probe interferometer (relative to the reference arm of the probe interferometer) exceeded 2π, creating the unusual ring-like shapes shown in (a). The actual phonon-polariton field more resembles that shown in (b), which consists of a single negative and a single positive lobe (a single cycle pulse). The peak field of the phonon-polariton created a phase shift of approximately 2.5π. Since signal from interferometry is proportional to the cosine of the phase difference between the two arms of the interferometer, the maximum intensity observed corresponds to a phase shift of π. For reference, a simulation of the intensity for a phonon-polariton with a peak field sufficient to create a phase shift of 3π. Due to the difficulty in determining the exact phase shift imparted at the peak of the phonon-polariton field, we have placed a lower bound on its value of

109

15 KV/cm.

The above measurements were made with a laser excitation pulse of 1.5 mJ energy. Subsequent to the measurements shown here, other members of the group rebuilt the apparatus such that greater than 50 kV/cm THz fields were generated. Even larger fields should be obtainable by using 4 mJ laser pulses that are now available. Experiments aimed at measurements of the non-parabolic character of the potential energy surface using these very large THz fields are now underway. More broadly, time-resolved measurements using THz "excitation" fields of large amplitude will be made using variably delayed THz and visible probe pulses. Wide-ranging applications of THz nonlinear optics and spectroscopy are anticipated.

3.6 Typesetting THz waveforms

For many fundamental and practical reasons, the linear spectral filtering approach that is well established in the optical regime for femtosecond pulse shaping (discussed in chapter 2) is not easily adapted to the THz regime. Instead, the THz pulse shaping methods reported to date have utilized either temporally shaped femtosecond excitation waveforms [126, 127, 128, 129] or specially fabricated materials or devices, with limited results in terms of the complexity and fidelity of the THz waveforms generated [130, 131, 132].

In this section we describe a new phonon-polariton-based method for generating tailored terahertz waveforms by shaping the spatial profile of the excitation pulses used to generate them. Since phonon-polaritons propagate in a plane almost perpendicular to the direction of the excitation beam (see fig. 3-3), the spatial profile of the femtosecond laser pulse exerts a strong influence on the temporal profile of the generated phonon-polariton response. As the phonon-polariton wave intercepts the crystal-air interface, the electromagnetic component, imprinted with the specified THz waveform, is able to radiate out into air and may be used for further experiments or applications.

It can be shown analytically in one dimension that in the impulsive, plane wave

excitation limit, the observed THz waveform $E(x,t)$ resembles the spatial derivative [133, 134] of the excitation beam profile $I_{exc}(x)$

$$E\left(x \pm \frac{ct}{n}, t\right) \propto \pm\partial_x I_{exc}(x), \qquad (3.23)$$

where c is the speed of light in vacuum and n is the THz frequency index of refraction which is nearly constant at frequencies well below the phonon resonance. Therefore, the spatial excitation profile that is needed to produce a user-defined THz waveform is to a first approximation calculated by integration. For higher frequencies it is necessary to back-propagate the THz waveform from the probe region to the excitation region prior to integration, and thus to compensate for dispersion and absorption effects. This is straightforward, so in both cases there exists a relatively easy recipe to determine the necessary spatially varying excitation profile. The next step is to simply 'typewrite' that excitation profile onto the crystal by shaping the spatial profile of the excitation pulse. The THz waveforms may be optimized through feedback-controlled adaptive shaping of the spatial excitation beam, although this technique was not implemented here.
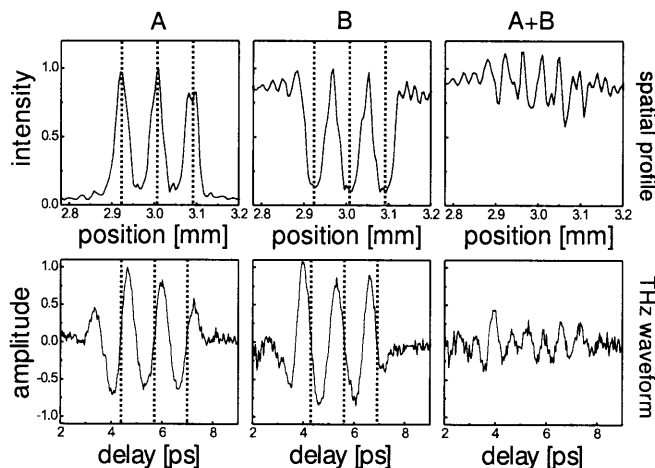
Figure 3-11: Two complementary excitation profiles a) and b) whose sum is spatially uniform c), and the corresponding measured THz waveforms d) and e) whose sum is uniformly zero f).

An example is shown in fig. 3-11. Note that the excitation profiles (a) and (c) are complementary, i.e. they add up to a constant value $I_1(x) + I_2(x) = $ const. as

seen in fig. 3-11(e). If the THz waveform is proportional to the spatial derivative, it is easy to show that $\partial_x I_2(x) = -\partial_x I_1(x) = \exp(i\pi)I_1(x)$. This argument also holds for higher frequencies because the frequency spectrum and dispersive or absorptive effects are identical for the two waveforms. Figures 3-11(b) and (d) show the measured waveforms. As expected they are out of phase by π and add up to zero as seen in fig. 3-11(f).

The laser pulses used to excite phonon-polaritons had a central wavelength of 790 nm, a duration of 40 fs, a repetition rate of 1 kHz, and 10–100 μJ of energy. A computer-controlled spatial light modulator (see chapter 2) was used to generate user-defined one-dimensional excitation profiles trhough amplitude modulation of the incident pump beam. The SLM was operated in amplitude-modulation mode, in which the nematic liquid crystal layer of the SLM was aligned such that it variably rotated the polarization of the pump beam at different spatial locations. This spatially varying polarization was converted to an amplitude modulated beam with a polarizer, and then imaged onto a 4 mm by 10 mm large and 0.5 mm thick x-cut $LiNbO_3$ crystal. In all cases, the polarization of the excitation beam at the sample was parallel to the optic axis, which is oriented vertically in figure 3-12. The excitation profiles varied along the x-direction (a cross section of the excitation intensity along the x-direction is shown in each figure) but were constant along the y-direction, typically over a few millimeters. A charge-coupled device camera was used to record the spatial excitation profile of all THz waveforms generated.

Phonon-polaritons were detected by measuring the transient birefringence induced in variably delayed probe pulses (see fig. 3-12). Lock-in detection was used to help eliminate noise arising from scattered light. The time needed for data acquisition was typically on the order of several minutes. Note that the spatial resolution (FWHM of the probe beam) was (13 ± 2) μm and the probe beam was variably delayed to measure the time-dependent index variation at a spatial position well separated from the excitation region (see figure 3-12). The size of the probe beam was chosen such that the highest polariton frequencies expected could be measured accurately, i.e. the probe spot was small compared to the finest features of the spatially varying
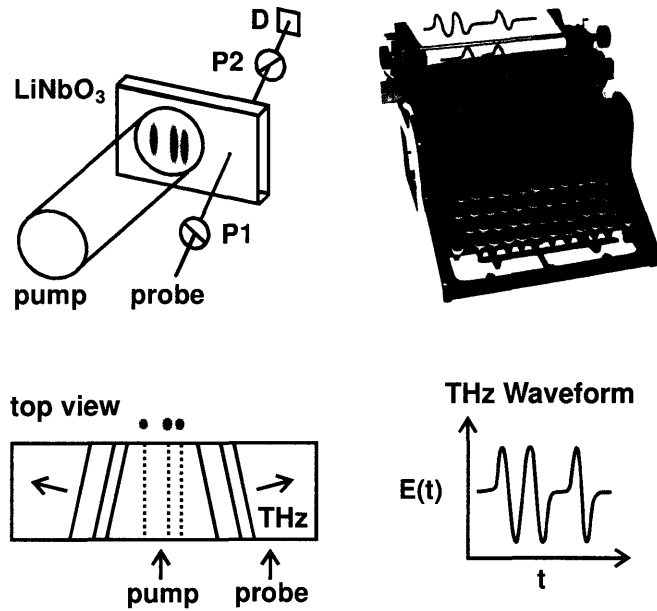
Figure 3-12: Experimental setup for the generation and detection of shaped THz waveforms.

excitation profile. Coherent detection allowed us to measure the THz electric field rather than its intensity, yielding phase as well as amplitude information.

Figure 3-13 shows negatively chirped, unchirped, and positively chirped phonon-polariton responses. The excitation profiles in column 3-13(a) show that the spacing between adjacent peaks is nonuniform in the top and the bottom rows but constant in the middle row. Column 3-13(b) shows that the spatial excitation profile is translated into the corresponding phonon-polariton waveform and that the uniform/nonuniform excitation profiles lead to unchirped/chirped phonon-polariton waveforms. The windowed Fourier transforms of the waveforms in column 3-13(b) are shown in column 3-13(c). Here, the chirp manifests itself in an upward or downward tilt of the time-frequency distribution. Note that the unchirped and the chirped waveforms have the same overall temporal duration. Since the chirped waveform may in principle be compressed, through removal of any nonuniform spectral phase, its bandwidth-limited duration would be shorter than its original duration. To support the shorter duration, the chirped waveforms require a larger spectral bandwidth, as seen in column 3-13(c). The maximum spectral bandwidth corresponds to the narrowest feature

113
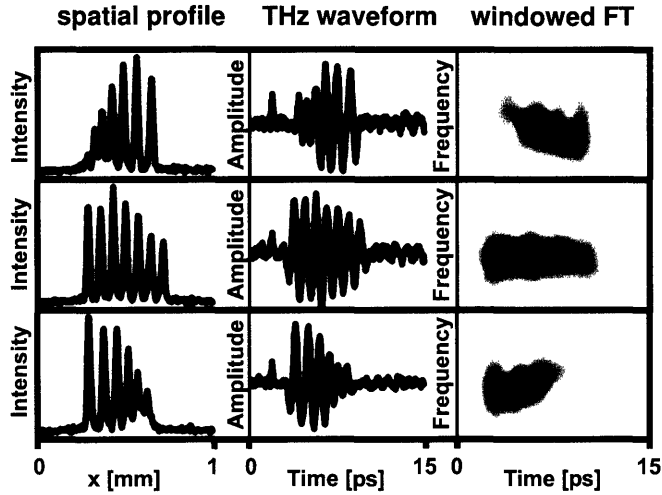
Figure 3-13: Unchirped and chirped THz waveforms. The excitation pattern is shown in column (a), the measured THz waveform in column (b), and the windowed Fourier transform in column (c).

of the excitation profile.

To demonstrate that the present technique is suitable for encoding signals in THz waveforms, we have generated spatially varying excitation profiles that are able to imprint a waveform resembling one byte worth of information. The bits are equally spaced, and each bit in the THz waveforms is represented by a single-cycle pulse generated by a single Gaussian shaped "line" feature within the excitation profile. The spatial light modulator allows single bits to be switched on or off in a simple manner. A compilation of nine consecutive experiments is shown in figure 3-14. An intensity plot of a vertical section of the excitation profile together with the corresponding byte is displayed in figure 3-14(a), and the measured phonon-polariton responses are shown in figure 3-14(b). Each excitation line generates a single-cycle response which corresponds to a single 'bit'. The center frequency of a single 'bit' is 1.1 THz and the bandwidth around 1 THz.

The decay of the signals in figure 3-14(b) is due primarily to the fact that the phonon-polaritons propagate across the crystal with a small forward wave vector component.[88] When they reach the back of the crystal, they reflect forward, and at this point the probing is no longer phase matched. This effect can be eliminated either by tilting the crystal with respect to the excitation beam angle of incidence

114
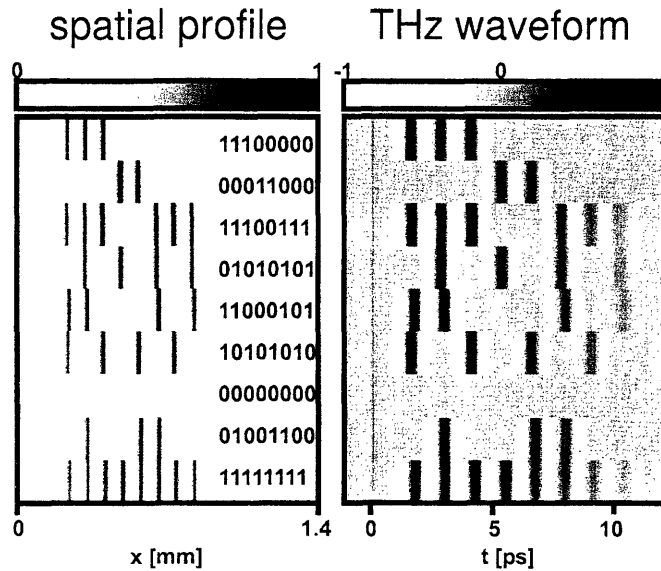
Figure 3-14: Generation of THz waveforms representing a byte. (a) Intensity plot of a vertical section of the excitation profile as a function of the spatial position together with the corresponding number in binary coding. (b) measured THz waveform versus probe delay time. The narrow dark line at time zero in (b) is caused by an instantaneous electronic contribution to the Kerr signal.

[135] or by using a crystal with the back side cut at an angle that matches the forward propagation component (26 degrees in $LiNbO_3$) so that polariton propagation is parallel to the back side. Polariton damping can be reduced substantially through cooling of the crystal to 77 K [136], or alternatively, it may be accounted for by an appropriate modification of the excitation beam profile. Finally, coupling of THz radiation out of the crystal may be optimized by cutting the side of the crystal to be perpendicular to the phonon-polariton propagation direction and/or through use of an index-matching medium.

Although the above examples of terahertz pulse shaping have been limited to shaping the temporal characteristics of the generated phonon-polariton through shaping of the excitation field in one spatial dimension, it is straightforward to extend these methods into two dimensions. In fig. 3-15, two-dimensionally shaped spatial excitation patterns (created with Fourier-beam shaping methods discussed in section 2.6) have been used to create spatiotemporally shaped phonon-polariton waveforms. Shadowgraph imaging was used to monitor the phonon-polariton waveforms as they prop-
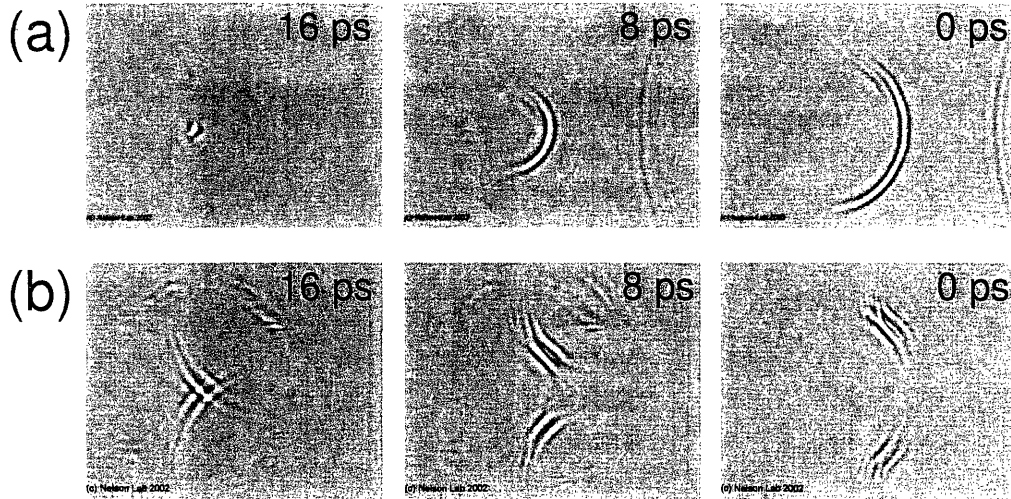
Figure 3-15: Generation of two-dimensionally shaped terahertz waveforms. Each panel is roughly 2.5 mm (wide) by 2 mm (tall).

agate. In (a), the excitation beam profile was that of a semi-circle, resulting in a phonon-polariton with a curved wavefront that focuses as it propagates. In (b), the excitation beam profile was two pairs of lines that cross after propagating roughly 0.8 mm. Prior experiments have required multiple static optical elements to create phonon-polariton waveforms with specific properties: spherical lenses (spot excitation) [117]; cylindrical lenses (line excitation); transmission gratings (multiple-fringe excitations) [123, 121]; axicon-lens arrangement (ring excitation) [137]. Instead, these as well as more arbitrary spatial excitation profiles may be simply generated through Fourier beam-shaping methods, in order to generate phonon-polariton waveforms as desired for experiments.

In conclusion, we have demonstrated in this section that spatial shaping of femtosecond excitation pulses leads to well defined THz phonon-polariton waveforms in $LiNbO_3$. The method requires no specialized materials or techniques other than a commonplace electrooptic crystal and the ability to create spatially shaped beam profiles. By coupling the generated THz radiation into free space, the corresponding THz electromagnetic field can be used for further experiments or applications.

In this chapter, we have demonstrated versatile spatial and/or temporal coherent control over propagating modes. While the present measurements have been con-

116

ducted exclusively on phonon-polaritons, other propagating modes including exciton-polaritons and spin waves could also be excited and controlled in a similar manner. We note that although phonon-polariton excitation through ISRS does not require control over the optical phases of different excitation pulses, the phases are well defined and to a considerable extent can be controlled, as described in the previous chapter. Polarization specification also could be exploited in coherent control over various systems, including spin waves [10].

Chapter 4

Coherent Four-Wave Mixing Spectroscopy Based On Two-Dimensional Femtosecond Pulse Shaping

4.1   Introduction

Nonlinear spectroscopic methods have been widely applied over the past several decades to diverse problems of both fundamental and applied importance. From two-dimensional (2D) nuclear magnetic resonance (NMR) spectroscopy [4] widely used in determining solution-phase structures of complex biomolecules, to real-time observations of chemical reactions [138], to Angstrom-level measurements of thin films probed with laser-generated acoustic waves [139], nonlinear spectroscopic methods can provide a vast amount of information about, for instance, a system's structural properties, relaxation processes, interactions with its surroundings, or dynamics when undergoing change. In addition to their ability to access nonequilibrium states of a system, nonlinear spectroscopic methods derive much of their usefulness from their ability to selectively measure properties of interest that are not clearly observable in

linear measurements. This is especially the case for condensed-phase measurements where complex inter- or intramolecular interactions, possibly occurring on time-scales faster than the measurement itself, broaden spectral lines in linear absorption measurements and obscure the desired information content of the spectrum. Consider a molecule of interest dissolved in a polar solvent such as water. The solvent molecules organize around the molecule of interest in a multitude of configurations that fluctuate over a large range of timescales, creating a variety of local solvation environments that change during the course of the measurement. The resulting absorption spectrum may then be very broad due in part to the large, inhomogeneous distribution of local solvation environments surrounding the molecule of interest. While the linear absorption spectra do in principle contain information about, for example, the homogeneous and inhomogeneous linewidths, the two are inextricably convolved with each other.

Nonlinear spectroscopic methods are often able to peer beneath broad, congested linear absorption spectra, to isolate quantities of interest. In the case of 2D NMR, methods such as correlation spectroscopy (COSY) or nuclear Overhauser effect spectroscopy (NOESY) can be used to spread spectra along two dimensions to reveal spin-couplings between adjacent or nearby nuclei. These and other related methods in NMR have been so successful that scientists have long sought to develop analogous experimental techniques in vibrational and electronic spectroscopy. The field of two-dimensional vibrational spectroscopy, especially, has made great progress in recent years [140, 141, 3, 20]. To date, two-dimensional vibrational spectroscopy been applied to a wide variety of interesting problems, including, the determination of anharmonicities and vibrational couplings within small molecules [142], the examination of the ultrafast timescales of hydrogen bonding in liquid water [143, 144], and the study of protein folding [5]. Analogous two-dimensional *optical* spectroscopic methods that probe electronic resonances have achieved more limited success, largely due to technical difficulties with the available experimental tools [20, 145, 146, 147].

Figure 4-1 schematically illustrates a typical experimental apparatus used for 2D optical (or infrared) spectroscopy. A single, short input pulse is divided up into four

120

pulses with a series of beamsplitters. Three of the pulses (black lines) are focused to a common point within the sample to generate a nonlinear signal in the direction of the detector, and a fourth (reference) pulse (shown in blue) is overlapped with the signal to characterize the signal via spectral interferometry. The signal is recorded as a function of one or more of the pulse delays, and this data is then Fourier-transformed to yield a 2D spectrum. Foremost among the challenges with this approach is that the signal is interferometrically detected. Since the phase of the emitted signal is a function of the phases of the input beams, it is important that the relative path lengths within all beams do not fluctuate by more than a small fraction of the wavelength. In the case of infrared vibrational experiments, where the wavelengths are on the order of 3-6 um, such an apparatus can be made to be reasonably insensitive to vibrations or other possible path length variations during the course of the measurements. For optical multidimensional spectroscopy, where the wavelengths are typically in the range of 0.4-0.8 um, the path length variations are much more problematic.
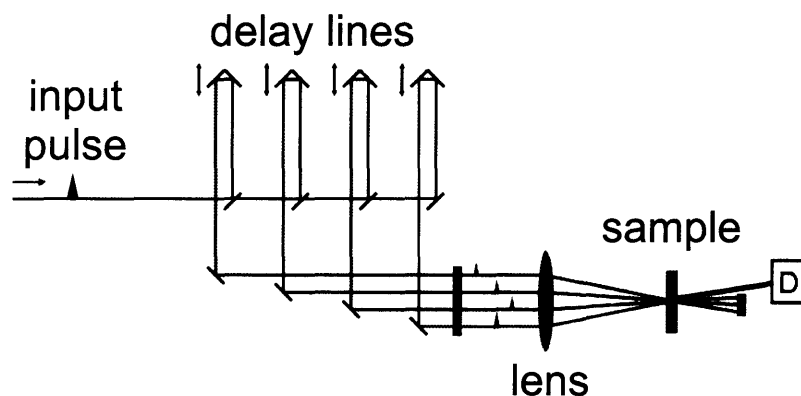
Figure 4-1: Schematic illustration of experimental apparatus used for 2D optical and infrared spectroscopy. A single input pulse is split into four pulses. Three of these pulses (black lines) may be variably delayed before they are focused to a common point within a sample and generate a nonlinear signal in the direction of the detector D. The fourth pulse (blue line) is interferometrically combined with the signal in the direction of the detector in order to characterize the signal.

Beyond differences in the mechanical stability of 2D optical and infrared spectroscopies, there is a broader issue that both optical and infrared 2D spectroscopy face, and that is the limited ability to which the input pulses may be shaped. In fact, the only control afforded by the method is the arrival time of the pulses used

to generate the nonlinear response. This is in contrast to 2D NMR, where sophisticated radio-frequency pulse sequences with specified frequencies, timings, and phase relationships between the pulses are the foundation upon which the 2D methods are based. Incorporating separate pulse shaping apparatuses (see chapter 2) into the individual beams of 2D optical infrared spectroscopy is no easy task, though, especially considering the difficulties of maintaining interferometric phase stability.

In this chapter we will discuss a powerful new approach to 2D (or generally, multidimensional) optical spectroscopy that is based on the 2D pulse shaping methods discussed in chapter 2. We will show how our pulse shaping based approach eliminates the problems of mechanical stability between the different beams and at the same time opens up many exciting new possibilities. The chapter will begin with an overview of the theoretical background for nonlinear spectroscopy and will make use of the simple approach of diagrammatic perturbation theory [21]. Next, the experimental apparatus will be described and its capabilities will be elaborated. Finally, results on three prototype systems will be used to illustrate the exciting possibilities with this powerful new method.

4.2   Nonlinear Optical Response

Four-wave mixing spectroscopic methods are based on the mixing of three input light fields, defined here as $\mathbf{E}_a$, $\mathbf{E}_b$, $\mathbf{E}_c$, to generate a fourth light field (the signal) $\mathbf{E}_s$, usually in a unique direction. In the present case, the three input fields as well as the output field are degenerate, or nearly so, meaning their center frequencies are close together, giving the method its full name degenerate four-wave mixing (DFWM). The input fields may be written in a general form as

$$\mathbf{E}_n(\mathbf{r}, t) = E_n(t) \exp\left[i\left(\mathbf{k}_n\mathbf{r} - \omega_n t + \phi_n(t)\right)\right] + \text{c.c.}, \qquad (4.1)$$

where $\mathbf{r}$ is the spatial coordinate, where the nth field has the slowly-varying envelope $E_n(t)$, wavevector $\mathbf{k}_n$, carrier frequency ω_n, time-dependent phase (such as for a shaped pulse, or when using multiple phase-related pulses) $\phi_n(t)$, and where c.c.

indicates complex conjugate such that the input fields are real. All fields are considered to be linearly polarized along a common axis, which is sufficient for the analysis and measurements in this chapter. Note that boldface terms indicate vectorial quantities. A commonly used beam arrangement for DFWM spectroscopy is the *boxcars* geometry, where three input fields, $\mathbf{E}_a$, $\mathbf{E}_b$, and $\mathbf{E}_c$, originating from three corners of an imaginary box, are focused to a common point within a sample, producing a signal output field $\mathbf{E}_s$ in the direction of the fourth corner of the box, as shown in fig. 4-2. Although in fig. 4-2 (left) double-sided arrows are used to indicate that the timing of the input pulses may be varied, other parameters may be adjusted during measurements, such as the center frequency or the phase of a given pulse.

boxcars FWM geometry   outgoing beams
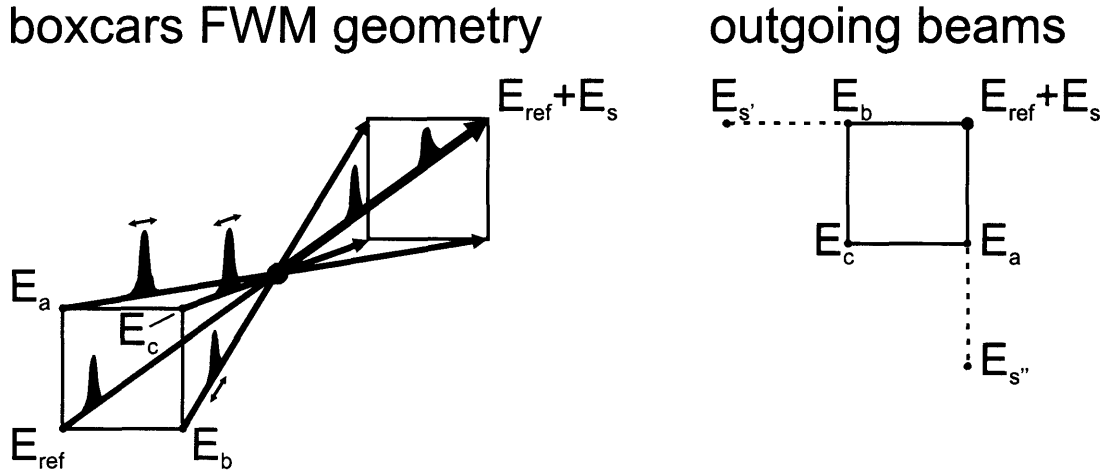
Figure 4-2: (left) Boxcars beam geometry for DFWM spectroscopy. (right) Output DFWM fields are generated in three directions, labelled as beams $\mathbf{E}_s$, $\mathbf{E}_{s'}$, and $\mathbf{E}_{s''}$.

The third-order macroscopic polarization response $\mathbf{P}^{(3)}(\mathbf{r}, \omega)$ resulting from three incident fields is given by

$$\mathbf{P}^{(3)}(\mathbf{r}, t) = \overline{\overline{\chi}}^{(3)} \sum_{f,g,h} \mathbf{E}_f(\mathbf{r}, t)\mathbf{E}_g(\mathbf{r}, t)\mathbf{E}_h(\mathbf{r}, t), \qquad (4.2)$$

where $\overline{\overline{\chi}}^{(3)}$ is the third order dielectric susceptibility tensor, and where the summation is performed over all possible combinations of the three incident fields. Of the 27 terms that result from the evaluation of eq. 4.2, only 6 are dependent upon all three of the incident fields—these can be distinguished from the rest by their wavevector. It will be

discussed in section 4.5.2 how these 6 terms correspond to six possible time-orderings of the three interactions between the sample and the input fields. Considering just one of these 6 terms, multiple output beams are generated, as shown in eq. 4.3.

$$\mathbf{P}^{(3)}(\mathbf{r}, t) = \overline{\overline{\chi}}^{(3)} \mathbf{E}_a(\mathbf{r}, t) \mathbf{E}_b(\mathbf{r}, t) \mathbf{E}_c(\mathbf{r}, t) \qquad (4.3)$$

$$= \overline{\overline{\chi}}^{(3)} \left\{ E_a(t) E_b(t) E_c(t) e^{i((-\mathbf{k}_a + \mathbf{k}_b + \mathbf{k}_c)\mathbf{r} - (-\omega_a + \omega_b + \omega_c)t - \phi_a(t) + \phi_b(t) + \phi_c(t))} \right.$$

$$+ E_a(t) E_b(t) E_c(t) e^{i((\mathbf{k}_a - \mathbf{k}_b + \mathbf{k}_c)\mathbf{r} - (\omega_a - \omega_b + \omega_c)t + \phi_a(t) - \phi_b(t) + \phi_c(t))}$$

$$+ E_a(t) E_b(t) E_c(t) e^{i((\mathbf{k}_a + \mathbf{k}_b - \mathbf{k}_c)\mathbf{r} - (\omega_a + \omega_b - \omega_c)t + \phi_a(t) + \phi_b(t) - \phi_c(t))}$$

$$\left. + E_a(t) E_b(t) E_c(t) e^{i((\mathbf{k}_a + \mathbf{k}_b + \mathbf{k}_c)\mathbf{r} - (\omega_a + \omega_b + \omega_c)t + \phi_a(t) + \phi_b(t) + \phi_c(t))} + \text{c.c.} \right\}$$

In eq. 4.3, the polarization response to the three input beams produces *four* separate output beams that propagate in different directions, as can be seen by examining the wavevector of each of the four terms. For example, the last term propagates with a wavevector $\mathbf{k}_a + \mathbf{k}_b + \mathbf{k}_c$, which for the boxcars geometry, corresponds to a beam propagating in the direction of beam $\mathbf{E}_c$. The other three terms propagate in directions different from the three input fields, and these terms (labelled $\mathbf{E}_s$, $\mathbf{E}_{s'}$, and $\mathbf{E}_{s''}$ in fig. 4-2, right) constitute the degenerate four-wave mixing (DFWM) polarization response. Use of the term "degenerate" in DFWM implies that the three input fields as well as the output fields all have the same, or nearly the same, frequency, which is the case here. The output field in the direction of $\mathbf{E}_c$ has a frequency that is the sum of all the input frequencies. It is not a *degenerate* signal and will therefore be ignored for the remainder of the chapter.

It is important to note that each of the three output DFWM light fields in eq. 4.3 has a different frequency, wavevector, and phase dependence on the three incident fields. The input field whose frequency, wavevector, and phase relationship to the output field is opposite to that of the other two input fields is called the *conjugate field*. For instance, the third term has a wavevector given by $\mathbf{k}_a + \mathbf{k}_b - \mathbf{k}_c$, which indicates that $\mathbf{E}_c$ is the conjugate field. When using the boxcars geometry, the signal that propagates in the direction of the fourth corner of the box is perfectly phase-

matched [114]. Because of this, the signal at the fourth corner of the box is in general the strongest, although the extent to which the other two signals are weaker due to improper phase-matching depends upon the specifics of the refractive index (and thickness) of the sample. Additionally, the three output signal fields contain, in general, different information about the sample response. It will be discussed in the section 4.3, that when short, non-overlapping pulses are used for the three input fields, the timing of the conjugate field relative to the other two input fields selects which one of the three different responses that will propagate in the direction of the fourth corner of the box.

4.3 Time-Dependent Perturbation Theory of Degenerate Four-Wave Mixing

One crucial aspect of the polarization response not elaborated in eq. 4.3 was the detailed form of the third order nonlinear optical susceptibility, $\overline{\overline{\chi}}^{(3)}$. In this section, we will use semiclassical perturbation theory [148, 21], where the light fields are treated classically but the system is treated quantum mechanically, to derive general expressions for the macroscopic polarization response. After that, we will explicitly calculate the first-order polarization response for a two-level system in order to demonstrate the use of the formalism. Then, a related diagrammatic approach will be used to calculate photon echo and transient grating signals (two classes of DFWM processes) for a two level system. Finally, we will discuss the features of measurements of systems with more levels.

In time-dependent perturbation theory, it is customary to split the Hamiltonian of the system, H(t), into two parts, H_o which describes the system in the absence of applied fields, and V(t) which describes the influence of the incident electric fields on the system:

$$H(t) = H_o + V(t) \qquad (4.4)$$

The time-dependent portion of the Hamiltonian is given by

$$V(t) = -\left(\mathbf{E}_a(\mathbf{r}, t) + \mathbf{E}_b(\mathbf{r}, t) + \mathbf{E}_c(\mathbf{r}, t)\right) \cdot \mu, \tag{4.5}$$

where μ is the transition dipole operator that describes the coupling of the states of the system resulting from an incident electric field. Note that vectorial notation (boldface variables) is used for the fields and material polarization in order to keep track of the different directions in which polarizations may be emitted, but that the spatial dependence of μ (implied by the dot product in eq. 4.5) will be ignored.

Working in the interaction picture (see chapter 5 of reference [148] or chapter 2 of reference [21], for example), we can write the Liouville-von Neumann equation of motion:

$$\frac{\partial \rho_I(t)}{\partial t} = -\frac{i}{\hbar} \left[V_I(t), \rho_I(t)\right], \tag{4.6}$$

where $\rho_I(t)$ is the interaction picture density matrix and $V_I(t)$ is the interaction picture time-dependent Hamiltonian corresponding to V(t). Following the usual procedure of integrating eq. 4.6 and then iteratively substituting it into itself [21], we obtain expressions for the interaction picture density matrix up through third order:

$$\rho_I^{(1)}(t_1) = \left(\frac{-i}{\hbar}\right)^2 \int_0^{t_1} dt_0 \left[V_I(t_0), \rho_I(t_0)\right] \tag{4.7}$$

$$\rho_I^{(2)}(t_2) = \left(\frac{-i}{\hbar}\right)^2 \int_0^{t_2} dt_1 \int_0^{t_1} dt_0 \left[V_I(t_1), [V_I(t_0), \rho_I(t_0)]\right] \tag{4.8}$$

$$\rho_I^{(3)}(t_3) = \left(\frac{-i}{\hbar}\right)^3 \int_0^{t_3} dt_2 \int_0^{t_2} dt_1 \int_0^{t_1} dt_0 \left[V_I(t_2), [V_I(t_1), [V_I(t_0), \rho_I(t_0)]]\right]. \tag{4.9}$$

The nth order polarization response $\mathbf{P}^{(n)}(\mathbf{r}, t_n)$ is then given by

$$\mathbf{P}^{(n)}(\mathbf{r}, t_n) \propto \langle \mu(t) \rangle = \text{Tr}[\mu_I(t_n) \rho_I^{(n)}(t_{n-1})], \tag{4.10}$$

126

where Tr indicates the trace operation, and $\langle \mu(t) \rangle$ is the expectation value of the interaction picture dipole operator $\mu_I(t)$. The usual procedure for calculating polarization responses in the time domain is to assume well-separated pulses, and then calculate the polarization in the case when each of the input fields is considered to be a δ pulse. If it is desired, the response function may then be convolved with each of the input pulses (a triple convolution), followed by imposing the rotating wave approximation to throw out "antiresonant" terms.

4.3.1 Explicit Calculation of the First-Order Polarization Response of a Two-Level System

We will now examine the first-order response of a simple two-level system, in order to point out a few general features of the formalism, before moving on to a discussion of the third-order response functions that describe DFWM measurements. A schematic illustration of a delta-like input pulse $\mathbf{E}_a$ (black vertical line) that arrives at time $t_o = \tau_o$ and the system's response to it $P^{(1)}(t_1)$ (red curve) are shown in fig. 4-3. Mathematically, this process can be described by substituting eq. 4.7 into eq. 4.10 for the case when n=1, to get

$$\mathbf{P}^{(1)}(\mathbf{r}, t_1) \propto \text{Tr} \left[\mu_I(t_1) \int_0^{t_1} dt_0 \left[V_I(t_0), \rho_I(t_0) \right] \right]. \quad (4.11)$$

Comparing eq. 4.11 to fig. 4-3, we can see that the function of the commutator operation (and integral) is to "propagate" the density matrix in time from an initial time $t_0 = 0$ until time $t_0 = \tau_0$, which corresponds to $t_1 = 0$. The interaction picture dipole operator $\mu_I(t_1)$ then determines the expectation value of the dipole moment as a function of t_1. In most cases, we can assume that the system is at equilibrium prior to the arrival of the input pulse, such that there is no evolution of the system during the time interval τ_0.

In order to calculate $\mathbf{P}^{(1)}(\mathbf{r},t)$, we first need to determine $\mu_I(t)$, $\rho_I(t)$, and $V_I(t)$. For a two-level system that, the equilibrium density matrix ρ_o (assumed to be in the
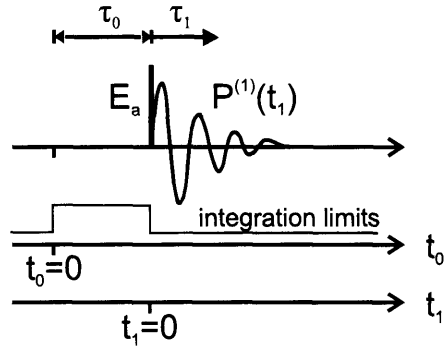
Figure 4-3: Schematic illustration of input pulse $\mathbf{E}_a$ (vertical black line) and system response $\mathbf{P}^{(1)}$ (red curve). Note that the top-hat function (thin line) indicates the range of values over which the integral in eq. 4.11 is evaluated.

ground state) and equilibrium Hamiltonian H_o may be written as:

$$H_o = \begin{pmatrix} E_0 & 0 \\ 0 & E_1 \end{pmatrix} \qquad \rho_0 = \begin{pmatrix} 1 & 0 \\ 0 & 0 \end{pmatrix}. \tag{4.12}$$

The interaction picture transition dipole matrix may be determined according to $\mu_I(t) = U_0^\dagger(t)\mu U_0(t)$ (see chapter 2 of reference [21]), where the equilibrium time-evolution operators $U_0^\dagger(t)$ and $U_0(t)$ are defined as:

$$U_0^\dagger(t) = \begin{pmatrix} \exp[iE_0 t/\hbar] & 0 \\ 0 & \exp[iE_1 t/\hbar] \end{pmatrix}$$

$$U_0(t) = \begin{pmatrix} \exp[-iE_0 t/\hbar] & 0 \\ 0 & \exp[-iE_1 t/\hbar] \end{pmatrix} \tag{4.13}$$

Using equations 4.13, we can calculate $\mu_I(t)$:

128

$$\mu_I(t) = U_0^\dagger(t)\mu U_0(t)$$

$$= \begin{pmatrix} \exp[iE_0 t/\hbar] & 0 \\ 0 & \exp[iE_1 t/\hbar] \end{pmatrix} \begin{pmatrix} 0 & \mu_{01} \\ \mu_{10} & 0 \end{pmatrix} \begin{pmatrix} \exp[-iE_0 t/\hbar] & 0 \\ 0 & \exp[-iE_1 t/\hbar] \end{pmatrix}$$

$$= \begin{pmatrix} 0 & \mu_{01}\exp[-i\omega_{10}t] \\ \mu_{10}\exp[i\omega_{10}t] & 0 \end{pmatrix}, \tag{4.14}$$

where the off-diagonal transition dipole matrix elements here are identical ($\mu_{01} = \mu_{10}$), and where $\omega_{10} = (E_1 - E_0)/\hbar$. Since the time-dependent portion of the Hamiltonian in the interaction picture is given by $V_I(t) = -\mathbf{E}(\mathbf{r}, t)\mu_I(t)$, no additional calculation is required to determine $V_I(t)$. The electric field of the delta-like input pulse given by

$$\mathbf{E}_a(\mathbf{r}, t) = E_a \delta(t) \exp[i(\mathbf{k}_a \mathbf{r} - \omega_a t)]. \tag{4.15}$$

Substituting the above equations into eq. 4.11, we obtain

$$\mathbf{P}^{(1)}(\mathbf{r}, t_1) \propto \text{Tr}\left[\begin{pmatrix} 0 & \mu_{01}\exp[-i\omega_{10}t_1] \\ \mu_{10}\exp[i\omega_{10}t_1] & 0 \end{pmatrix} \int_0^{t_1} dt_0 E_a \delta(t_0 - \tau_o) \exp[i(\mathbf{k}_a \mathbf{r} - \omega_a t_o)] \right.$$

$$\tag{4.16}$$

$$\left[\begin{pmatrix} 0 & \mu_{01}\exp[-i\omega_{10}t_0] \\ \mu_{10}\exp[i\omega_{10}t_0] & 0 \end{pmatrix}, \begin{pmatrix} 1 & 0 \\ 0 & 0 \end{pmatrix} \right] \right] \tag{4.17}$$

Note that since the system is assumed to be an equilibrium state up until the interaction with the pulse, there is no evolution during the time period t_0 and we may therefore set $\tau_0 = 0$ such that the first pulse is defined to arrive at the time $t_0 = 0$. Before evaluating the above equation explicitly, we will phenomenologically introduce

129

damping terms by substituting Ω_{kl} for ω_{kl}, where

$$\Omega_{kl} = \omega_{kl} + i\Gamma_{kl}. \tag{4.18}$$

Here Γ_{kl} represents either the rate of homogeneous dephasing for the state ρ_{kl}, when $k{\neq}l$, or the inverse of the lifetime of the state ρ_{kl} when when k=l. Alternatively, these damping terms may be introduced from the beginning in the form of a damping superoperator as part of the full Hamiltonian [21, 149]. We then obtain for the polarization response

$$\mathbf{P}^{(1)}(\mathbf{r}, t_1) \propto \mu_{01}\mu_{10}E_a \exp(i\mathbf{k}_a\mathbf{r})\Theta(t_1) \exp(-\Gamma_{01}t_1) \sin(\omega_{10}t_1), \tag{4.19}$$

where the Heaviside step function $\Theta(t_1)$ has been introduced such that there is only a polarization response at times following the input pulse (which occurs at t_1=0). Note that the the use of an input field whose temporal shape is that of a delta pulse makes the integral trivial. Equation 4.20 describes the free-induction decay of the system assuming all oscillators within the system are identical. In the case when there is an inhomogeneous distribution $G(\omega_o)$ of two-level systems with slightly different splittings, perhaps due to local solvation environments, the ensemble polarization response $\mathbf{P}^{(1)}_{ens}(\mathbf{r},t_1)$ becomes

$$\mathbf{P}^{(1)}_{ens}(\mathbf{r}, t_1) \propto \int\limits_{-\infty}^{\infty} d\omega_{10}\mathbf{P}^{(1)}(\mathbf{r}, t_1) \exp[-(\omega_{10} - \omega_o)^2/2\sigma^2]$$

$$\propto \mu_{01}\mu_{10}E_a \cos(\mathbf{k}_a\mathbf{r})\Theta(t_1) \exp(-\Gamma_{01}t_1) \exp(-\sigma^2 t_1^2/2) \sin(\omega_{10}t_1). \tag{4.20}$$

The term ω_o is the center frequency of the inhomogeneous distribution, and σ characterizes the width of the inhomogeneous distribution. In eq. 4.20 the inhomogeneous distribution $G(\omega)$ was assumed to be of a Gaussian form in order to produce a simple analytical result.

The form of the ensemble polarization response, $\mathbf{P}^{(1)}_{ens}(\mathbf{r},t_1)$ is a damped sinusoid whose decay is determined by the inhomogeneous distribution of oscillators as well as

the homogeneous dephasing time. The direction in which the first-order polarization response propagates is determined by $\mathbf{k}_a$, such that the emitted polarization response propagates in the same direction as the transmitted input field. The magnitude of the response is proportional to the product of the transition dipole matrix elements, $\mu_{01}\mu_{10}$, as well as the factor E_a that expresses the amplitude of the input field. To calculate the ensemble polarization response to a realistic input pulse of finite duration, eq. 4.20 would be convolved with an oscillatory input pulse, followed by imposing the rotating-wave approximation to discard the antiresonant terms, although we will not do so here.

4.3.2 Polarization Response for DFWM

We will now turn our attention to the calculation of the third-order DFWM response to three delta-like input pulses. A general equation for the third-order polarization response can be obtained by substituting eq. 4.9 into eq. 4.10 for the case when n=3, to obtain

$$\mathbf{P}^{(3)}(\mathbf{r}, t_3) \propto \text{Tr} \left[\mu_I(t_1) \int\limits_0^{t_3} dt_2 \int\limits_0^{t_2} dt_1 \int\limits_0^{t_1} dt_0 \right.$$
$$\left. [\delta(t_2 - \tau_2)\mu_I(t_2), [\delta(t_1 - \tau_1)\mu_I(t_1), [\delta(t_0 - \tau_0)\mu_I(t_0), \rho_I(t_0)]]] \right]. \quad (4.21)$$

The computations involved within eq. 4.21 are schematically represented in fig. 4-4. Each commutator operation propagates the system until the next interaction with the light field. As before, the system does not evolve during the time interval τ_0 since the system is assumed to be in its equilibrium state. The system evolution during time interval τ_1 and τ_2 is governed by the temporal separation of the three input pulses, as well as their order.

Instead of constructing matrices for $V_I(t)$, $\mu_I(t)$, etc., and evaluating eq. 4.21 explicitly, it is customary to use a form of double-sided Feynman diagrams to analyze nonlinear optical responses in systems. The principles for constructing Feynman
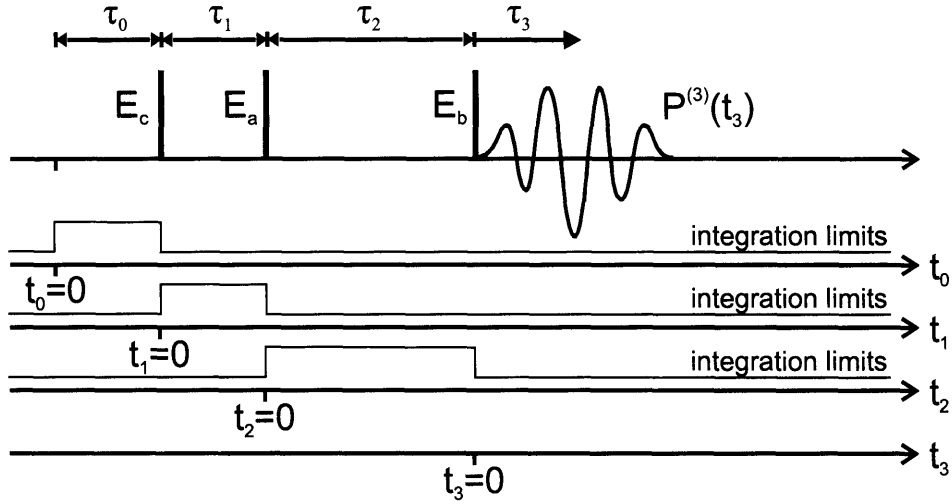
Figure 4-4: Schematic illustration of system-light interactions for four-wave mixing and the evolution of the system during the time intervals τ_0, τ_1, τ_2, and τ_3. Three pulses, E_a, E_b, and E_c (vertical black lines) are incident upon the system, generating a third-order polarization response (red curve). The top-hat functions (thin lines) represent the range of values over which the integrals in eq. 4.21 are evaluated.

diagrams are included in section 4.7, adapted from reference [21]. The basic idea behind the Feynman diagram approach is illustrated in fig. 4-4. All that is required to determine the polarization response of the system to a series of delta input pulses is to calculate the evolution of the system during the time intervals τ_1, τ_2, and τ_3. As stated earlier, if the system is at equilibrium during time interval τ_0, which is almost always the case, then there is no evolution of the system until the interaction of the first input pulse with the system. Assuming the system is a two level system initially in the ground state (as before), there are two possible DFWM diagrams when using the pulse sequence illustrated in fig. 4-4, labelled R_1 and R_2 in fig. 4-5. The pulse sequence corresponds to the photon echo measurement. R_1 and R_2 and are expressed as

$$R_1 + R_2 \propto |\mu_{01}|^4 \Theta(\tau_1)\Theta(\tau_2)\Theta(\tau_3) \exp[-\Gamma_{01}(\tau_1 + \tau_3)](1 + \exp[-\Gamma_{11}\tau_2]) \exp[i\omega_{01}(\tau_1 - \tau_3)].$$

$$(4.22)$$

The polarization response of an inhomogeneous distribution of systems can now

132

| | IOXOI | | IOXOI | | IOXOI | | IOXOI |
| | I1XOI | | I1XOI | | I1XOI | | I1XOI |
τ_2 | I1X1I | | IOXOI | | IOXOI | | I1X1I |
τ_1 | IOX1I | | IOX1I | | I1XOI | | I1XOI |
| | IOXOI | | IOXOI | | IOXOI | | IOXOI |
| R_1 | | R_2 | | R_3 | | R_4 |
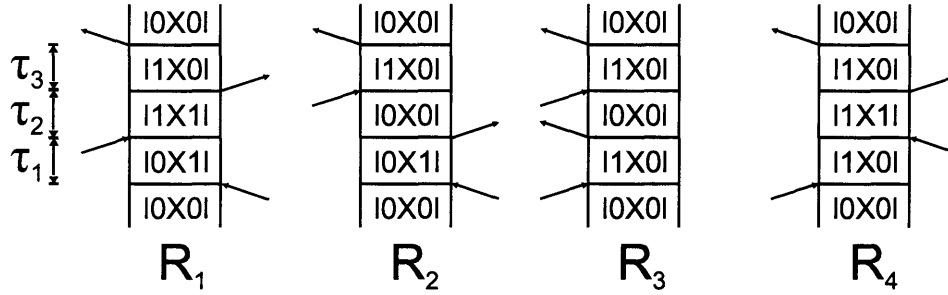
Figure 4-5: Possible DFWM diagrams for a two level system, initially in the ground state. R_1 and R_2 correspond to a photon echo measurement, while R_3 and R_4 correspond to a transient grating measurement.

be calculated via eq. 4.23:

$$\mathbf{P}^{(3)}(\mathbf{r},t) \propto \int\limits_0^\infty d\omega \exp\left(\frac{-(\omega - \omega_o)^2}{2\sigma^2}\right) \sum_k R_k, \qquad (4.23)$$

where, as before, ω_o is the center frequency of the inhomogeneous distribution corresponding to the ω_{01} transition, σ determines the inhomogeneous linewidth, and the summation is over the contributing diagrams R_1 and R_2. The resulting macroscopic polarization response is then

$$\mathbf{P}^{(3)}(\mathbf{r},t) \propto \exp[-\Gamma_{01}(\tau_1+\tau_3)](1+\exp[-\Gamma_{11}\tau_2]) \exp[-\sigma^2(\tau_1-\tau_3)^2/2] \exp[-i\omega_c(\tau_1-\tau_3)],$$

$$(4.24)$$

where the Heaviside functions are not explicitly shown to keep the expression compact. There are several interesting aspects of eq. 4.24. The Gaussian term resulted from the integration over the inhomogeneous distribution of oscillators and physically represents the rephasing of the oscillators that comprise the system. That is, the signal envelope, as a function of τ_3, will have its maximum amplitude when τ_3 equals τ_1 the *echo* in photon echo. As τ_1 is increased, the maximum amplitude of the signal envelope as a function of τ_3 decreases due to the homogeneous dephasing (from Γ_{01} of the individual oscillators within the system). As τ_2 is increased, the contribution from diagram R_2 decreases according to the lifetime (Γ_{11}) of the upper state. A 2D photon echo spectrum, the 2D Fourier-transformation of eq. 4.24 along τ_1 and τ_3, con-

133

sists of a single peak whose lineshapes along the diagonal and antidiagonal reveal the inhomogeneously broadened and homogeneous lineshapes, respectively (see fig. 4-6).

Figure 4-6: (left) Simulation of the 2D spectrum of a photon echo signal for an inhomogeneously broadened two-level system with $\tau_2 = 0$. (right) A slice through the diagonal yields the inhomogeneously broadened lineshape (blue) while a slice through the antidiagonal yields the homogeneous lineshape (dashed green).

If we change the timing of the pulses such that the conjugate field, $E_c(\mathbf{r},t)$, arrives at the sample second, the transient grating diagrams R_3 and R_4 (fig. 4-5) constitute the signal for our two-level system. We can now repeat the above procedure to find the polarization response for the transient grating signal of the two-level system, yielding

$$\mathbf{P}^{(3)}(\mathbf{r},t) \propto \exp[-\Gamma_{01}(\tau_1 + \tau_3)](1 + \exp[-\Gamma_{11}\tau_2]) \exp[-\sigma(\tau_1 + \tau_3)^2/2] \exp[-i\omega_c(\tau_1 + \tau_3)],$$

$$(4.25)$$

which is nearly identical in form to eq. 4.24, with the only exception that the sign of τ_3 is reversed in the last two terms. This difference in sign is significant as it eliminates the ability to distinguish inhomogeneous and homogeneous contributions to the lineshape for transient grating measurements, as seen in fig. 4-7. This concludes the possibilities of performing DFWM on two-level systems.

We will next consider the ensemble polarization response of a three-level system where a ground state may be coupled by the radiation field to two states. This configuration is similar to the 5S-5P transitions for the rubidium atom that will be discussed in section 4.5.2. For the moment, however, we will keep things general, and merely assume that there are three levels, labelled $|0\rangle$, $|1\rangle$, and $|2\rangle$, and where
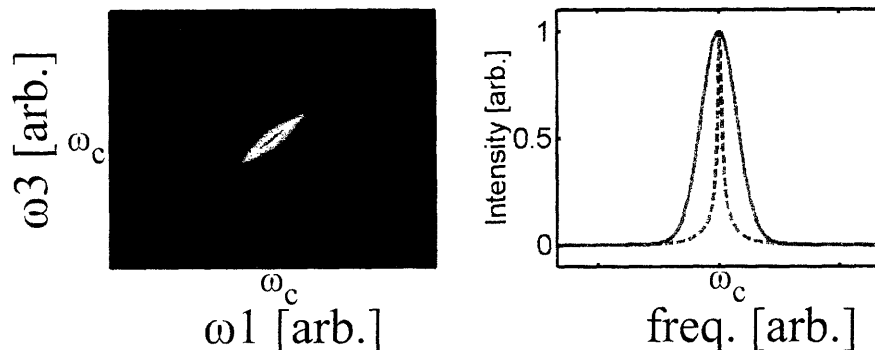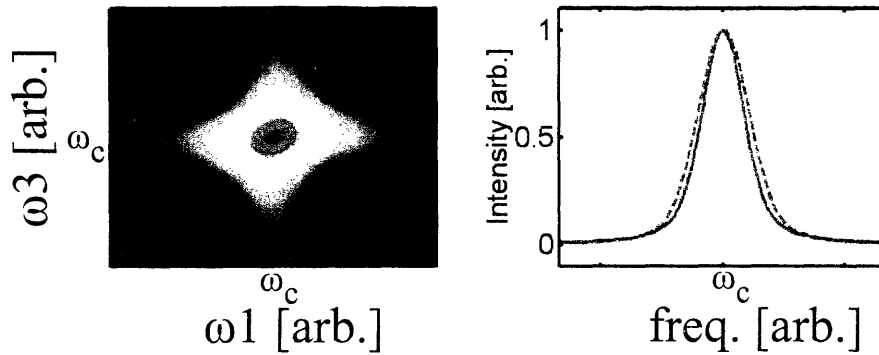
Figure 4-7: (left) Simulation of the 2D spectrum of a transient grating signal for an inhomogeneously broadened two-level system with $\tau_2 = 0$. (right) Slices along the diagonal (blue) and antidiagonal (dashed green) are not able to discern the homogeneous contribution to the lineshape as in fig. 4-6.

an incident light field may couple $|0\rangle$ to either of the other two levels, as shown in fig. 4-8 (a). With the introduction of the third level, many new diagrams contribute to the signal. These are shown in fig. 4-22, and are labelled R_1-R_{16} (ignore diagrams R_17-R_32 for now as they require a fourth state). By choosing the arrival time of the conjugate field to be before the other incident fields, we can restrict our consideration to only 8 diagrams, which correspond to the photon echo measurement. Among the 8 contributing photon echo diagrams, R_1, R_2, R_5, and R_6 are signals arising from two-level systems, which have already been calculated. In the two-dimensional spectrum, diagrams R_1-R_2 and R_5-R_6 will produce peaks along the diagonal of the 2D spectrum, centered at ω_{10} and ω_{20}, respectively. The remaining four diagrams, R_9, R_{10}, R_{13}, and R_{14}, produce off-diagonal peaks in the 2D spectrum, as can be seen by examining the time evolution within the diagrams during τ_1 and τ_3. Specifically, diagrams R_9 and R_{10} evolve with the frequency ω_{10} during τ_1 and frequency ω_{20} during τ_3, producing a cross-peak *above* the diagonal. Diagrams R_{13} and R_{14} evolve with the frequency ω_{20} during τ_1 and frequency ω_{10} during τ_3, producing a cross-peak *below* the diagonal.

A 2D spectrum for such a three-level ("V" shaped) system is shown in fig. 4-8. A slice through the diagonal of fig. 4-8 reproduces the linear absorption spectrum of the system. The cross peaks indicate couplings. In 2D infrared spectroscopy, cross peaks are used to help determine structural parameters, such as the relative angles

135

(a)

$$—— |2\rangle$$
$$—— |1\rangle$$

$$—— |0\rangle$$

(b)
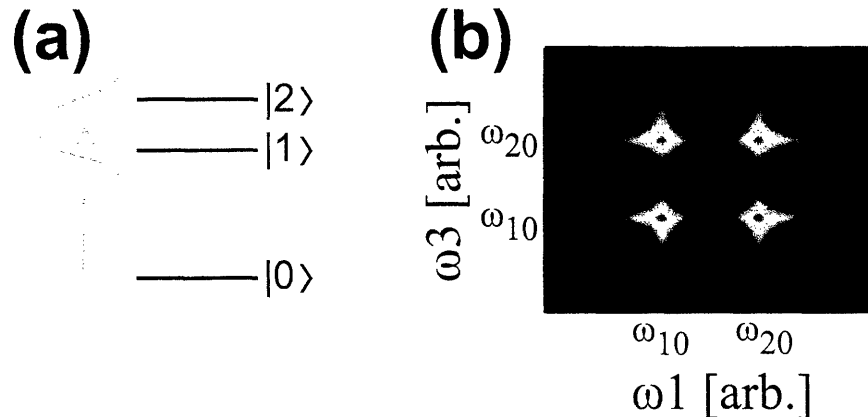
Figure 4-8: (a) Energy level diagram for a three-level system. (b) Simulation of a 2D spectrum for a three-level system where $\tau_2 = 0$, indicating diagonal and off-diagonal peaks. The same dephasing time (homogeneous linewidth) was used for all coherences, and the system was assumed to have no inhomogeneous broadening. Furthermore, all transition dipole moments were assumed to be equal.

between the transition dipoles, and the lineshapes of the given peaks are used to study relaxation dynamics.

4.4 Experimental Apparatus

The apparatus used for the experiments in this chapter is shown in fig. 4-9. The active component of the experiment is the two-dimensional pulse shaper configured in the diffraction-based pulse shaping arrangement discussed in section 2.8. Diffraction-based pulse shaping is used to generate four outputs that may each be independently shaped in phase and amplitude to create four nearly arbitrarily shaped output waveforms. The four regions are shown in the fig. 4-9 as blue, green, red, and light blue horizontal stripes within the beam. As described in section 2.8, a pair of razor blades was positioned at the focal plane (FP) to block all but the first-order diffraction spots produced by the sawtooth phase functions applied by the LC SLM. Notice that after a lens collimates the laser beam, the four shaped regions of the beam propagate coplanar and are therefore not arranged in the useful boxcars geometry discussed in the previous sections. Preliminary experiments in this coplanar geometry were reported in reference [68]. In order to configure the apparatus for the boxcars geometry, a

136

spatial mask with four holes on the vertices of an imaginary square was used to mask each horizontal region of the shaped laser beam. The imaginary square defined by the four holes of the mask was rotated by about 25 degrees from vertical such that each of the four holes of the mask was positioned within a different horizontal slice of the laser beam. The four transmitted regions of each of the horizontal slices were thus arranged in the boxcars geometry. The red, green, and light blue regions of the output pulse constituted the three input fields used to generate the nonlinear signal. The dark blue region was used for a reference local oscillator (LO) beam in order to characterize the emitted field, as will be discussed further, below. In some cases, the LO beam was blocked with a card at the position of the spatial mask.
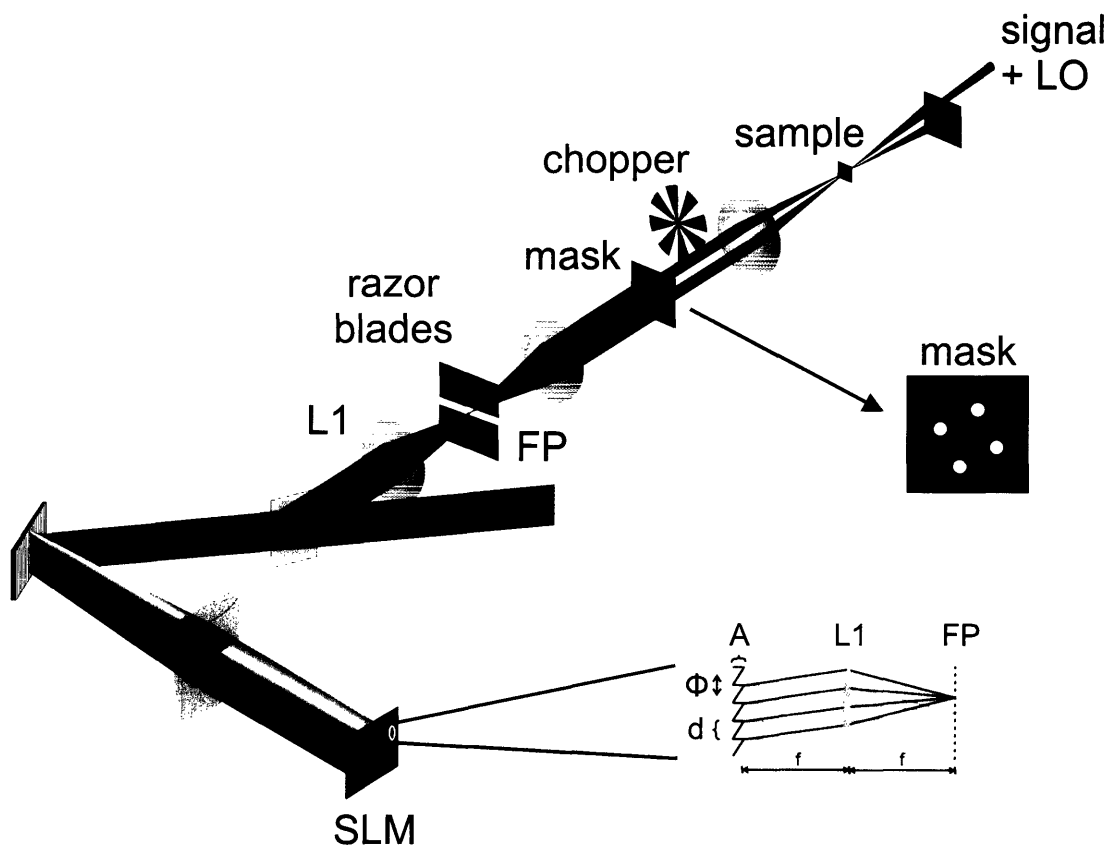
Figure 4-9: Experimental apparatus for degenerate four-wave mixing spectroscopy based on two-dimensional femtosecond pulse shaping.

After the spatial mask, the four beams were focused to a common point within the sample by another lens. All transmitted beams were then blocked except for the

the signal beam. In the cases when the LO beam was not blocked at the mask plane, the LO beam was incident upon the sample at such an angle that it copropagated with the outgoing signal beam. We will analyze the function of the LO pulse later in this section. When the LO pulse was used, it was necessary to attenuate it since the nonlinear signals were generally quite weak and would otherwise be completely overwhelmed by the much larger LO pulse.

Two methods were used to attenuate the LO pulse. For relatively strong signals, it was sufficient to reduce the amplitude of the sawtooth phase function on the LC SLM such that the LO beam amplitude was correspondingly reduced to about 2% of its maximum possible intensity. Due to the finite bit depth of the LC SLM, however, it is not possible to reduce the amplitude of the sawtooth phase function and still achieve good control over shaped outputs that are very weak. Essentially, the finite bit depth of the LC SLM doesn't allow for continuous adjustment of the pulse amplitude at values near to zero—below 2%, the amplitude drops abruptly. The second method that was used for attenuating the LO pulse was to place a neutral density (ND) filter within its beam path. Unfortunately, the glass substrates used for the ND filters possessed a small but significant amount of wedge shape to them, such that a beam transmitted through one of the ND filters would be deviated relative to the other beams. Therefore, a weak (0.1 optical density) ND filter on a nearly identical substrate was inserted into the path of the other three beams in addition to the stronger (2.0 optical density) ND filter in the path of the LO pulse, such that all beams were deviated by the same angle and therefore overlapped properly. The signals were either measured with a photodiode or a spectrometer. When a photodiode was used, one of the three input beams was chopped at half the repetition rate of the laser pulses to allow for lock-in detection.

A tremendous benefit of the apparatus is that all beams propagate through the same set of optics, such that the relative path length traversed by all beams is interferometrically stable. This property greatly facilitates the characterization of the emitted signal, required for most two-dimensional spectroscopic methods, since the signal field is detected by measuring the interference fringes between it and the co-

propagating LO reference field within a spectrometer. Small path length variations on the order of the wavelength of the laser pulses cause the interference fringes between the signal and LO to shift significantly and introduce crippling distortions in the measured signals. The common path geometry used here makes the apparatus insensitive to vibrations in the mounts and holders for each optic. Only relatively high-order vibrational modes, for instance the "warping" of a mirror or lens, are capable of introducing phase shifts between the beams. Air currents were not found to compromise the interferometric stability of the apparatus. During a full day of operation, the apparatus was not found to drift noticeably, and the root mean squared stability was measured to be $\lambda/50$.

Other groups have developed diffraction-based approaches for creating phase-stable two-dimensional DFWM apparatuses where refractive elements were used when scanning the delay one or more of the incident pulses [146, 150]. Although these approaches do possess excellent stability, they rely upon methods for delaying pulses which shift the envelope of a pulse along with its carrier phase. This means that as the delay is shifted, the phase of the delayed beam is also shifted, imparting a corresponding phase shift to the third order signal field. Since the delay and phase of the LO pulse are fixed, the interference fringes between it and the signal field also shift as a function of the delay of one of the input pulses. This requires that very small delay steps be used so that the interference fringes do not shift by more than half a period between successive measurements. Unfortunately, reproducibly delaying pulses by fractions of a wavelength is not a simple task. In the experiments described in references [146, 150], an additional measurement was used at each time step in order to precisely record the time delay between the delayed pulse and a reference pulse. This external measurement of the delay allowed for correction of phase errors due to the mechanical stages used to impart the delay.

Unlike pulse delay devices based on optical path-length variations (delay stages) or refractive delays based on glass components of adjustable thicknesses, delays generated by a pulse shaping apparatus only shift the *carrier envelope*. This means that with our pulse-shaping based approach, it is not necessary to increment delays by

fractions of the wavelength, reducing the number of measurements required and sim-
plifying the eventual data analysis. For envelope-delayed pulses, there is no benefit to
using delay increments smaller than approximately 1/4 of the duration of the pulse.
A 40 fs FWHM laser pulse centered at 800 nm requires only 100 delay steps per
picosecond (4 delay points per 40 fs envelope duration) when using envelope-delayed
pulses, while approximately 1500 delay steps (4 delay points per 2.7 fs optical period)
are required when using envelope and phase delayed pulses. In NMR, this decoupling
of a signal from its carrier frequency is known as detecting in the *rotating frame*, and
similarly reduces the number of required data points.

As discussed in chapter 2, the range of delay times accessible by the pulse shaper
is approximately ±4 ps. Depending on the delay of the pulse, the amplitude varies
(see fig. 2-14). If desired, amplitude shaping of the output pulse could be used to
compensate for the natural rolloff of the pulse as it is delayed or advanced from time
zero. Alternately, the rolloff may be accounted for in the data analysis by either
characterizing the rolloff prior to the experiment or by recording the intensity of a
pulse for all delays during a measurement.

One drawback of the apparatus is that much of the input laser energy is wasted.
Fortunately the experiments reported here did not suffer from the low efficiency of the
apparatus since there was an abundance of energy provided by our laser source—a
1 kHz amplified Ti:sapphire laser, with 1.5 mJ pulses of 50 fs duration and a center
wavelength of 800 nm. The losses arise from both the pulse shaping apparatus, which
is about 20% efficient, and the spatial mask, which is about 5% efficient. In the pulse
shaping portion of the apparatus, most of the losses arise from two passes through
a 50% beamsplitter. The 1200 lp/mm holographic grating is itself 90% efficient per
pass. On previous occasions, we have used the pulse shaper with the LC SLM slightly
tilted such that the reflected, modulated beam was sent out of the system at a small
angle relative to the input and could be picked off with a mirror. The efficiency of
this pulse shaping arrangement is about 80%. Methods to improve the efficiency of
the spatial masking process are currently under consideration. One approach would
be to reshape the beam with a custom refractive optic such that the beam only has

intensity in the region of the mask over the holes.

A wide variety of methods may be used to detect the emitted signal. The simplest scheme uses a photodiode or a photomultiplier tube to measure the time-integrated intensity of the signal as the pulse delays (or center frequencies, or optical phases, etc.) are varied. Note that such a scheme only records the energy of the signal pulse, and not its temporal properties. The questions of *when* was the signal emitted and what was its *phase* are critical for 2D time-domain spectroscopic measurements. Characterization of the emitted signal via methods based on FROG (see section 2.3) are not convenient since FROG requires many measurements (typically 50 or more) as a function of inter-pulse delay in order to characterize a signal. For a FWM measurement involving scanning the time delay between two incident pulses for a total of 300 steps, a full FROG trace would need to be recorded at each step, making the total number of measurements 15,000. Instead, experimenters typically use spectral interferometry [65, 60, 66] to rapidly characterize the signal field in just one or two measurements using a multichannel spectrometer.

In spectral interferometry, a reference field $\mathbf{E}_{ref}$ (fig. 4-2, left) that is already well-characterized is combined with the output signal beam and then the intensity of the coherent superposition of both fields is recorded by a spectrometer. The spectral intensity recorded is given by

$$
\begin{aligned}
I(\omega) &= |E_s(\omega)e^{i\phi_s(\omega)} + E_{ref}(\omega)e^{i(\phi_{ref}(\omega)+2\pi\tau)}|^2 \\
&= I_s(\omega) + I_{ref}(\omega) + 2|E_s(\omega)||E_{ref}(\omega)|\cos(\phi_s(\omega) - \phi_{ref}(\omega) - \tau\omega), \quad (4.26)
\end{aligned}
$$

where the signal and reference pulses have been expressed in the frequency domain, and where τ is the delay between the (first moments of the) signal and reference pulses. The cross-term in eq. 4.26 is a function of the time delay between the signal and reference fields, τ, and the difference between the spectral phases of the signal and reference fields. Typically, the reference field spectral phase and amplitude are independently determined through a measurement such as FROG [59]. One addi-

tional measurement may be used to determine the spectral amplitude ($|E_s(\omega)|$) of the signal field, such that the remaining unknown quantities τ and $\phi_s(\omega)$ may then be determined by the measured spectral interferogram, as described in [65, 66]. As opposed to the 15,000 measurements required for the above example with FROG, only 600 measurements are required for this implementation of spectral interferometry. Inverse Fourier-transformation with a computer may then be used to reconstruct the temporal phase and intensity of the signal field if desired.

4.5   Experimental Results

In the remainder of this chapter, we will present the first generation of experiments based on our new approach to coherent nonlinear optical spectroscopy. As with any new method, a first objective is to generate results from systems that we believe can be modelled accurately so that the method itself can be tested thoroughly. To that end, the first experiments discussed are heterodyne-detected transient grating measurements of liquid diiodomethane, a nonresonant system that is Raman active. Single- and multiple-pulse excitation are used to generate and manipulate ground electronic state wavepackets excited via impulsive stimulated Raman scattering. Next, one- and two-dimensional DFWM measurements of atomic rubidium vapor are described. Some of the versatility of the apparatus is demonstrated with measurements conducted in the frequency domain (via spectral filtering of the input beams), and in a hybrid time-frequency domain measurement (delayed pulse in one input beam, and spectral filtering of other beams). Finally, we will present photon-echo measurements on potassium dimer molecules in the gas phase, with different pulse sequences that exert a strong influence on the system response. We also demonstrate powerful phase-cycling methods borrowed from multidimensional NMR, which allow for the isolation of the nonlinear signal of interest in the presence of competing signals that would otherwise seriously degrade the measurements.

4.5.1   Transient Grating Measurements on Diiodomethane

Two vibrational modes of diiodomethane are accessible by our laser pulses, the C-I symmetric stretch at 488 cm^{-1} and an I-C-I bending mode at 123 cm^{-1} (see fig. 4-11). These vibrational modes may be excited by ISRS (see section 3.2) as part of a DFWM measurement. The pulse configuration will be that of a transient grating measurement (SII), with the delay between the first two pulses set to zero. Since there are no resonant transitions in diiodomethane that occur within the spectral bandwidth of our laser, pairs of light-matter interactions occur simultaneously. For a given Raman-active vibrational mode, then, two diagrams contribute to the DFWM signal, as shown in fig. 4-10. The expected signal for delta-like input pulses is

$$\mathbf{P}^{(3)}(\mathbf{r}, \tau_2) \propto \Theta(\tau_2) \exp(-\Gamma_{01}\tau_2) \sin(\omega_{10}\tau_2). \qquad (4.27)$$

Note that the polarization response is identical to the free-induction decay result derived in section 4.3.1 for the response of two-level system to a delta-like input pulse (see eq. 4.20). However, it should be noted that the free-induction decay in that calculation was a first-order response that was resonant with the frequency of the incident laser field, while the present vibrational free-induction decay is a second-order response that is resonant with neither incident field but with differences among the Fourier components contained within their bandwidths. Furthermore, the result is identical to that obtained classically when ISRS was introduced section 3.2. Since there are two Raman-active modes in diiodomethane whose frequencies are within the bandwidth of the laser pulse, both modes will be excited, making the generated signal the sum of the two free-induction decay signals.
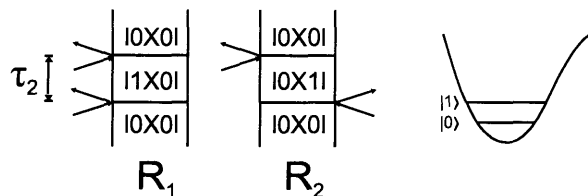

Figure 4-10: Two contributing Feynman diagrams describing a nonresonant transient-grating DFWM measurement involving a single vibrational mode.

Figure 4-11 shows the transient grating signal (c) for diiodomethane in a 1 mm path length cuvette at room temperature, consisting of both slow and fast oscillatory components, as well as a large nonresonant electronic response at time zero (not described in the Feynman diagrams for this process). The frequencies of the fast and slow oscillations agree with the expected frequencies, shown in (d). The pulse sequence is illustrated in (b), where the conjugate pulse, $\mathbf{E}_c$, arrives at the sample time-coincident with pulse $\mathbf{E}_a$. At a variable delay time controlled by the pulse shaping apparatus, a probe pulse, $\mathbf{E}_c$ is then scattered to create a signal pulse $\mathbf{E}_s$ whose dependence upon τ_2 is identical to that of the polarization response of the system. Added coherently to the variably delayed probe pulse is a reference pulse $\mathbf{E}_{LO}$ whose delay is perfectly matched to that of the probe pulse. The time-integrated intensity $I_s(\tau_2)$ recorded by the photodiode as a function of the probe/LO delay is given by

$$
\begin{aligned}
I_s(\tau_2) &\propto |E_s(\tau_2) + E_{LO}(\tau_2)|^2 \\
&\propto I_s(\tau_2) + I_{LO}(\tau_2) + 2|E_s(\tau_2)||E_{LO}(\tau_2)|\cos(\Delta\phi) \\
&\approx I_{LO}(\tau_2) + 2|E_s(\tau_2)||E_{LO}(\tau_2)|\cos(\Delta\phi),
\end{aligned}
\tag{4.28}
$$

where the the approximation holds true for signals that are much weaker than the reference pulse, and where $\delta\phi$ here represents the phase difference between $\mathbf{E}_s$ and $\mathbf{E}_{LO}$. When the phase of one of the input beams (beam $\mathbf{E}_c$) is flipped by π with the pulse shaper, the argument of the cosine term is then shifted by π, imparting an opposite sign to the signal as shown in the green trace in (c). The green signal has been displaced from the blue trace for the sake of clarity. Since this detection scheme relies upon interference between the emitted signal and the reference pulse, all four incident beams must be interferometrically stable, which is clearly the case here.

A second set of transient grating measurements is shown in fig. 4-12. This time, the pulse shaping capabilities were used to produce a pair of output pulses for each of $\mathbf{E}_a$ and $\mathbf{E}_c$ with a variable interpulse separation, Δ. The configuration is similar that used

144
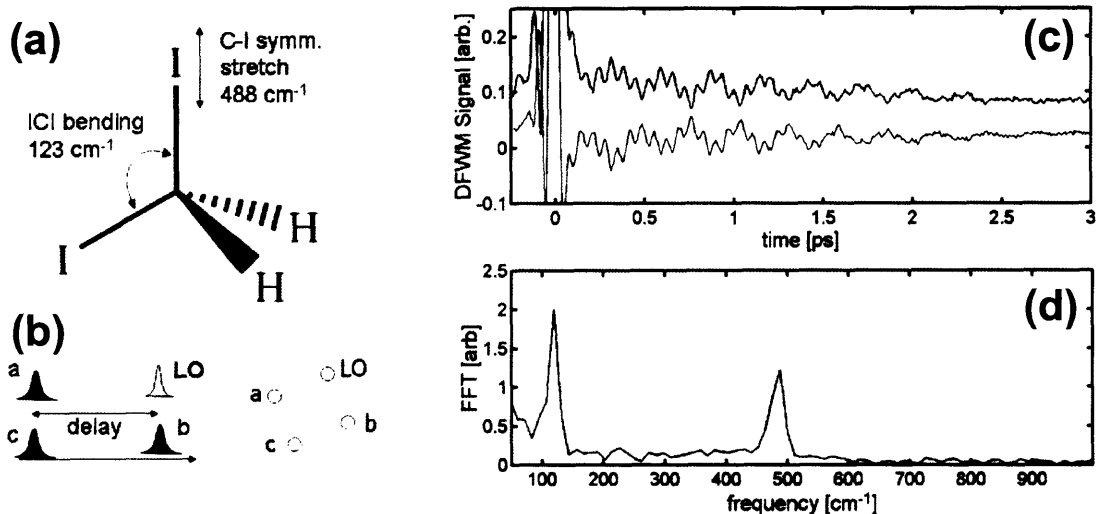
Figure 4-11: (a) Diiodomethane molecule, and Raman-active vibrational modes accessible by the laser pulses. (b) Pulse sequence and beam geometry. (c) Heterodyne-detected transient grating signals with (green) and without (blue) one of the input beam phases flipped by π. (d) Fourier transform of blue signal in (c), indicating the expected vibrational modes.

by Weiner et al. [6] for multiple-pulse excitation used to coherently control crystalline vibrational modes. The pulse sequence is shown in (a). Note that the second pulse within each pulse pair was fixed at time zero and the first pulse was shifted in time to precede the second pulse by Δ. A transient grating measurement was performed for many different values of the interpulse separation. The full two-dimensional data set is shown in (b). Thick white lines in the shape of the letter V indicate the nonresonant electronic response (saturating the colormap). Quite intuitively, when the interpulse delay corresponds to an integer multiple of a vibrational period, an enhancement of the vibrational response is observed. For instance, when Δ=0.27 ps, which is one vibrational period of the bending mode, a stronger oscillatory signal at the bending mode frequency is observed. For Δ=0.41 ps, which is a half-integer multiple of the period of the bending mode, the slower oscillatory signal is no longer observed. In these cases, the coherent vibrational response driven by the second pulse is in phase or out of phase, respectively, with the coherent response driven by the first pulse. Slices for various values of Δ are shown in (c), where the measured signals contain either fast or slow oscillatory components. This is clearly seen in the Fourier transform of

145

the full data set in for all values of Δ shown in (d), where either vibrational mode may be suppressed or enhanced (peaks near 120 cm^{-1} and 500 cm^{-1}) depending upon the interpulse delay.
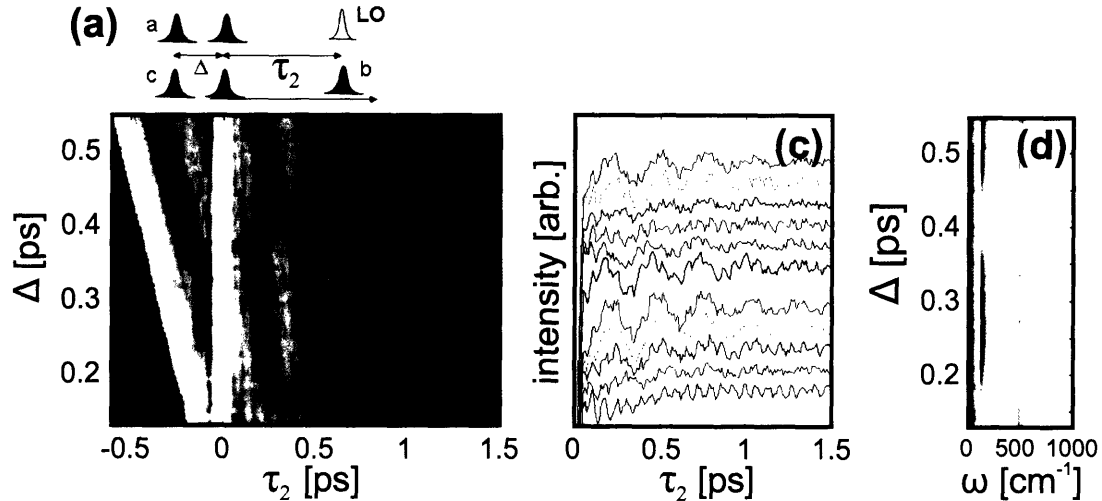
Figure 4-12: (a) Double-pulse excitation pulse scheme. (b) Transient grating data recorded as a function of interpulse delay Δ and probe delay τ_2. (c) Horizontal slices through (b) for selected values of Δ. (d) Fourier-transform of (b) for different values of Δ.

From the transient grating measurements shown in this section, it is clear that the DFWM apparatus based on 2D pulse shaping may be used for sophisticated non-linear optical measurements requiring interferometric phase stability (for heterodyne detection) and precise delays between pairs of incident pulses. All pulse delays, phase modulations, and pulse shapes (i.e. multiple pulse waveforms) were created by varying the pattern on the computer-controlled LC SLM. Multiple pulse excitation is easily implemented and can help to simplify the system response. Furthermore, the ability to manipulate the phase of the signal beam by modulating the phase of the input pulses foreshadows the phase-cycling methods that will be used in later sections to eliminate spurious signals not dependent upon all input beams.

4.5.2 DFWM Measurements of Rubidium Atoms

Atomic rubidium vapor is a convenient four-level system for users of ultrafast lasers because it possesses multiple electronic resonances in the vicinity of the Ti:sapphire

laser bandwidth (around 800 nm). The commercially available (Triad Technology Inc.) rubidium sample cell consists of a 2 inch path length quartz cell containing 20 mTorr of helium buffer gas in addition to a small amount of rubidium. The cell was heated to approximately 130° C. Fig. 4-13 shows the relevant energy levels and the transition wavelengths. Depending on the bandwidth of the laser pulse, some or all of the transitions may fall within the laser bandwidth, such that the system may effectively be: a 2-level system (laser bandwidth only spans the 5S-5$P_{1/2}$ transition); a 3-level system with a "V" shape (laser bandwidth spans both 5S-5P transitions); a 3-level system with a second excited state (laser bandwidth only spans the 5S-5$P_{3/2}$ and 5$P_{3/2}$-5D transitions); or a 4-level system where the laser bandwidth spans all possible resonances.
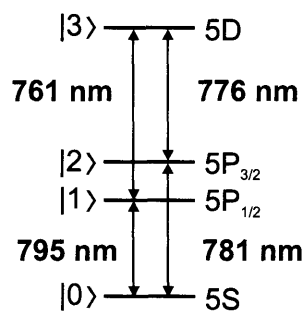
Figure 4-13: Energy level system for gas phase Rb atoms and corresponding transition wavelengths.

Our first DFWM measurement on rubidium atoms constitutes a mixed time-frequency domain measurement. Pulses E_a ad E_c were each shaped such that their spectral amplitude consisted of two reasonably narrow frequency bands centered at the two 5S-5P transition frequencies. Pulse E_b was then variably delayed in time, and the time-integrated signal was then measured with a photodiode, yielding an oscillatory transient whose frequency corresponds to the energy difference between the 5P levels, as shown in fig. 4-14 (a). When the phase of the blue spectral components of beams E_a and E_c are both shifted by π with the pulse shaping apparatus, the phase of the transient signal also shifts by π (b). It should be noted that the oscillations persisted much longer than the time window shown here, ruling out the possibility that the transients are simply a measure of the beats produced in the excitation

147

pulses as a result of the spectral shaping (a pulse with two frequency stripes creates an oscillating pulse envelope in time). Based on the width of the two spectral stripes used, the FWHM duration of the waveforms in E_a and E_b should be about 0.7 ps, centered at time zero. The amplitude envelope of the oscillations in fig. 4-14 results from two separate effects.
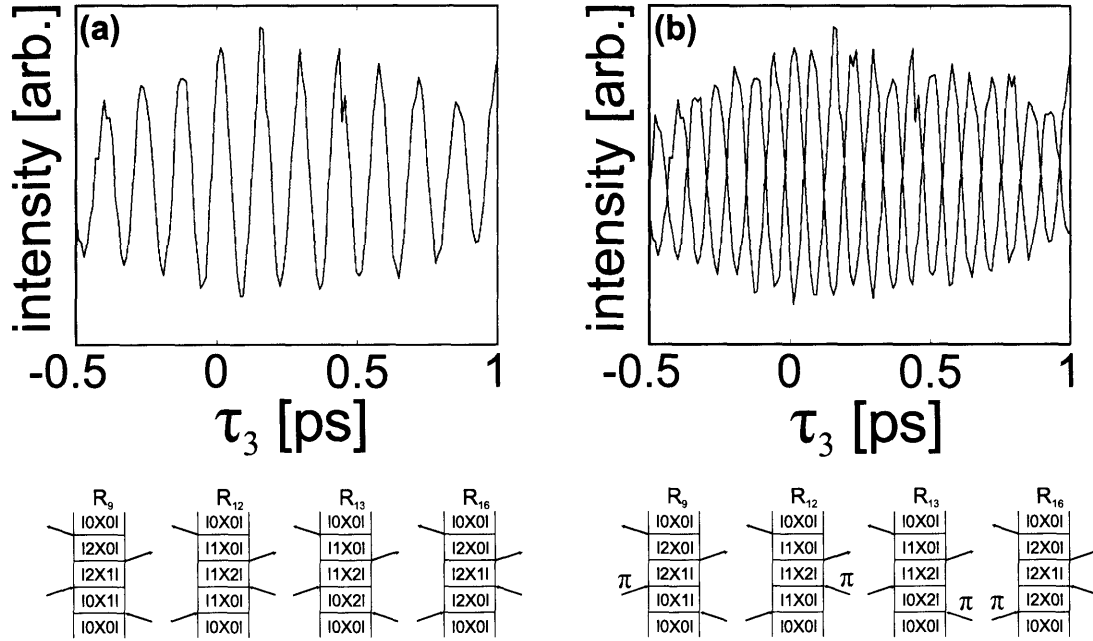
Figure 4-14: Hybrid time-frequency domain DFWM measurements in rubidium vapor. (a) Relevant diagrams contributing to transient signal. (b) Phase-shifting the "blue" spectral components of E_a and E_c by π results in a π phase shift of the measured transient (green curve).

The signals in fig. 4-14 can be easily understood by inspection of the relevant Feynman diagrams. For rubidium vapor, there are a total of 32 diagrams corresponding to all possible DFWM quantum pathways. These diagrams are shown in fig. 4-22 within section 4.7. They are divided up into three categories. The left two columns contain the photon echo diagrams (also called SI, or rephasing diagrams), while the middle two columns contain the transient grating diagrams (also called SII, or non-rephasing diagrams), and the right two columns contain an additional set of diagrams called SIII diagrams. Note that in each of the three groups, the time-ordering of the conjugate field (left-tilted arrow of the first three interactions) dictates which set of

pathways contribute to the signal observed at the fourth corner of the box. For SI diagrams , the conjugate field precedes the other two fields, while for SII diagrams, the conjugate field interaction occurs between the other two interactions, and for SIII diagrams the conjugate field interaction occurs last. In the case when the conjugate field precedes the other two input fields, signals resulting from the SI diagrams propagate in the direction of the fourth corner of the box. Signals from the other two sets of pathways (SII and SIII) are not suppressed, but merely travel in a different direction than the fourth corner of the box. They travel in the direction $E_{s'}$ and $E_{s''}$, as shown in fig. 4-2). Note that the SIII diagrams as well as diagrams R_{17}-R_{23} involve two sequential ket-side "absorptions," which means that these pathways are not possible for a two-level system—use of the SIII time ordering for a two-level system should therefore produce no signal in the direction of the fourth corner of the box.

Out of the 32 total diagrams, we will restrict our attention to only those diagrams that do not involve the level $|3\rangle$, R_1-R_{16} in fig. 4-22, which are sufficient for the present purposes. Since pulses $\mathbf{E}_a$ and $\mathbf{E}_c$ are overlapped in time and pulse $\mathbf{E}_c$ arrives at the sample after a delay of τ_2, both the SI and SII diagrams should contribute to the signal in the direction of the fourth corner of the box. For the three level system being considered, diagrams R_1-R_{16} are accessible. Of these diagrams, only four evolve in a coherence during τ_2 (R_9, R_{12}, R_{13}, and R_{16}) meaning that the other 12 diagrams produce a constant signal as a function of τ_2 (in the limit of long lifetimes, which is certainly the case for these measurements) which may interfere with the 4 diagrams that have a coherence during τ_2. In fig. 4-22 (a), these four relevant diagrams are indicated. These diagrams interfere with the 12 diagrams that do not evolve in a coherence during τ_2. When the phase of the "blue" spectral component within $\mathbf{E}_a$ and $\mathbf{E}_c$ is phase shifted by π, the four pathways indicated incur a π phase shift, such that the resulting interferences with the non-evolving terms is phase-shifted by π.

Although there is certainly more to explore with the hybrid time-frequency domain experiments, such as multi-color time-domain experiments that will allow the maximum level of control over the possible quantum pathways on the basis of pulse timing and spectral tuning, there are also interesting possibilities for purely spectral-domain

measurements. A *two-dimensional* measurement directly in the spectral-domain is shown in fig. 4-15 (a). For this scan, fields $\mathbf{E}_a$ and $\mathbf{E}_b$ covered all three spectral transitions except for the $|1\rangle - |3\rangle$ transition due to there being no laser bandwidth at the corresponding wavelength. Pulse $\mathbf{E}_c$, the conjugate field, consisted of a narrow frequency component. The DFWM signal generated in this configuration was then measured with a spectrometer (vertical axis) as a function of the center frequency of $\mathbf{E}_c$.
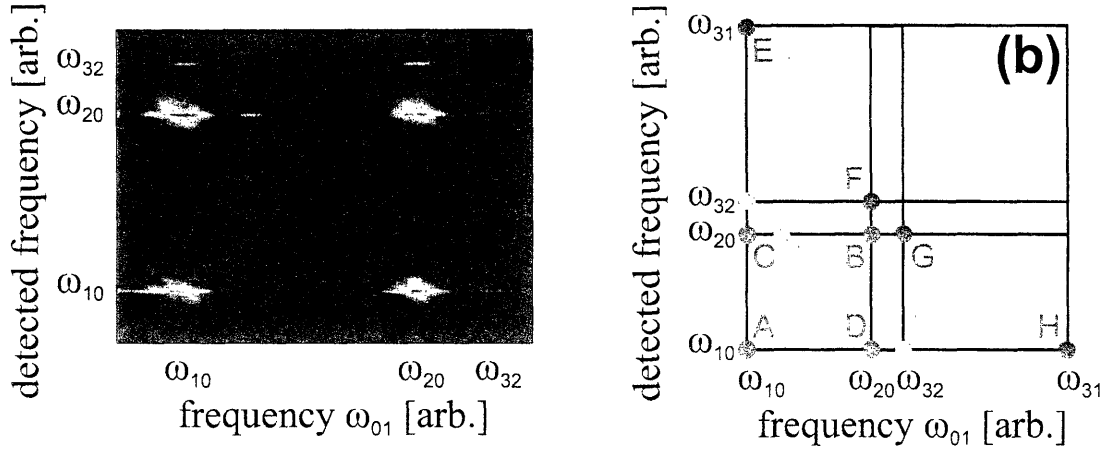
Figure 4-15: Two-dimensional spectrum of Rb. The y-axis represents the detection frequency of the spectrometer, and the x-axis represents the excitation frequency of the conjugate field, labelled here as ω_c. (a) Measured 2D spectrum. The faint line along the diagonal is scattered light from $\mathbf{E}_c$ as it was being scanned. (b) Schematic illustration labelling various peak positions. Green and blue circles represent the expected peaks. Red circles represent additional peaks observed in the experiment, possibly due to effects out of the perturbative limit.

Many peaks are observed in the 2D DFWM spectrum of rubidium. The most prominent peaks, labelled A-D in the schematic in fig. 4-15 (b), arise from diagrams R_1-R_{16}. Since the three input pulses are time-coincident, neither group of quantum pathways (SI, SII, or SIII) is selected by pulse ordering. Although the peaks A-D have the same overall shape as the 2D photon echo spectrum for a three-level system (fig. 4-8), an additional set of 16 diagrams (R_{17}-R_{32}) are able to contribute to the 2D DFWM spectrum of rubidium. Peaks E-H in (b) arise from quantum pathways involving the state $|3\rangle$, although there are also contributions from SI, SII, and SIII diagrams in peaks E and F. Peaks G and H in (b) arise from SIII pathways. Peaks

E and h were not observed in the 2D spectrum of rubidium, and the spectral range in (a) therefore does not cover this range. There are also three weak peaks, I-K, observed in the 2D DFWM spectrum of rubidium that are not explainable with these diagrams.

Peak Label	Corresponding Diagrams
A	R_1, R_2, R_3, R_4
B	R_5, R_6, R_7, R_8
C	R_9, R_{10}, R_{11}, R_{16}
D	R_{12}, R_{13}, R_{14}, R_{15}
E	R_{21}, R_{23}, R_{32}
F	R_{18}, R_{20}, R_{22}, R_{24}, R_{28}
G	R_{27}
H	R_{25}, R_{31}
I-K	???

Table 4.1: Peak labels for 2D rubidium spectrum in fig. 4-15 and corresponding Feynman diagrams. The diagrams are shown in fig. 4-22.

Further measurements should help to uncover the origin(s) of the unexpected peaks I-K. One possible cause is that the input light fields are sufficiently strong that they are no longer in the weak-limit where third-order perturbation theory is valid. Due to the narrow linewidth of rubidium's absorptions, it is difficult to estimate the optical density of the peak absorption. Recently, however, a new rubidium cell was obtained that contains close to a 0.5 atm buffer gas pressure such that the absorption lineshape will be resolvable with our spectrometer due to pressure broadening (approx. 0.5 nm). Another possible cause of the unexplained peaks is that they may arise from a higher-order nonlinear optical processes (i.e. fifth-order, seventh-order). If this is the case, then the phase-cycling schemes described in the next section (in combination with the use of a LO pulse to permit phase-sensitive detection) may be used to discriminate between signals originating from higher-order nonlinear optical processes. Also, the spectrum of E_a and E_b could be manipulated (i.e. tuned to only span one or two resonances) in order to determine the dependence of the signal on various spectral contributions of these pulses.

151

Unlike the 2D Fourier-transform measurements, which can take on the order of 1-12 hours to record and which require involved procedures for data analysis, the present 2D spectrum was obtained in less than 1 minute. The data acquisition time will be even faster once a a recently acquired MEMS-based 2D SLM is used in place of the LC SLM. The MEMS device can operate at 500 Hz, while the LC SLM typically operate at 2-4 Hz. Further measurements and analysis should be performed to determine the connection between the novel 2D scan approach used above and the methods used in 2D Fourier-transform spectroscopy to obtain absorptive 2D spectra [3, 20, 146, 47]. These methods involve adding a measured 2D photon echo spectrum with a measured 2D transient grating spectrum to yield the 2D absorptive spectrum. The absorptive spectrum is especially useful when the sought-after information is contained within the broad wings of the lineshape or when the sign of the individual peaks within the 2D spectrum is desired [3].

To determine the absorptive spectrum using our novel spectral scanning approach, the appropriate combination of SI and SII pathways must be sampled. This may be easily achieved by shifting the spectrally broad pulses $\mathbf{E}_a$ and $\mathbf{E}_b$ in time such that neither overlaps temporally with the spectrally narrow pulse $\mathbf{E}_c$. Then, in order to select the SI pathway, $\mathbf{E}_a$ and $\mathbf{E}_b$ should follow $\mathbf{E}_c$ in time, or to select the SII pathway, one of the pulses (for instance $\mathbf{E}_a$) should precede $\mathbf{E}_c$ and the other pulse ($\mathbf{E}_b$) should follow $\mathbf{E}_c$. These measurements will require heterodyne detection in order to determine the absolute signs of the peaks, and phase cycling methods may be necessary to remove artifacts from the data (see phase-cycling discussion below). It may even be possible to use a double-pulse waveform within one of the beams, for instance $\mathbf{E}_a$, such that one of the pulses arrives before $\mathbf{E}_c$ and the other arrives after $\mathbf{E}_c$. Since $\mathbf{E}_b$ would still be timed to follow $\mathbf{E}_a$, this pulse sequence would yield the absolute value 2D spectrum in a single experiment. The group of Peter Hamm uses a similar two-beam approach for 2D infrared spectroscopy [151]. Unlike their method, which relies upon two interactions between a spectrally narrow field and the sample followed by one interaction between the sample and a spectrally broad field, our method still allows for independent manipulation of each interacting field. Our

method should also allow for the prospect of incorporating a waveplate and polarizer in the path of each separate input pulse. Use of variably-polarized input pulses has allowed for powerful simplifications of 2D infrared spectra [152].

4.5.3 Potassium Dimer

A final set of photon-echo experiments, en route to two-dimensional time-domain spectroscopy, were performed on potassium dimer molecules in the gas phase. Rubidium, it turns out, is not a good sample for photon echo measurements since the system is not inhomogeneously broadened and since all atoms start in the same initial state. In eq. 4.24, was saw that the Gaussian inhomogeneous distribution was responsible for the "echo" behavior that causes the peak of the signal to appear at a time τ_1 after the final input pulse. In the absence of significant inhomogeneity, then, the signal would simply be expected to rapidly decay as a function of τ_3. The large inhomogeneous broadening in potassium dimer arises from the large number of rovibrational transitions between the $X^1\Sigma_g^+$ and $A^1\Sigma_U^+$ electronic energy surfaces.

The potassium dimers were contained within in a home-built heat pipe that was heated to 420°. The heat pipe contained approximately 10 g of solid potassium within a buffer gas of 100 mbar helium buffer gas. In the temperature range we used, the first approximately 7 vibrational levels of the the X state were populated. With our laser center wavelength of 815 nm, we were able to access the v=20-30 vibrational levels of the excited state. Note that the center wavelength of the laser pulse was tuned so that two strong electronic resonances of atomic potassium (the doublet), at 766.5 nm and 769.9 nm, did not fall within the bandwidth of the laser pulse.

In order first to confirm that we had generated potassium dimers within the heat pipe, we performed a two-pulse, time-integrated photon echo measurement using a modified FROG apparatus to produce a two-pulse photon-echo signal. The pulse sequence used is shown in fig. 4-16, where one of the second two pulses, $\mathbf{E}_c$, is the conjugate field. A complicated transient is obtained (a), with many peaks in the Fourier-transformation (b). Since these peaks occurred at integer multiples of the vibrational periods of the ground and excited electronic states of potassium dimer,
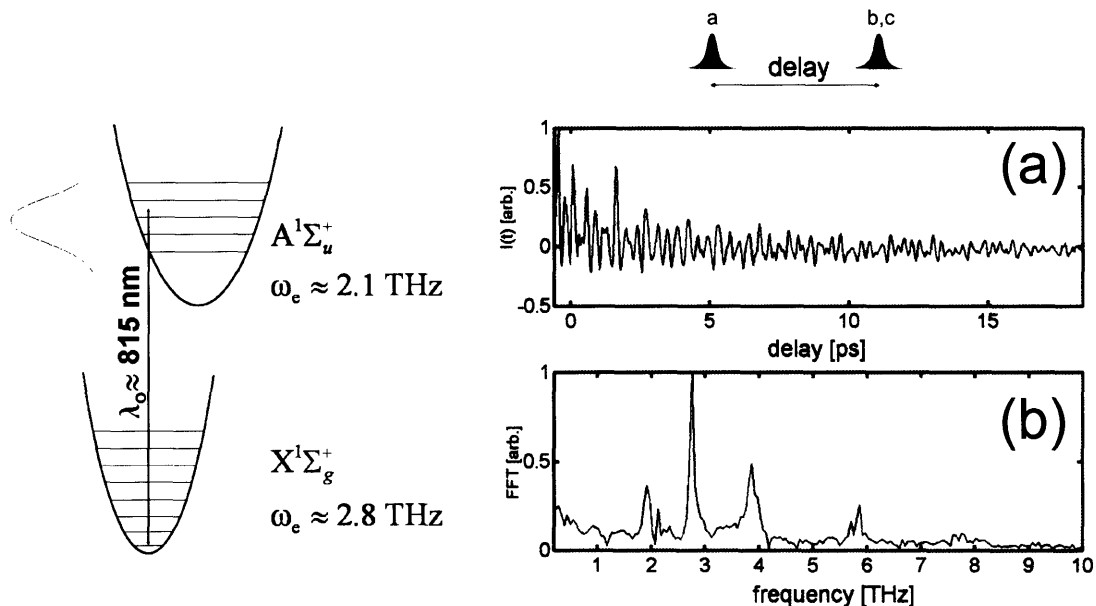
Figure 4-16: (left) Schematic illustration of relevant electronic energy levels for potassium dimer. (a) Time-integrated photon-echo trace of potassium dimer with a complicated oscillatory structure. (b) Fourier transform of (a), indicating oscillatory frequencies at integer multiples of the ground electronic state and excited electronic state vibrational frequencies.

and not at the frequency corresponding to the potassium doublet (1.7 THz) it was clear that the heat pipe was operational.

We next used our pulse-shaping based apparatus to perform three-pulse photon echo measurements on potassium dimer molecules. Time-integrated three-pulse photon-echo measurements on potassium dimer are shown in fig. 4-17. When the delay τ_1 was set to 540 fs, the observed transient in (a) contained only a single frequency component [see (b)] at the frequency corresponding to the ground state vibrational period. When τ_1 was set to 540 fs and the delay τ_2 was scanned, an oscillating transient (a) recorded as a function of τ_2 was observed whose frequency of approximately 2.8 THz corresponds to the vibrational frequency of the ground electronic state (b). When τ_1 was set to 720 fs, the observed transient (c) measured as a function of τ_3 oscillated with a frequency corresponding to the ground state vibrational frequency (d). Thus it is clear that the choice of pulse sequence is able to influence whether or not the measurement is sensitive to dynamics on the excited or the ground elec-

154

tronic surface. These effects have received a fair amount of attention in the literature [153, 154, 155, 156]. The basic idea is that the time delay between pulses $\mathbf{E}_c$ and $\mathbf{E}_a$ controls whether or not the system evolves on the ground or excited state energy surfaces during τ_3. See ref. [154] for a detailed explanation.
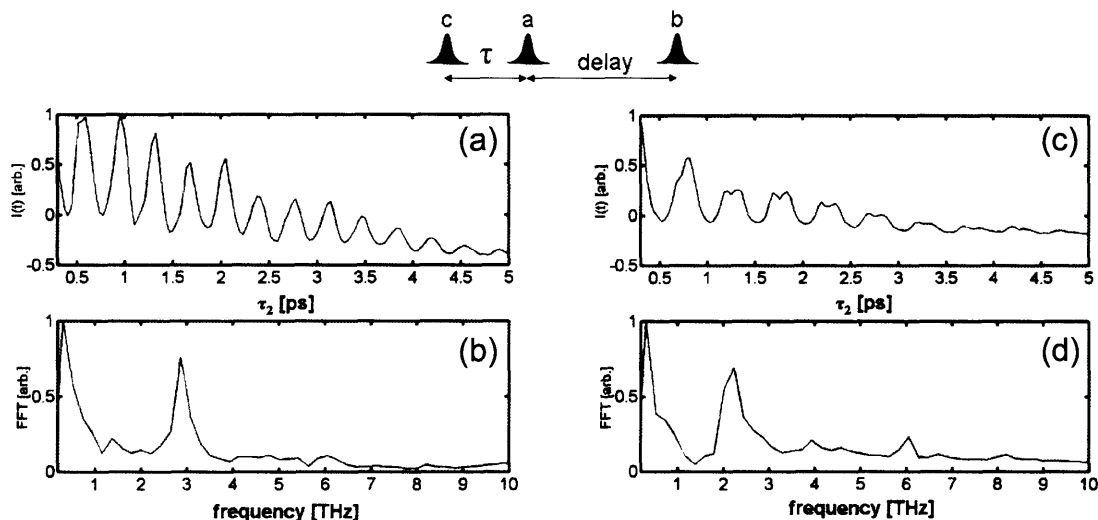
Figure 4-17: (a) Time-integrated three-pulse photon echo measurement of potassium dimer molecules, where the delay between the first two pulses was set to be 540 fs, and its Fourier transform (b). When τ_1 was set to be 720 fs, the resulting transient (c) oscillated at the frequency of the excited state vibrational frequency (d).

The next step was to introduce a local oscillator beam that could be used to characterize the emitted signal in time through spectral interferometry. Unfortunately, this step was not straightforward since we quickly discovered that there were stray pulses within the pulse shaping apparatus itself that were obscuring our spectral interferometry measurements. A schematic illustration showing the two types of unwanted pulses is shown in fig. 4-18. The first type of unwanted pulse results from very weak crosstalk between shaped regions $\mathbf{E}_a$, $\mathbf{E}_b$, $\mathbf{E}_c$ in the direction of the signal beam. An unwanted pulse occurred at time zero. All of these stray pulses interfered within the spectrometer and obscured the desired signal. In general, these third-order signals are quite small, such that even weak stray pulses that are 1/1000 of the input pulses are still on order with or larger than the measured nonlinear signals.

Note that the time-integrated heterodyned measurements on diiodomethane in

section 4.5.1 were not found to be sensitive to the crosstalk or t=0 peaks. That is because the stray peaks will only interfere with the local oscillator pulse when they are within their coherence length (i.e. when the pulses overlap, assuming bandwidth-limited pulses)—otherwise they will add incoherently, giving rise to a constant background signal that does not adversely affect the measurements. Considering the pulse sequence for the diiodomethane measurements, which was two time-coincident pump pulses followed by time-coincident probe and LO pulses, the only times at which a stray pulse would occur are at time zero or at the time of the probe pulse. At time zero, there there is already an unavoidable nonresonant electronic response, and so an additional distortion there is not a cause for concern. A possible stray pulse at the time of the probe would be shifted temporally but with a fixed phase relative to the LO pulse, leading to a constant term for all delays. Therefore, the heterodyned-transient grating measurements were insensitive to the stray pulses.
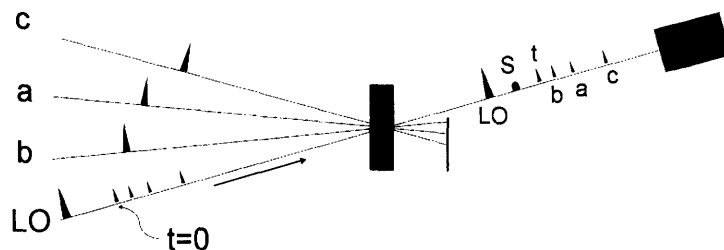
Figure 4-18: . Schematic illustration of weak stray pulses in the direction of the LO pulse that distort the spectral interferometry measurements. Pulses a, b, and c are the three input fields that generate the outgoing signal S. In this case, the detector (det.) is a spectrometer.

The reason why the stray pulses cause troubles when using spectral interferometry is that the duration of the pulses *within the spectrometer* are very long. The duration of a pulse at the spectral plane of a spectrometer is roughly the reciprocal of the spectral resolution—on the order of 10 ps for the spectrometer we used. This means that pulses within the 10 ps window will interfere, causing distortions to the desired signals. Fortunately, we can apply phase cycling methods borrowed from multidimensional NMR in order to isolate the interference terms of interest.

In the case when there are no stray pulses, the intensity $I_{det}(\omega)$ recorded by the

spectrometer is given by

$$I(\omega) \propto |E_{LO}(\omega)\exp[i\phi_{LO}(\omega)] + E_a(\omega)E_b(\omega)E_c(\omega)\exp[i\phi_a(\omega)]\exp[i\phi_b(\omega)]\exp[-i\phi_c\omega]|^2$$

$$\propto I_{LO}(\omega) + I_s(\omega) + 2\sqrt{I_s(\omega)I_{LO}(\omega)}\cos(\phi_{LO} - \phi_a(\omega) - \phi_b(\omega) + \phi_c(\omega)). \quad (4.29)$$

When there are stray pulses, many additional cross terms will be produced, but none of them has the same phase dependence on the main three input pulses and local oscillator pulse as the desired cross term in eq. 4.29. The phase dependence of the various terms is indicated in shorthand form in eq. 4.30, where the last term is the one which we seek to isolate.

$$I(\phi_{LO}, \phi_a, \phi_b, \phi_c)$$

$$\propto |A_{LO}e^{i\phi_{LO}} + A_s e^{i\phi_s} + A_a e^{i\phi_a} + A_b e^{i\phi_b} + A_c e^{i\phi_c} A_{t0} e^{i\phi_{t0}}|^2$$

$$\propto A_{LO}^2 + A_s^2 + A_a^2 + A_b^2 + A_c^2 + A_{t0}^2$$

$$+ 2A_{LO}A_{t0}\cos(\phi_{LO} - \phi_{t0}) + 2A_S A_{t0}\cos(\phi_S - \phi_{t0}) + 2A_a A_{t0}\cos(\phi_a - \phi_{t0})$$

$$+ 2A_b A_{t0}\cos(\phi_b - \phi_{t0}) + 2A_c A_{t0}\cos(\phi_c - \phi_{t0}) + 2A_L A_c\cos(\phi_L - \phi_c)$$

$$+ 2A_S A_c\cos(\phi_S - \phi_c) + 2A_a A_c\cos(\phi_a - \phi_c) + 2A_b A_c\cos(\phi_b - \phi_c)$$

$$+ 2A_{LO}A_b\cos(\phi_{LO} - \phi_b) + 2A_S A_b\cos(\phi_S - \phi_b) + 2A_a A_b\cos(\phi_a - \phi_b)$$

$$+ 2A_{LO}A_a\cos(\phi_{LO} - \phi_a) + 2A_S A_a\cos(\phi_S - \phi_a) + 2A_{LO}A_S\cos(\phi_{LO} - \phi_a - \phi_b + \phi_c)$$

$$(4.30)$$

The basic approach is to perform multiple measurements where the phases of the input pulses have been varied for each measurement, and then to combine the measurements such that the unwanted terms disappear. If subtract from the first "measurement" given in eq. 4.30 a measurement in which the phase of the pulse E_a (which controls the phase of the stray light A_s) is shifted by π, we obtain

157

$$I_1(\phi_{LO}, \phi_a, \phi_b, \phi_c) \equiv I(\phi_{LO}, \phi_a, \phi_b, \phi_c) + I(\phi_{LO}, \phi_a + \pi, \phi_b, \phi_c)$$

$$= 4A_S A_{t0} \cos(\phi_S - \phi_{t0}) + 4A_a A_{t0} \cos(\phi_a - \phi_{t0}) + 4A_S A_c \cos(\phi_S - \phi_c)$$

$$+ 4A_a A_c \cos(\phi_a - \phi_c) + 4A_S A_b \cos(\phi_S - \phi_b) + 4A_a A_b \cos(\phi_a - \phi_b)$$

$$+ 4A_{LO} A_a \cos(\phi_{LO} - \phi_a) + 4A_{LO} A_S \cos(\phi_{LO} - \phi_a - \phi_b + \phi_c). \qquad (4.31)$$

Note that the effect of this procedure is the elimination of terms not dependent upon the phase of pulse E_a. This may be repeated with two more measurements to eliminate all terms not dependent upon the phase of pulse E_b, and then four more measurements to eliminate all terms not dependent upon E_LO, which then isolates the term of interest. This set of 8 measurements, in three stages, would be written as:

$$I_1 \equiv I(\phi_{LO}, \phi_a, \phi_b, \phi_c) - I(\phi_{LO}, \phi_a + \pi, \phi_b, \phi_c)$$

$$I_2 \equiv I_1(\phi_{LO}, \phi_a, \phi_b, \phi_c) - I_1(\phi_{LO}, \phi_a, \phi_b + \pi, \phi_c)$$

$$I_3 \equiv I_2(\phi_{LO}, \phi_a, \phi_b, \phi_c) - I_2(\phi_{LO} + \pi, \phi_a, \phi_b, \phi_c)$$

$$= 16 A_{LO} A_S \cos(\phi_{LO} - \phi_a - \phi_b + \phi_c). \qquad (4.32)$$

A simulation of such a phase-cycling process is included in fig. 4-19. The first plot, (a), shows a series of spectral interferograms as a function of the delay of the LO. A complicated set of interference fringes is observed. After each phase-cycling stage, the unwanted signal contributions diminish. Finally in (d), 8 measurements have been combined, yielding the expected pattern for a signal field emitted at a time of 1.3 ps that interferes with a variably delayed reference pulse. The fringe spacing (along the vertical dimension)is inversely proportional to the temporal separation of the two pulses that interfere. When the two pulses overlap, the fringes disappear, leaving a single large feature, as can be seen for a LO delay of 1.3 ps. In experiments, it is not necessary to scan the LO pulse in time, although we have found the LO

158
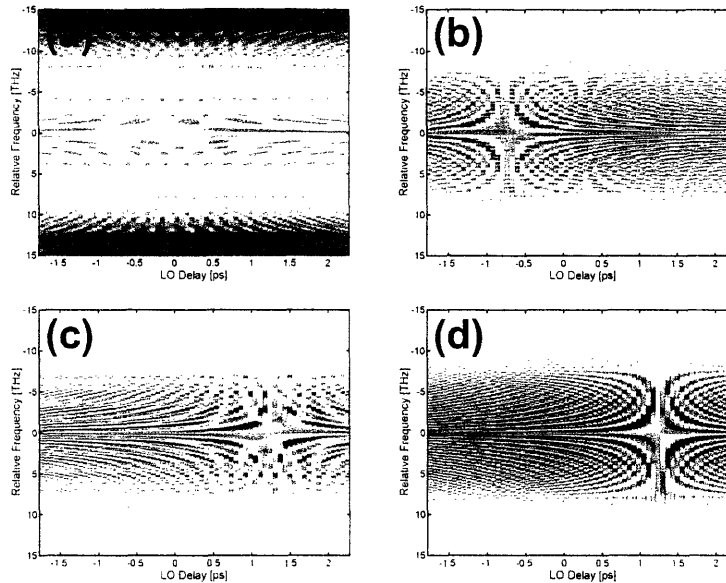
Figure 4-19: Simulation of LO scans, illustrating how phase-cycling can be used to eliminate spurious signals that are not dependent on the phase of all beams. (a) Original interferogram, no phase cycles. (b) Two phase cycles. (c) Four phase cycles. (d) Eight phase cycles, yielding the correct signal free of distortions

delay scans to be useful when investigating the effects of the unwanted pulses due to cross talk, etc. A single spectral interferogram recorded for a given LO delay can provide all the necessary information to characterize the emitted signal field. Eight cycles are sufficient to isolate the third-order nonlinear optical signal from spurious pulses, provided that the spurious pulses are only dependent upon the phase of a single input pulse (i.e. not a nonlinear signal of a different order). Related phase cycling schemes can be used to discriminate between nonlinear signals of a different order (i.e. separate $5^{t}h$ order response from 3rd order response).

Figure 4-20 shows two stages of the phase cycling process used in preliminary experiments. For the photon-echo pulse sequence shown in (a), the time-integrated signal in (b) was obtained as a function of τ_2, with τ_1 held constant at 0.54 ps. An arrow in (b) points to a specific peak in the time-integrated signal ($\tau_2 = 1$ ps) which we investigated with several phase-cycled LO scans. The LO scan shown in (c) has already been through the first step of the phase cycling process (two combined measurements). There are broad features centered at a time of about 1.5 ps, the

159

position at which the echo signal is expected, as well as smaller features that originate from the insidious t=0 pulse. Repeating the phase cycling operation performed in (c) (a single phase cycle) with one of the non-cycled phases flipped by π causes the interference fringes to flip in sign, as can be seen in (e). The difference between (c) and (e) is plotted in (d), where the smaller features originating from t=0 have been eliminated and the expected interference pattern is much clearer. Thus, (d) constitutes is a spectrum that has been through two stages of the phase cycling process (4 measurements). When the measurement in (d) is repeated but with one of the non-cycled phases flipped by π, the sign of the interference fringes is switched. The difference between (d) and (f) would then constitute the full three stages of phase cycling (total of 8 measurements).
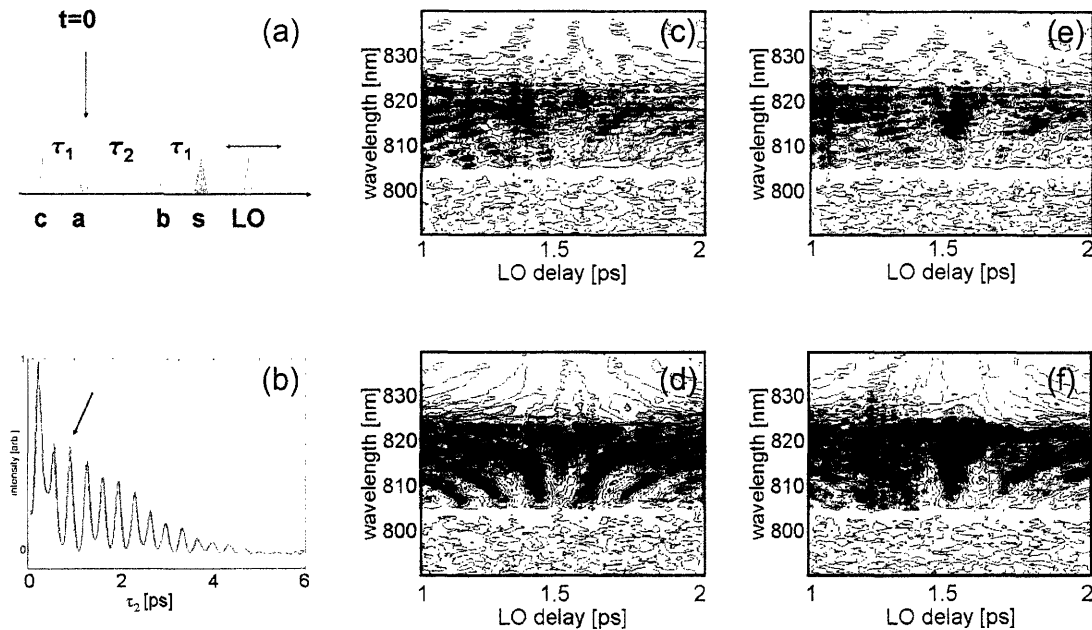
Figure 4-20: (a) Photon-echo pulse sequence. For τ_1=0.54 ps, τ_2 is scanned in time, yielding the transient in (b). For a fixed value of τ_2=1 ps [see arrow in (b)], LO scans were recorded for varying amounts of phase-cycling (c)-(f).

A second set of LO scans is shown in fig. 4-21, where this time, the delay is set to τ_2=1.3 ps [which, again, corresponds to a peak in the time-integrated photon-echo signal (b)]. As expected, the peak of the echo signal has shifted in time to about 1.85 ps (c)-(d). It is worth noting that the fringes observed in figures 4-20 and 4-21

160

do not have an overall tilt to them, as would happen if mechanical or refractive delay lines were used because these delay methods shift both carrier phase and envelope. Since 800 nm light has a period of about 2.7 fs, there would be about 370 tightly-spaced fringes running diagonally across the 1 ps LO scans in the LO scans of fig. 4-20 and 4-21. By using the pulse shaper to shift the envelope of the pulse without shifting the phase, it is not necessary to resolve oscillations of the carrier phase. The same principles apply for regular 2D scans, not just the LO scan. Also note that there a are a few instances where dark vertical lines appear in the data [i.e. at 1.5 ps and 1.7 ps in fig. 4-21 (c)]. These dark lines resulted from unusually large fluctuations in the laser power due to a faulty chiller unit that has since been repaired.
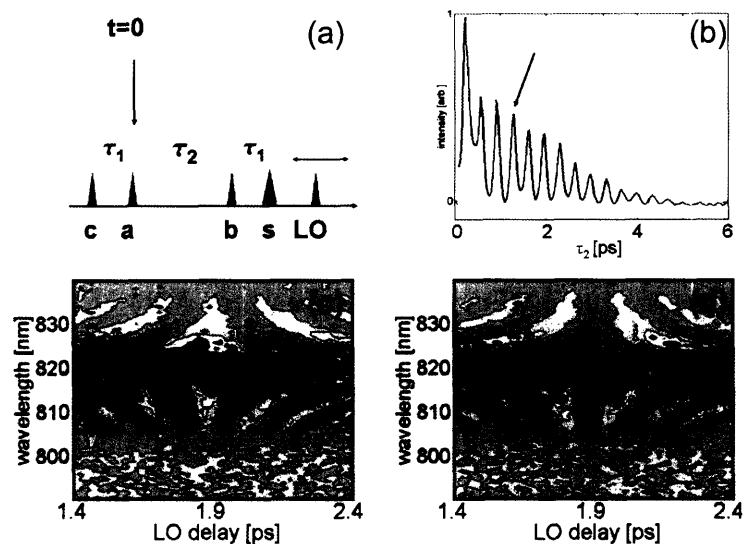
Figure 4-21: . (a) Photon-echo pulse sequence. For τ_1=0.54 ps, τ_2 is scanned in time, yielding the transient in (b). When τ_2 is set to be 1.3 ps [see arrow], the observed phase-cycled signal shifts to the expected time at about 1.85 ps (c),(d). Two sets of phase cycling (four measurements) were used in each of (c) and (d).

4.6 Conclusion and Outlook

A powerful new approach to coherent nonlinear optical spectroscopy has been proposed and demonstrated. Signals may be selected on the basis of input beam wavevector, input pulse timings, input pulse spectral content, signal phase dependence,

161

carrier-free interferometric detection, etc. As such the methodology combines aspects of optical nonlinear spectroscopy with aspects of 2D NMR spectroscopy.

Near term goals include further elaboration of the above capabilities on rubidium vapor and potassium dimer molecules. A collaboration is under way with the group of Steve Cundiff at JILA in Boulder, CO to study biexciton dynamics and disorder effects in semiconductor quantum well structures, which also have resonances within the bandwidth of our laser. A noncollinear optical parametric amplifier capable of 20 fs pulses in the range 450-700 nm is currently being built, such that we may extend the experimental approach out to the visible region of the spectrum where molecular aggregates and carotenoid systems provide some of the most interesting possibilities for investigation. The future is bright for 2D optical spectroscopy.

4.7 Appendix: Principles for Constructing Feynman Diagrams

The principles for constructing Feynman diagrams are reproduced here in modified form from chapter 6 of reference [21].

1. A diagram represents a *particular quantum pathway* along which the system may evolve that contributes to an emitted signal. All possible pathways (i.e. all valid diagrams) for a given pulse sequence must be included in order to determine the full response of the system.

2. The two vertical lines represent the ket (left line) and bra (right line) of the density matrix. Temporal evolution is represented from the bottom to the top. During each time increment t_n separating successive system-field interactions, the system is in the state $|l\rangle\langle m|$ and accumulates a factor of $\exp(i\Omega_{lm}t_n)$. In many cases, damping is introduced phenomenologically via $\Omega_{lm} \equiv \omega_{lm} + i\Gamma_{lm}$. When l=m, the term Γ_{mm} represents the reciprocal of the lifetime of the density matrix population $|m\rangle\langle m|$, and when $l \neq m$, Γ_{lm} represents the reciprocal of the dephasing time of the density matrix coherence $|l\rangle\langle m|$.

3. Each diagram carries a sign of $(-1)^n$, where n is the number of interactions on the right (bra) side. This overall sign is especially important to consider in cases when there are multiple diagrams that will be summed together.

4. Each interaction between the system and an incident field is represented by an arrow. These arrows point either up and to the right or up and to the left. An arrow pointing towards the diagram represents absorption while an arrow pointing away from the diagram represents emission.

5. Arrows that have a right tilt are contribute a term of $\exp[-i(\phi_a(t) - \mathbf{k}_a\mathbf{r})]$ to the emitted signal. Arrows that have a left tilt contribute a term of $\exp[i(\phi_a(t) - \mathbf{k}_a\mathbf{r})]$ to the emitted signal. The overall wavevector and phase of the signal contribution associated with each diagram is the sum of the input wavevectors and phases. These considerations arise out of the rotating wave approximation implicit in the diagrams.

6. Each interaction between the field and the system on the ket side contributes a factor of μ_{lm} to the magnitude of the diagram, where $|l\rangle$ and $|m\rangle$ are the initial and final states. Interactions on the bra side contribute a factor of $\mu_{lm}*$.

7. By convention, the last arrow always points left from the ket side, representing emission of the signal. Its wavevector and phase are given by the sums of the wavevectors and phases of all preceding arrows.

8. Diagrams must end in a population, ρ_{mm}, by virtue of the trace operation. Furthermore, the diagram (almost) always starts in a population.

9. Consideration of the strength of the relevant transition dipole moments as well as the width of the laser spectrum relative to the transitions between the system's eigenstates can help avoid writing out unnecessary diagrams.

10. For DFWM spectroscopy, two arrows will tilt left and two arrows will tilt right. Of the first three arrows, the left-tilting arrow represents the interaction with *conjugate field.*

11. The full response of the system is twice the real part of the sum of all valid diagrams.

SI   SII   SIII

τ_3
τ_2
τ_1

	0X0			0X0			0X0			0X0			0X0			1X1	
	1X0			1X0			1X0			1X0			1X0			3X1	
	1X1			0X0			1X1			1X1			3X0			3X0	
	0X1			0X1			1X0			1X0			1X0			1X0	
	0X0			0X0			0X0			0X0			0X0			0X0	

R_1 R_2 R_3 R_4 R_{25} R_{26}

	0X0			0X0			0X0			0X0			0X0			2X2	
	2X0			2X0			2X0			2X0			2X0			3X2	
	2X2			0X0			0X0			2X2			3X0			3X0	
	0X2			0X2			2X0			2X0			2X0			2X0	
	0X0			0X0			0X0			0X0			0X0			0X0	

R_5 R_6 R_7 R_8 R_{27} R_{28}

	0X0			0X0			0X0			0X0			0X0			2X2	
	2X0			2X0			2X0			1X0			2X0			3X2	
	2X1			0X0			0X0			1X2			3X0			3X0	
	0X1			0X1			1X0			1X0			1X0			1X0	
	0X0			0X0			0X0			0X0			0X0			0X0	

R_9 R_{10} R_{11} R_{12} R_{29} R_{30}

	0X0			0X0			0X0			0X0			0X0			1X1	
	1X0			1X0			1X0			2X0			1X0			3X1	
	1X2			0X0			0X0			2X1			3X0			3X0	
	0X2			0X2			2X0			2X0			2X0			2X0	
	0X0			0X0			0X0			0X0			0X0			0X0	

R_{13} R_{14} R_{15} R_{16} R_{31} R_{32}

	1X1			2X2			1X1			2X2	
	3X1			3X2			3X1			3X2	
	1X1			2X2			1X1			2X2	
	0X1			0X2			1X0			2X0	
	0X0			0X0			0X0			0X0	

R_{17} R_{18} R_{19} R_{20}

|3> ————

	1X1			2X2			1X1			2X2	
	3X1			3X2			3X1			3X2	
	2X1			2X2			2X1			1X2	
	0X1			0X2			2X0			1X0	
	0X0			0X0			0X0			0X0	

R_{21} R_{22} R_{23} R_{24}

|2> ————
|1> ————

|0> ————

Figure 4-22: All 32 Feynman diagrams for DFWM spectroscopy on four-level systems resembling the Rb atom (level structure, lower right) that are initially in the ground state. The diagrams are grouped into SI (photon echo) diagrams, SII (transient grating) diagrams, and SIII (other) diagrams. Note the timing of the interaction between the system and the conjugate field in each group: for SI the conjugate field interacts first; for SII the conjugate field interacts second; and for SIII the conjugate field interacts third.

Bibliography

[1] G. Hayafus, *Stopping Time: The Photographs of Harold Edgerton* (Harry N. Abrams, Inc., New York, 1987).

[2] M. Dantus, M. Rosker, A. Zewail, "Real-time femtosecond probing of "transition states" in chemical reactions", *J. Chem. Phys.* **87**, 2395–2397 (1987).

[3] M. Khalil, N. Demirdoven, A. Tokmakoff, "Coherent 2D IR Spectroscopy: Molecular Structure and Dynamics in Solution", *J. Phys. Chem. A* **107**, 5258–5279 (2003).

[4] R. Ernst, G. Bodenhausen, A. Wokaun, *Principles of nuclear magnetic resonance in one and two dimensions* (Oxford University Press, Oxford, 1987).

[5] H. Chung, M. Khalil, A. Smith, Z. Ganim, A. Tokmakoff, "Conformational changes during the nanosecond-to-millisecond unfolding of ubiquitin", *Proc. Nat. Acad. Sci.* **102**, 612–617 (2005).

[6] A. Weiner, D. Leaird, G. Wiederrecht, K. Nelson, "Femtosecond pulse sequences used for optical manipulation of molecular motion", *Science* **247**, 1317–1319 (1990).

[7] T. Weinacht, J. Ahn, P. Bucksbaum, "Controlling the shape of a quantum wavefunction", *Nature* **397**, 2783–2791 (1999).

[8] D. Meshulach, Y. Silberberg, "Coherent quantum control of two-photon transitions by a femtosecond laser pulse", *Nature* **396**, 239–242 (1998).

[9] N. Dudovich, B. Dayan, S. Faeder, Y. Silberberg, "Transform-Limited Pulses Are Not Optimal for Resonant Multiphoton Transitions", *Phys. Rev. Lett.* **86**, 47–50 (2001).

[10] J. Gupta, R. Knobel, N. Samarth, D. Awschalom, "Ultrafast Manipulation of Electron Spin Coherence", *Science* **292**, 2458–2461 (2001).

[11] A. Assion, T. Baumert, M. Bergt, T. Brixner, B. Kiefer, V. Seyfried, M. Strehle, G. Gerber, "Control of Chemical Reactions by Feedback-Optimized Phase-Shaped Femtosecond Laser Pulses", *Science* **282**, 919–922 (1998).

[12] R. Levis, G. Menkir, H. Rabitz, "Selective Bond Dissociation and Rearrangement with Optimally Tailored, Strong-Field Laser Pulses", *Science* **292**, 709–713 (2001).

[13] C. Daniel, J. Full, L. Gonzales, C. Lupulescu, J. Manz, A. Merli, S. Vajda, L. Woste, "Deciphering the Reaction Dynamics Underlying Optimal Control Laser Fields", *Science* **299**, 536–539 (2003).

[14] J. Herek, W. Wohlleben, R. Cogdell, D. Zeidler, M. Motzkus, "Quantum control of energy flow in light harvesting", *Nature* **417**, 533–535 (2002).

[15] N. Dudovich, D. Oron, Y. Silberberg, "Single-pulse coherently controlled nonlinear Raman spectroscopy and microscopy", *Nature* **418**, 512–514 (2002).

[16] S. Rice, M. Zhao, *Optical Control of Molecular Dynamics* (John Wiley and Sons, New York, 2000).

[17] M. Shapiro, P. Brumer, *Principles of the Quantum Control of Molecular Processes* (Wiley-Interscience, New Jersey, 2003).

[18] C. Kittel, *Introduction to Solid State Physics* (John Wiley and Sons, Inc., New York, 1996).

[19] I. Inbar, R. Cohen, "Electronic-structure studies of the differences in ferroelectric behavior of BaTiO3 and PbTiO3", *Phys. Rev. B* **53**, 1193–1204 (1996).

[20] D. Jonas, "Two-Dimensional Femtosecond Spectroscopy", *Annu. Rev. Phys. Chem.* **54**, 425–463 (2003).

[21] S. Mukamel, *Principles of Nonlinear Optical Spectroscopy* (Oxford University Press, Oxford, 1995).

[22] C. Froehly, B. Colombeau, M. Vampouille, *Progress in Optics, ed. E. Wolf*, vol. 20, 65–153 (North-Holland, Amsterdam, 1983).

[23] M. Haner, W. Warren, "Generation of arbitrarily shaped picoseond optical pulses using an integrated electrooptic wave-guide modulator", *Appl. Opt.* **26**, 3687–3694 (1987).

[24] A. Weiner, "Femtosecond pulse shaping using spatial light modulators", *Rev. Sci. Instr.* **71**, 1929–1969 (2000).

[25] J. Heritage, R. Thurston, W. Tomlinson, A. Weiner, R. Stolen, "Spectral windowing of frequency-modulated optical pulses in a grating compressor", *Appl. Phys. Lett.* **47**, 87–89 (1985).

[26] J. Tull, M. Dugan, W. Warren, "High resolution, ultrafast laser pulse shaping and its applications", *Adv. Magn. Opt. Reson.* **20**, 1–56 (1997).

[27] E. Zeek, K. Maginnis, S. Backus, U. Russek, M. Murnane, G. Mourou, H. Kapteyn, G. Vdovin, "Pulse compression by use of deformable mirrors", *Opt. Lett.* **24**, 493–495 (1999).

[28] D. Leaird, A. Weiner, "Femtosecond optical packet generation by a direct space-to-time pulse shaper", *Opt. Lett.* **24**, 853–855 (1999).

[29] K. Hill, K. Purchase, D. Brady, "Pulsed-image generation and detection", *Opt. Lett.* **290**, 1201–1203 (1995).

[30] F. Verluise, V. Laude, J. Huignard, P. Tournois, "Arbitrary dispersion control of ultrashort optical pulses with acoustic waves", *J. Opt. Soc. Am. B* **17**, 138–145 (2000).

[31] M. Wefers, K. Nelson, "Analysis of programmable ultrashort waveform generation using liquid-crystal spatial light modulators", *J. Opt. Soc. Am. B* **12**, 1343–1362 (1995).

[32] N. Karasawa, L. Li, A. Suguro, H. Shigekawa, R. Morita, M. Yamashita, "Optical pulse compression to 5.0 fs by use of only a spatial light modulator for phase compensation", *J. Opt. Soc. Am. B* **18**, 1742–1746 (2001).

[33] H. Saradesai, C.-C. Chang, A. Weiner, "A Femtosecond Code-Division Multiple-Access Communication System Test Bed", *L. Lightwave Technol.* **16**, 1953–1964 (1998).

[34] F. Huang, W. Yang, W. Warren, "Quadrature spectral interferometric detection and pulse shaping", *Opt. Lett.* **26**, 362–364 (2001).

[35] M. Wefers, K. Nelson, A. Weiner, "Multidimensional shaping of ultrafast optical waveforms", *Opt. Lett.* **21**, 1–3 (1996).

[36] M. Nuss, R. Morrison, "Time-domain images", *Opt. Lett.* **20**, 740–742 (1995).

[37] R. Koehl, T. Hattori, K. Nelson, "Automated spatial and temporal shaping of femtosecond pulses", *Opt. Commun.* **157**, 57–61 (1998).

[38] T. Feurer, J. Vaughan, R. Koehl, K. Nelson, "Multidimensional control of femtosecond pulses by use of a programmable liquid crystal matrix", *Opt. Lett.* **27**, 652–654 (2002).

[39] J. Vaughan, T. Feurer, K. Nelson, "Automated two-dimensional femtosecond pulse shaping", *J. Opt. Soc. Am. B* **19**, 2489–2495 (2002).

[40] J. Vaughan, T. Feurer, K. Nelson, "Automated spatiotemporal diffraction of ultrashort laser pulses", *Opt. Lett.* **28**, 2408–2410 (2003).

[41] J. Vaughan, T. Hornung, T. Feurer, K. Nelson, "Diffraction-based femtosecond pulse shaping with a 2D SLM", *Opt. Lett.* **30**, 323–325 (2005).

[42] M. Wefers, K. Nelson, "Generation of high-fidelity programmable ultrafast optical waveforms", *Opt. Lett.* **20**, 1047–1049 (1995).

[43] T. Brixner, G. Gerber, "Femtosecond polarization pulse shaping", *Opt. lett.* **26**, 557–559 (2001).

[44] T. Brixner, G. Krampert, P. Niklaus, G. Gerber, "Generation and characterization of polarization-shaped femtosecond laser pulses", *Appl. Phys. B* **74**, S133–S144 (2002).

[45] T. Brixner, "Poincare representation of polarization-shaped femtosecond laser pulses", *Appl. Phys. B* **76**, 531–540 (2003).

[46] T. Brixner, N. Damrauer, G. Krampert, P. Niklaus, G. Gerber, "Adaptive shaping of femtosecond polarization profiles", *J. Opt. Soc. Am. B* **20**, 878–881 (2003).

[47] T. Brixner, W. Pfeiffer, F. J. G. de Abajo, "Femtosecond shaping of transverse and longitudinal light polarization", *Opt. Lett.* **29**, 2187–2189 (2004).

[48] D. Oron, N. Dudovich, Y. Silberberg, "Femtosecond Phase-and-Polarization Control for Background- Free Coherent Anti-Stokes Raman Spectroscopy", *Phys. Rev. Lett.* **90**, 213902 (2003).

[49] N. Dudovich, D. Oron, Y. Silberberg, "Quantum Control of the Angular Momentum Distribution in Multiphoton Absorption Processes", *Phys. Rev. Lett.* **92**, 103003 (2004).

[50] T. Suzuki, S. Minemoto, T. kanai, H. Sakai, "Optimal Control of Multiphoton Ionization Processes in Aligned I2 Molecules with Time-Dependent Polarization Profiles", *Phys. Rev. Lett.* **92**, 133005 (2004).

[51] T. Brixner, G. Krampert, W. Pfeiffer, R. Selle, G. Gerber, "Quantum Control by Ultrafast Polarization Shaping", *Phys. Rev. Lett.* **92**, 208301 (2004).

[52] C. Dorrer, F. Salin, F. Verluise, J. Huignard, "Programmable phase control of femtosecond pulses by use of a nonpixelated spatial light modulator", *Opt. Lett.* **23**, 709–711 (1998).

[53] A. Efimov, C. Schaffer, D. Reitze, "Programmable shaping of ultrabroad-bandwidth pulses from a Ti:sapphire laser", *J. Opt. Soc. Am. B* **12**, 1969–1979 (1995).

[54] G. Stobrawa, M. Hacker, T. Feurer, D. Zeidler, M. Motzkus, F. Reichel, "A new high-resolution femtosecond pulse shaper", *Appl. Phys. B* **72**, 627–630 (2001).

[55] L. Wang, A. Weiner, "Programmable spectral phase coding of an unamplified spontaneous emission light source", *Opt. Commun.* **167**, 211–224 (1999).

[56] H. Wang, Z. Zheng, D. Leaird, A. Weiner, T. Dorschner, J. Fijol, L. Friedman, H. Nguyen, L. Palmaccio, "20-fs Pulse Shaping With a 512-Element Phase-Only Liquid Crystal Modulator", *IEEE J. Sel. Top. Quant. Elec.* **7**, 718–727 (2001).

[57] A. Rundquist, A. Efimov, D. Reitze, "Pulse shaping with the Gerchberg-Saxton algorithm", *J. Opt. Soc. Am. B* **19**, 2468–2478 (2002).

[58] C. Iaconis, I. Walmsley, "Spectral phase interferometry for direct electric-field reconstruction of ultrashort optical pulses", *Opt. Lett.* **23**, 792–794 (1998).

[59] R. Trebino, K. DeLong, D. Fittinghoff, J. Sweetser, M. Krumbugel, B. Richman, "Measuring ultrashort laser pulses in the time-frequency domain using frequency-resolved optical gating", *Rev. Sci. Instr.* **68**, 3277–3295 (1997).

[60] D. Fittinghoff, J. Bowie, J. Sweetser, R. Jennings, M. Krumbugel, K. Delong, R. Trebino, "Measurement of the intensity and phase of ultraweak, ultrashort laser pulses", *Opt. Lett.* **21**, 884–886 (1996).

[61] W. Walecki, D. Fittinghoff, A. Smirl, R. Trebino, "Characterization of the polarization state of weak ultrashort coherent signals by dual-channel spectral interferometry", *Opt. Lett.* **22**, 81–83 (1997).

[62] P. O'shea, M. Kimmel, X. Gu, R. Trebino, "Highly simplified device for ultrashort-pulse measurement", *Opt. lett.* **26**, 932–934 (2001).

[63] J. Nicholson, J. Jasapara, W. Rudolph, F. Omenetto, A. Taylor, "Characterization of femtosecond pulses by spectrum and cross-correlation measurements", *Opt. Lett.* **24**, 1774–1776 (1999).

[64] J.-K. Rhee, T. Sosnowski, T. Norris, J. Arns, W. Colburn, "Chirped-pulse amplification of 85-fs pulses at 250 kHz with third-order dispersion compensation by use of holgraphic transmission gratings", *Opt. Lett.* **19**, 1550–1552 (1994).

[65] L. Lepetit, G. Cheriaux, M. Joffre, "Linear techniques of phase measurement by femtosecond spectral interferometry for applications in spectroscopy", *J. Opt. S oc. Am. B* **12**, 2467–2474 (1995).

[66] C. Dorrer, N. Belabas, j.P. Likforman, M. Joffre, "Spectral resolution and sampling issues in Fourier-transform spectral interferometry", *J. Opt. Soc. Am. B* **17**, 1795–1802 (2000).

[67] A. Weiner, D. Leaird, J. Patel, J. Wullert, "Programmable Shaping of Femtosecond Optical Pulses by Use of 128-Element Liquid Crystal Phase Modulator", *IEEE J. Quant. Elec.* **28**, 908–920 (1992).

[68] T. Hornung, J. Vaughan, T. Feurer, K. Nelson, "Degenerate four-wave mixing spectroscopy based on two-dimensional femtosecond pulse shaping", *Opt. Lett.* **29**, 2052–2054 (2004).

[69] M. Wefers, K. Nelson, "Space-Time Profiles of Shaped Ultrafast Optical Waveforms", *IEEE J. Quant. Elec.* **32**, 161–172 (1996).

[70] M. Hacker, G. Stobrawa, T. Feurer, "Iterative Fourier transform algorithm for phase-only pulse shaping", *Opt. Express* **9**, 191–199 (2001).

[71] J. Goodman, *Introduction to Fourier Optics* (McGraw-Hill, Inc., San Francisco, 1968).

[72] S. Lee, *Selected Papers on Computer-Generated holograms and Diffractive Optics* (SPIE Optical Engineering Press, Bellingham, Washington, 1992).

[73] L. Romero, F. Dickey, "Lossless laser beam shaping", *J. Opt. Soc. Am. A* **13**, 751–760 (1996).

[74] F. Dickey, S. Holswade, "Gaussian laser beam profile shaping", *Opt. Eng.* **35**, 3285–3295 (1996).

[75] V. Soifer, V. Kotlyar, *Iterative methods for diffractive optical elements computation* (Taylor and Francis, London, 1997).

[76] R. Gerchberg, W. Saxton, "A Practical Algorithm for the Determination of Phase from Image and Diffraction Plane Pictures", *Optik* **35**, 237 (1971).

[77] A. W. S. Oudin, D. Leaird, D. Reitze, "Shaping of femtosecond pulses using phase-only filters designed by simulated annealing", *J. Opt. Soc. Am. B* **10**, 1112–1120 (1993).

[78] T. Baumert, B. T, V. Seyfried, M. Strehle, G. Gerber, "Femtosecond pulse shaping by an evolutionary algorithm with feedback", *Appl. Phys. B* **65**, 779–782 (1997).

[79] D. Meshulach, D. Yelin, Y. Silberberg, "Adaptive real-time femtosecond pulse shaping", *J. Opt. Soc. Am. B* **15**, 1615–1619 (1998).

[80] E. DeSouza, M. Nuss, W. Knox, D. Miller, "Wavelength-division multiplexing with femtosecond pulses", *Opt. Lett.* **20**, 1166–1168 (1995).

[81] J. Ford, V. Aksyuk, D. Bishop, J. Walker, "Wavelength Add-Drop Switching Using Tilting Micromirrors", *J. Lightwave Technol.* **17**, 904–911 (1999).

[82] J. Patel, Y. Silberberg, "Liquid Crystal and Grating-Based Multiple-Wavelength Cross-Connect Switch", *IEEE Photon. Technol. Lett.* **7**, 516–516 (1995).

[83] K. Tan, W. Crossland, R. Mears, "Dynamic holography for optical interconnec-
tions. I. Noise floor of low-cross-talk holographic switches", *J. Opt. Soc. Am. B*
18, 195–204 (2001).

[84] K. Tan, S. Warr, I. Manolis, T. Wilkinson, M. Redmond, W. Crossland,
R. Mears, B. Robertson, "Dynamic holography for optical interconnections. II.
Routing holograms with predictable location and intensity of each diffraction
order", *J. Opt. Soc. Am. B* **18**, 205–215 (2001).

[85] M. Hacker, G. Stobrawa, R. Sauerbrey, T. Buckup, M. Motzkus, M. Wildenhain,
A. Gehner, "Micromirror SLM for femtosecond pulse shaping in the ultraviolet",
Appl. Phys. B **76**, 711–714 (2003).

[86] J. James, *A Student's Guide to Fourier Transforms* (Cambridge University
Press, Cambridge, 1995).

[87] B. Saleh, M. Teich, *Fundamentals of Photonics* (John Wiley and Sons, Inc.,
New York, 1991).

[88] D. Auston, K. Cheung, J. Valdamis, D. Kleinman, "Cherenkov Radiation from
Femtosecond Optical Pulses in Electro-Optic Media", *Phys. Rev. Lett.* **53**, 1555–
1558 (1984).

[89] D. You, R. Jones, D. Dykaar, P. Bucksbaum, "Generation of High-power Half-
Cycle 500 Femtosecond Electromagnetic Pulses", *Opt. Lett.* **18**, 290–292 (1993).

[90] R. Cheville, D. Grishkowsky, "Far-infrared terahertz time-domain spectroscopy
of flames", *Opt. Lett.* **30**, 1646–1648 (1995).

[91] B. Hu, M. Nuss, "Imaging with terahertz waves", *Opt. Lett.* **20**, 1716–1718
(1995).

[92] M. Brucherseifer, M. Nagel, P. Bolivar, H. Kurz, A. Bosserhoff, R. Buttner,
"Label-free probing of the binding state of DNA by time-domain terahertz sens-
ing", *Appl. Phys. Lett.* **77**, 4049 (2000).

[93] P. Tamborenea, H. Metiu, "Coherent control of multisubband wavepackets with terahertz (THz) pulses", *J. Chem. Phys.* **110**, 9202–9213 (1999).

[94] N. Stoyanov, D. Ward, T. Feurer, K. Nelson, "Terahertz polariton propagation in patterned materials", *Nature Materals* **1**, 95–98 (2002).

[95] C. Flytzanis, "Infrared Dispersion of Second-Order Electric Susceptibilities in Semiconducting Compounds", *Phys. Rev. B* **6**, 1264–1290 (1972).

[96] L. Xu, D. Auston, A. Hasegawa, "Propagation of electromagnetic solitary waves in dispersive nonlinear dielectrics", *Phys. Rev. A* **45**, 3184–3193 (1992).

[97] K. Okumura, Y. Tanimura, "Two-dimensional THz spectroscopy of liquids: non-linear vibrational response to a series of THz laser pulses", *Chem. Phys. Lett.* **4**, 298–304 (1998).

[98] U. Haberle, G. Diezemann, "Nonresonant holeburning in the Terahertz range: Brownian oscillator model", *J. Chem. Phys.* **120**, 1466–1476 (2004).

[99] C. Rangan, P. Bucksbaum, "Optimally shaped terahertz pulses for phase retrieval in Rydberg-atom data register", *Phys. Rev. A* **64**, 033417 (2001).

[100] T. Feurer, J. Vaughan, K. Nelson, "Spatiotemporal control of lattice vibrational waves", *Science* **299**, 374–377 (2003).

[101] T. Feurer, J. Vaughan, T. Hornung, K. Nelson, "Typesetting of terahertz waveforms", *Opt. Lett.* **29**, 1802–1804 (2004).

[102] A. Mayer, F. Keilmann, "Far-infrared nonlinear optics. I. Chi(2) near ionic resonance", *Phys. Rev. B* **33**, 6954–6961 (1986).

[103] A. Mayer, F. Keilmann, "Far-infrared nonlinear optics. II. Chi(3) contributions from the dynamics of free carriers in semiconductors", *Phys. Rev. B* **33**, 6962–6968 (1986).

[104] J. Cerne, J. Kono, T. Inoshita, M. Sherwin, M. Sundaram, A. Gossard, "Near-infrared sideband generation induced by intense far-infrared radiation in GaAs quantum wells", *Appl. Phys. Lett.* **26**, 3543 3545 (1997).

[105] J. Kono, M. Su, T. Inoshita, T. Noda, M. Sherwin, S. Allen, H. Sakaki, "Resonant Terahertz Optical Sideband Generation from Confined Magnetoexcitons", *Phys. Rev. Lett.* **79**, 1758 1761 (1997).

[106] C. Brennan, *Femtosecond Wavevector Overtone Spectroscopy of Anharmonic Lattice Dynamics in Ferroelectric Crystals*, Ph.D. thesis, Massachusetts Institute of Technology (1997).

[107] A. Barker, R. Loudon, "Response functions in the theory or Raman scattering by vibrational and polariton modes in dielectric crystals", *Rev. Mod. Phys.* **44**, 18 46 (1972).

[108] M. Born, K. Huang, *Dynamical Theory of Crystal Lattices* (Oxford, 1988).

[109] T. Dougherty, G. Wiederrecht, K. Nelson, "Impulsive stimulated Raman scattering experiments in the polariton regime", *J. Opt. Soc. Am. B* **9**, 2179 2189 (1992).

[110] D. Weard, *Polaritonics: An Intermediate Regime Between Electronics and Photonics*, Ph.D. thesis, Massachusetts Institute of Technology (2005).

[111] Y. Yan, K. Nelson, "Impulsive stimulated light scattering. I. General theory", *J. Chem. Phys.* **87**, 6240 6256 (1987).

[112] K. Nelson, E. Ippen, "Femtosecond Coherent Spectroscopy", *Adv. Chem. Phys.* **75**, 1 35 (1989).

[113] M. Wefers, H. Kawashima, K. Nelson, "Optical control over two-dimensional lattice vibrational trajectories in crystalline quartz", *J. Chem. Phys.* **108**, 10248 10255 (1998).

[114] R. Boyd, *Nonlinear Optics* (Academic Press, San Diego, 1992).

[115] A. Yariv, *Quantum Electronics* (John Wiley and Sons, New York, 1989).

[116] G. Settles, *Schlieren and Shadowgraph Techniques* (Springer, New York, 2001).

[117] R. Koehl, S. Adachi, K. Nelson, "Direct visualization of collective wavepacket dynamics", *J. Phys. Chem. A* **103**, 10260–10267 (1999).

[118] M. Wefers, H. Kawashima, K. Nelson, "Automated multidimensional coherent optical spectroscopy with multiple phase-related femtosecond pulses", *J. Chem. Phys.* **102**, 9133–9136 (1995).

[119] H. Kawashima, M. Wefers, K. Nelson, "Femtosecond pulse shaping, multiple-pulse spectroscopy, and optical control", *Ann. Rev. Phys. Chem.* **46**, 627–656 (1995).

[120] Y. Nakamura, Y. Pashkin, J. Tsai, "Coherent control of macroscopic quantum states in a single-Cooper-pair box", *Nature* **398**, 786–788 (1999).

[121] T. Crimmins, N. Stoyanov, K. Nelson, "Heterodyned impulsive stimulated Raman scattering of phonon-polaritons in LiTaO3 and LiNbO3", *J. Chem. Phys.* **117**, 2882–2896 (2002).

[122] M. Skolnik, *Introduction to Radar Systems* (McGraw-Hill, Boston, 2001).

[123] R. Koehl, K. Nelson, "Coherent optical control over collective vibrations traveling at lightlike speeds", *J. Chem. Phys. B* **114**, 1443–1446 (2001).

[124] R. Koehl, K. Nelson, "Terahertz polaritonics: Automated spatiotemporal control over propagating lattice waves", *Chem. Phys.* **267**, 151–159 (2001).

[125] E. D. Malacara, *Optical Shop Testing* (Wiley-Interscience, 1978).

[126] Y. Sohn, Y. Ahn, D. Park, E. Oh, D. Kima, "Tunable terahertz generation using femtosecond pulse shaping", *Appl. Phys. Lett.* **81**, 13–15 (2002).

[127] A. Weiling, D. Auston, "Novel sources and detectors for coherent tunable narrow-band terahertz radiation in free space", *J. Opt. Soc. Am. B* **13**, 233-235 (1996).

[128] Y. Liu, S. Park, A. Weiner, "Terahertz Waveform Synthesis via Optical Pulse Shaping", *IEEE J. Sel. Top. Quant. Elec.* **2**, 709-719 (1996).

[129] J. Ahn, A. Efimov, R. Averitt, A. Taylor, "Terahertz waveform synthesis via optical rectification of shaped ultrafast laser pulses", *Opt. Express* **11**, 2486-2496 (2003).

[130] N. Froberg, B. hu, X. Zhang, D. Auston, "Terahertz Radiation from a Photonducting Antenna Array", *IEEE J. Quant. Elec.* **28**, 2291-2301 (1992).

[131] J. Bromage, S. Radic, G. Agrawal, C. Stroud, P. Fauchet, R. Sobolewski, "Spatiotemporal shaping of half-cycle terahertz pulses by diffraction through conductive apertures of finite thickness", *J. Opt. Soc. Am. B* **15**, 1953 1959 (1998).

[132] Y. Lee, T. Meade, T. Norris, A. Galvanauskas, "Tunable narrow-band terahertz generation from periodically poled lithium niobate", *Appl. Phys. Lett.* **78**, 3583-3585 (2001).

[133] D. Kleinman, D. Auston, "Theory of Electrooptic Shock Radiation in Nonlinear Optical Media", *IEEE J. Quant. Elec.* **20**, 964-970 (1984).

[134] D. Cote, J. Sipe, H. vanDriel, "Simple method for calculating the propagation of terahertz radiation in experimental geometries", *J. Opt. Soc. Am. B* **20**, 1374 1385 (2003).

[135] B. Hu, X. Zhang, D. Auston, P. Smith, "Free-space radiation from electro-optic crystals", *Appl. Phys. Lett.* **56**, 506-508 (1990).

[136] T. Qiu, M. Maier, "Long-distance propagatino and damping of low-frequency phononpolaritons in LiNbO3", *Phys. Rev. B* **56**, R5717-5720 (1997).

[137] N. Stoyanov, T. Feurer, D. Ward, K. Nelson, "Direct visualization of phonon-polariton focusing and amplitude enhancement", *J. Chem. Phys.* **117**, 2897–2901 (2002).

[138] C. Chudoba, E. Riedle, M. Pfeiffer, T. Elsasser, "Vibrational coherence in ultrafast excited state proton transfer", *Chem. Phys. Lett.* **263**, 622–628 (1996).

[139] J. Rogers, A. Maznev, M. Banet, K. Nelson, "Optical generation and characterization of acoustic waves in thin films: Fundamentals and applications", *Ann. Rev. Mater. Sci.* **30**, 117–157 (2000).

[140] W. Zhao, J. Wright, "Doubly Vibrationall Enhanced Four Wave Mixing: The Optical Analog to 2D NMR", *Phys. Rev. Lett.* **84**, 1411–1414 (2000).

[141] S. Mukamel, "Multidimensional Femtosecond Correlation Spectroscopies of Electronic and Vibrational Excitations", *Annu. Rev. Phys. Chem.* **51**, 691–729 (2000).

[142] O. Golonzka, M. Khalil, N. Demirdoven, A. Tokmakoff, "Vibrational Anharmonicities Revealed by Coherent Two-Dimensional Infrared Spectroscopy", *Phys. Rev. Lett.* **86**, 2154–2157 (2001).

[143] C. Fecko, J. Eaves, J. Loparo, A. Tokmakoff, P. Geissler, "Ultrafast Hydrogen-Bond Dynamics in the Infrared Spectroscopy of Water", *Science* **301**, 1698–1702 (2003).

[144] M. Cowan, B. Bruner, N. Huse, J. Dwyer, B. Chugh, E. Nibbering, T. Elsasser, R. Miller, "Ultrafast memory loss and energy redistribution in the hydrogen bond network of liquid H2O", *Nature* **434**, 199–202 (2005).

[145] G. Fleming, M. Yang, R. Agarwal, B. Prall, L. Kaufman, F. Neuwahl, "Two Dimensional Electronic Spectroscopy", *Bull. Korean Chem. Soc.* **24**, 1081–1090 (2003).

[146] M. Cowan, J. Ogilvie, R. Miller, "Two-dimensional spectroscopy using diffractive optics based phase-locked phtoon echoes", *Chem. Phys. Lett.* **386**, 184–189 (2004).

[147] P. Tian, D. Keusters, Y. Suzaki, W. Warren, "Femtosecond phase-coherent two-dimensional spectroscopy", *Science* **300**, 1553–1555 (2003).

[148] J. Sakurai, *Modern Quantum Mechanics* (Addison-Wesley, New York, 1994).

[149] B. Grimberg, V. Lozovoy, M. Dantus, "Ultrafast Nonlinear Spectroscopic Techniques in the Gas Phase and Their Density Matrix Representation", *J. Phys. Chem. A* **106**, 697–718 (2002).

[150] T. Brixner, T. Mancal, I. Stiopkin, G. Fleming, "Phase-stabilized two-dimensional electronic spectroscopy", *J. Chem. Phys.* **121**, 4221–4236 (2004).

[151] J. B. V. Cervetto, J. Helbing, P. Hamm, "Double-resonance versus Fourier transform two-dimensional infrared spectroscopy: An experimental and theoretical comparison", *J. Chem. Phys.* **121**, 5935–5942 (2004).

[152] M. Zanni, N. Ge, Y. Kim, R. Hochstrasser, "2D IR spectroscopy can be designed to eliminate the diagonal peaks and exhibit only the cross peaks needed for structure determination", *Proc. Natl. Acad. Sci. U.S.A.* **98**, 11265 (2001).

[153] E. Brown, I. Pastirk, B. Grimberg, V. Lozovoy, M. Dantus, "Population and coherence control by three-pulse four-wave mixing", *J. Chem. Phys.* **111**, 3779–3782 (1999).

[154] V. Lozovoy, B. Grimberg, E. Brown, I. Pastirk, M. Dantus, "Femtosecond spectrally dispersed three-pulse four-wave mixing: the role of sequence and chirp in controlling intramolecular dynamics", *J. Raman Spec.* **31**, 41–49 (2000).

[155] I. Pastirk, E. Brown, B. Grimberg, V. Lozovoy, M. Dantus, "Sequences for controlling laser excitation with femtosecond three-pulse four-wave mixing", *Faraday Discuss.* **113**, 401–424 (1999).

[156] T. Hornung, R. Meier, M. Motzkus, "Optimal control of molecular states in a learning loop with a parameterization in frqeuency and time domain", *Chem. Phys. Lett.* **326**, 445–453 (2000).

Joshua C. Vaughan

MIT Room 6-026
77 Massachusetts Ave.
Cambridge, MA 02139
(617) 253-1956

184 Brookline St.
Cambridge, MA 02139
(617) 576-0976
jvaughan@mit.edu

Education

Massachusetts Institute of Technology   **Ph.D. in Physical Chemistry, Expected 2005**
Graduate research: developed and applied novel optical methods to laser spectroscopy and control of matter in the gas, liquid, and solid phases.

Reed College   **B.A. Chemistry, 2000**
Undergraduate research: Constructed instrumentation for CARS spectroscopy of metal-carbonyl complexes. Minor in music. Commendations for Excellence in Scholarship, 1997-2000 (on leave 1998). Graduated Phi Beta Kappa.

Research Experience

Research Assistant, MIT   **2000-present**
Research Advisor: Keith A. Nelson

- Established methods based on adaptive optics for two-dimensional shaping of femtosecond laser pulses, and applied these to: control of lattice responses traveling at light-like speeds in ferroelectric crystals; phase-stable, optical analogues of multidimensional NMR spectroscopy.

- Measured high-frequency dielectric properties of liquid and crystalline materials in the far-infrared regime. Used ultrafast imaging techniques to monitor propagation of lattice waves in bulk and laser-machined, microstructured ferroelectric materials. Created method for generation of arbitrarily shaped far-infrared waveforms.

- With the biomedical optics group of the Spectroscopy Laboratory at MIT, collaboratively developed a novel technique to perform real-time quantitative phase-contrast microscopy, now used in analyzing cellular processes.

- Set up a new, fully functional laboratory for ultrafast spectroscopy. Coordinated large group purchases and negotiated deep discounts from vendors.

Senior Thesis, Reed College   **1999-2000**
Research Advisor: Daniel P. Gerrity
Designed and constructed instrumentation for coherent anti-Stokes Raman scattering (CARS) spectroscopy, and used it to study the mechanism of the gas phase multiphoton dissociation of $Cr(CO)_6$.

NSF REU Summer Internship, Georgia Institute of Technology   **1999**
Research Advisor: Robert Dickson
Analyzed single dye molecule orientation based on dipole emission patterns. Wrote image analysis in IMAQ and LabVIEW to rapidly determine of the orientation of single dye molecules imbedded in a polymer matrix.

Teaching Experience

Massachusetts Institute of Technology   **2000-2001**
- Teaching assistant for Thermodyamics and Kinetics. Led two, twice-weekly recitations of 15 students each.
- Teaching assistant for Advanced Undergraduate Laboratory. Assisted with the development of a fluorescence resonance energy transfer (FRET) experiment for MIT undergraduate students.

Reed College   **1997-1998**
- Teaching assistant for Organic Chemistry Laboratory.
- Teaching assistant for Natural Science Laboratory.

Publications

- **J.C. Vaughan**, T. Hornung, T. Feurer, K.A. Nelson, "Diffraction-based femtosecond pulse shaping with a 2D SLM," Opt. Lett. **30**, 323-325 (2005).

- G. Popescu, L.P. Deflores, **J.C. Vaughan**, K. Badizadegan, H. Iwai, R.R. Dasari, M.S. Feld, "Fourier quantitative-phase microscopy for investigation of biological structure and dynamics," Opt. Lett. **29**, 2503-2505 (2004).

- T. Hornung, **J.C. Vaughan**, T. Feurer, K.A. Nelson "Degenerate four-wave mixing spectroscopy based on two-dimensional femtosecond pulse shaping," Opt. Lett. **29**, 2052-2054 (2004).

- T. Feurer, **J.C. Vaughan**, T. Hornung, K.A. Nelson, "Typesetting of terahertz waveforms," Opt. Lett. **29**, 1802-1804 (2004).

- **J.C. Vaughan**, T. Feurer, K.A. Nelson, "Automated spatiotemporal diffraction of ultrashort laser pulses," Opt. Lett. **28**, 2408-2410 (2003).

- T. Feurer, **J.C. Vaughan**, K.A. Nelson, "Spatiotemporal coherent control of lattice vibrational waves," Science **299**, 374-377 (2003).

- **J.C. Vaughan**, T. Feurer, K.A. Nelson, "Automated two-dimensional femtosecond pulse shaping," J. Opt. Soc. of Am. B **19**, 2489-2495 (2002).

- T. Feurer, **J.C. Vaughan**, R.M. Koehl, K.A. Nelson, "Multidimensional control of femtosecond pulses using a programmable liquid crystal matrix," Opt. Lett. **27**, 652-654 (2002).

Pending U.S. Patent

"Diffraction-Based Pulse Shaping With a 2D Spatial Light Modulator," **J.C. Vaughan**, T. Hornung, T. Feurer, K.A. Nelson, (application number 60/590,600, filed July 2004).

Selected Presentations

- MIT Physical Chemistry Departmental Seminar, 2005. Lecture: "Application of 2D Femtosecond Pulse Shaping to Coherent Control and Nonlinear Spectroscopy."

- Second International Conference on Coherent Multidimensional Vibrational Spectroscopy, Madison, Wisconsin, 2004. Lecture: "Automated degenerate four-wave mixing spectroscopy via 2D femtosecond pulse shaping."

- Hamamatsu Central Research Labs, Hamamatsu, Japan, 2004. Invited Lecture: "Applications of the Hamamatsu PAL-SLM in Ultrafast Optics." Audience included Hamamatsu president and director of central research labs.

- Modern Optics and Spectroscopy Seminar Series, Spectroscopy Lab, MIT, 2004. Invited Lecture: "Manipulating Light-Matter Interactions via 2D Femtosecond Pulse Shaping."

Additional Skills

Software: Extensive programming experience in MATLAB for data analysis and simulation of complex optical and material responses; created software in LabVIEW to control laboratory instruments and integrate them in sophisticated experiments.

Other: Basic laboratory electronics, machine shop, crystal cutting and polishing, profilometry, STM, and TEM.

References

Prof. Keith A. Nelson
Department of Chemistry
MIT Room 6-235
77 Massachusetts Ave.
Cambridge, MA 02139
(617)253-1423
kanelson@mit.edu

Prof. Thomas Feurer
Institute of Applied Physics
Sidlerstr. 5
Ch-3012 Bern
Switzerland
+41 (0)31-631-8913
thomas.feurer@iap.unibe.ch

Prof. Daniel P. Gerrity
Department of Chemistry
Reed College
3203 SE Woodstock Blvd.
Portland, OR 97202-8199
(503) 771-1112 x7212
gerrity@reed.edu